INSTITUTE OF PHYSICS PUBLISHING REPORTS ON PROGRESS IN PHYSICS

Rep. Prog. Phys. **67** (2004) 2105–2181 PII: S0034-4885(04)71475-X

Recent advances in x-ray absorption spectroscopy

Heiko Wende

Institut für Experimentalphysik, Freie Universität Berlin, Arnimallee 14,
D-14195 Berlin–Dahlem, Germany

Received 8 June 2004
Published 27 October 2004
Online at stacks.iop.org/RoPP/67/2105
doi:10.1088/0034-4885/67/12/R01

Abstract

Using x-ray absorption spectroscopy recent progress is achieved all over in solid state physics. This review focuses on these advances, with particular emphasis on applications to surface physics and to magnetism of ultrathin 3d and 5d films that are made possible by the use of undulators in third generation synchrotron radiation sources: the unambiguous appearance of an atomic extended x-ray absorption fine structure for atomic adsorbates and of σ^* resonances in near-edge x-ray absorption fine structure spectra of oriented molecules is demonstrated. The induced magnetism at the interfaces of 3d and 5d layers is studied by x-ray magnetic circular dichroism. Fundamental aspects of the spectroscopy are clarified for rare earth crystals. The determination of the ground state properties and the detailed understanding of the underlying mechanisms was obtained by comparison of the experimental data to state-of-the-art *ab initio* calculations.

(Some figures in this article are in colour only in the electronic version)

Contents

1. Historical review and introduction

The discovery of x-rays by Röntgen in 1895 (Nobel prize in 1901) opened up new frontiers in the investigation of matter: since these rays have a wavelength similar to atomic distances in solids, x-ray diffraction experiments could probe the inner structure and vibrations of materials at an atomic resolution, which were previously unreachable by optical methods. Laue later received a Nobel prize in 1914 in recognition of his ground-breaking work. In another early development, demonstrating the particle quantum nature of the radiation, it was discovered that ultraviolet light or x-rays upon interaction with matter could generate the emission of electrons with a characteristic energy. This effect, called the photoelectric effect, was first explained by Einstein in 1905 (Nobel prize in 1921). Its development as a successful spectroscopic tool had to wait until further improvements in monochromatic x-ray sources and electron energy analysers. This later development was conducted by Siegbahn *et al* in the 1950s, who later received a Nobel prize in 1981 for his contribution to photoelectron spectroscopy, where ultraviolet light (UPS) or x-rays (XPS) are used. However, the most utilized method of spectroscopy using x-rays before the second world war was invented by Maurice de Broglie, namely, x-ray absorption spectroscopy (XAS). As early as 1913 he published the first observation of an absorption edge [1]. The two different principles are schematically shown; figure 1(*a*) depicts XAS where the x-ray absorption coefficient $\mu(E)$ is measured as a function of the photon energy; in figure 1(*b*) XPS is sketched where the photon energy is fixed at a particular value and the photoelectrons are investigated as function of their kinetic energy depending on various parameters determined by the detector set-up, e.g. the angular dependence and the spin-sensitivity. In this simplified description, the two techniques can be categorized as follows: with XPS the electronic structure of the occupied density of states is investigated whereas the unoccupied density of states determines the fine structure of the near-edge range in the XAS spectra (near-edge x-ray absorption fine structure spectroscopy: NEXAFS; x-ray absorption near-edge spectroscopy: XANES). In the extended energy range of XAS (starting about 50 eV above the absorption edge) the scattering of the photoelectron in the local environment of the absorbing atom dominates the spectra (extended x-ray absorption fine structure spectroscopy: EXAFS). Since this fine structure is due to a short-range order, non-crystalline materials can also be studied with this technique.

Many review articles exist for XPS and x-ray diffraction techniques (see, e.g., [2, 3]). In the present overview we will focus exclusively on some of the recent advances in XAS. Beginning from the 1960s, the speed of the development increases with major advances every ten years. In the 1960s researchers like van Nordstrand [4] modified commercially available diffractometers so that absorption spectra could be obtained using conventional diffraction x-ray tubes. Systematic studies of compounds were carried out and classifications of spectra started. Using rotating anode sources the photon flux of the Bremsstrahlung was relatively low and a successful high sensitive recording of x-ray absorption spectra had clear limitations. However, soon the advantages of the new technique became clear by the use of new x-ray sources: the possibility to choose the energy of the x-rays allows for the tuning to characteristic absorption edges and therefore XAS is element specific.

In 1970 a major breakthrough was made in theory [5, 6]. Lytle described the exciting moment: 'As in the x-ray scattering work, the turning point was the simplification of EXAFS theory to an equation which could be Fourier transformed. Immediately, one is confronted with a series of peaks in a familiar format spaced like a radial distribution function. All the calculational uncertainties of phase shifts, scattering envelopes, temperature factors and mean free paths became less fundamental to an understanding of the phenomenon. Application of the Fourier transform to EXAFS data turned the phenomenon from a persistent scientific

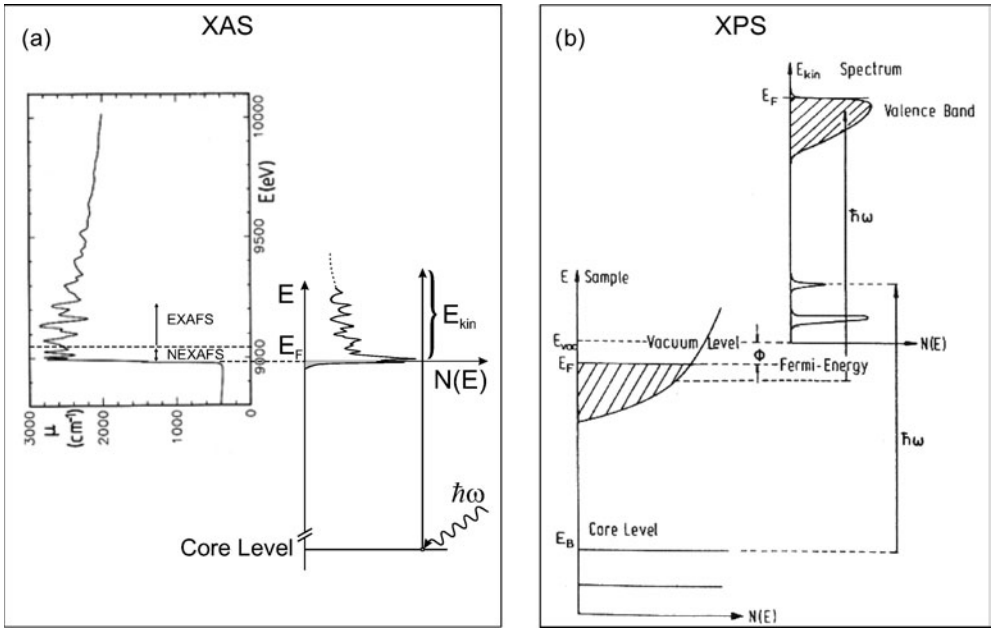

Figure 1. Schematic representation of XAS and x-ray photoemission spectroscopy (XPS). (*a*) In XAS the x-ray absorption coefficient is analysed as a function of the incoming photon energy (spectrum taken from [7]). (*b*) For the investigation of XPS the photon energy $\hbar\omega$ is kept constant and the photoelectrons are measured as a function of their kinetic energy $E_{\mathrm{kin}} = \hbar\omega - |E_{\mathrm{B}}| - \Phi$. $|E_{\mathrm{B}}|$ is the so-called binding energy of the electrons which is related to the Fermi level in solids and to the vacuum level in free atoms or molecules. Φ is the work function. The figure is taken from [2].

curiosity into a quantitative structural tool!' [8]. Employing the new theory, the investigation of the oscillatory fine structure which is caused by the interference phenomena of the outgoing and backscattered photoelectron wave made enormous progress. In this period less attention was drawn to the near-edge fine structure because the energy resolution of the x-ray monochromators was not sufficient to record the small features and the energy shifts at the K, L and M edges. Furthermore, an extensive theory did not exist at this time which allowed for the quantitative description of NEXAFS.

In the 1980s, with the advent of the first dedicated synchrotron radiation sources, the data quality and the acquisition times were greatly improved. Almost like in the visible light regime, the experimentalists made use of the 'white' synchrotron radiation of bending magnets [9] which provides a fantastic tool to investigate x-ray absorption spectra. Now the x-ray absorption technique was used in more advanced experiments: the first simultaneous angular-dependent π^* and σ^* resonances of CO and NO on nickel were measured [10]. A further step was taken with the paper by Stöhr *et al* [11] which included the provocative phrase 'bond lengths with a ruler' in the title. This work incited many discussions and thereby spread the potentiality of NEXAFS spectroscopy among a large scientific community. From this time on, the community split more or less into two branches, namely the groups that investigated NEXAFS and EXAFS. The success of this research in the mid-1980s has been documented in various review articles and books (see, e.g. [12–16]). The status about 20 years ago is visualized in figure 2(*a*). Stöhr and co-workers [17,18] have measured the EXAFS oscillations of half a monolayer of oxygen on Ni(100) in SSRL using the Grasshopper monochromator (flux of $\approx 10^9$ photons s^{-1}) in 1982. These spectra allowed only for the investigation of the

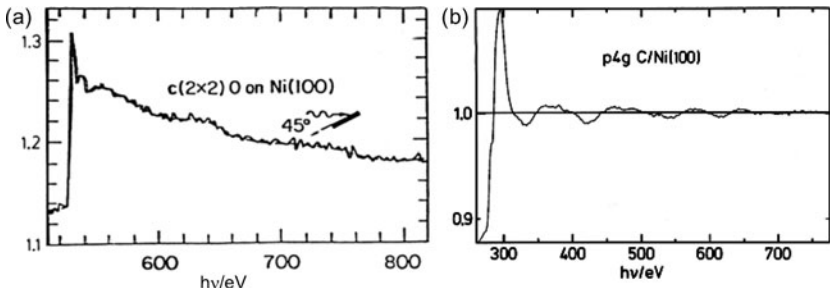

Figure 2. Development of the data quality in second generation synchrotron radiation sources, demonstrated for surface EXAFS data: (*a*) SEXAFS of a submonolayer oxygen on Ni(100): c(2 × 2)O/Ni(100) measured in SSRL in 1982 [17, 18]. (*b*) SEXAFS of a submonolayer carbon on Ni(100): p4g(2 × 2)C/Ni(100) achieved in BESSY I in 1987 [19].

nearest neighbour distance and the local bonding geometry. In the second generation machine BESSY I in 1987, spectra at the carbon K edge of p4g(2 × 2)C/Ni(100) were taken with a photon flux of about 10^{10} photons s^{-1} [19]. One clearly sees the improvement in the signal-to-noise ratio and the more detailed fine structure of the oscillatory part which opened the possibility to also investigate peaks in the Fourier transform at distances larger than the nearest neighbour distances as it is presented, e.g. in [19–23]. Furthermore, more attention was paid to the dynamics, as, for example, to the anisotropy of the surface Debye–Waller factors [24–27].

At this time dramatic developments took place which added the sensitivity to magnetism to XAS. It started in 1985 with the measurement of x-ray resonant magnetic scattering (XRMS) by Namikawa *et al* [28] which was followed one year later by the investigation of the x-ray magnetic linear dichroism (XMLD) by van der Laan *et al* [29]. In 1987 Schütz and co-workers [30] carried out their pioneering works on x-ray magnetic circular dichroism (XMCD) and thereby confirmed the theoretical prediction of this effect by Erskine and Stern in 1975 [31]. This gave an enormous boost to applications and basic research to study magnetic effects, using the inherent advantage of XAS to be element and shell specific. The theoretical understanding was improved by performing *ab initio* calculations of the x-ray absorption cross-sections. Clearly, the better resolved fine structures in the experimental spectra proved to be a challenge to theory. For the description of EXAFS, first a single-scattering theory (see, e.g. [32–35]) and then a high-order multiple-scattering theory in real space (see, e.g. [36–42]) were implemented into the codes which also allowed for the analysis of the angular dependence of the spectra. In the same period calculations of NEXAFS evolved [43–50]. Later on fully relativistic multiple-scattering calculations were able to model the helicity dependence of the EXAFS and NEXAFS of magnetic samples which added spin-sensitivity to the theoretical description (see, e.g. [51–54] and references therein). Also the effects of thermal disorder were included by improved treatments of the EXAFS Debye–Waller factors ([55–59] and references therein). These advances eliminated various arbitrariness in the analysis of the early EXAFS experiments. Nowadays, nearly all parameters (e.g. temperature, angular and spin dependence) are fixed by *ab initio* starting conditions, except the treatment of multi-electron excitations (MEEs) which is phenomenologically described by an amplitude reduction factor S_0^2 (see equation (8) in the next section). Various attempts have been carried out to understand this factor theoretically. It turns out that it is only weakly dependent on energy and can be approximated by a constant in practical calculations (see [60] and references therein).

In the mid-1990s when the third generation synchrotron radiation facilities (like ALS, APS, BESSY II, Elettra, ESRF, SPring-8) came into operation, another enormous step forward was achieved. Insertion devices like wigglers and undulators started to be used routinely. These

allowed for the measurement of x-ray absorption spectra with excellent statistics and high energy resolution. The use of helical undulators enables one to precisely adjust the polarization of the x-rays. With these advantages it is nowadays possible to record XMCD and magnetic EXAFS, which is normally in the range of 10^{-2}–10^{-3} of the isotropic absorption, nearly free of noise with a detailed fine structure. In addition, the isotropic XAS, NEXAFS and EXAFS, also made enormous progress, as will be presented here. Because of the high spectral purity, even small oscillatory fine structures in the x-ray absorption coefficient, as, for example, the atomic EXAFS, can be identified. These previously unrevealed features pushed the theory to new limits.

The present developments point to the following unifications: there is the goal to describe the near-edge (NEXAFS) and the extended energy range (EXAFS) using one theoretical approach, in order to obtain a coherent description of the entire XAS of a sample and thereby deduce its real structure. This field of XAS is a prototype example, where hand-in-hand developments in theory and experiment are performed. The advantage of the theoretical modelling is the possibility to switch on and off specific effects, such as electric dipolar and electric quadrupolar transitions or multiple-scattering versus single-scattering. The experimental results include all these effects and are analysed in their complete content only with the help of theory. This is crucial, since it will be shown in this review that the standard analysis procedures fail for specific cases. Samples are investigated using different techniques, revealing several facets of the systems, e.g. a combined investigation of XAS and x-ray scattering phenomena emerges. There are further applications, such as XMLD [29], x-ray natural dichroism (XNCD) [61] and XRMS [28] which are not covered in this review.

Here, we will present examples of recent progress in surface sciences and the magnetism of thin films using XAS. In the last five years we carried out these studies at undulator beamlines employing the gap-scan technique which provides x-rays with variable polarization in the soft as well as in the hard x-ray regime. These experimental advances allow for the reliable measurement of small fine structures in the x-ray absorption spectra. In addition, the progress in theory enables one to calculate exactly these fine structures, and thereby provides the ground state properties of the material investigated. These possibilities are used here to solve various scientific questions. Scattering phenomena of the photoelectron of atoms and molecules on surfaces are analysed: the so-called atomic EXAFS of atoms on surfaces is studied by polarization-dependent surface EXAFS measurements. This effect originates from the backscattering at interstitial charge densities, and with the help of the angular-dependent analysis the anisotropy of the embedded atom potential could be analysed. This can be used for a more detailed characterization of the bondings involved. Furthermore, the polarization-dependent NEXAFS is investigated experimentally and theoretically for oriented molecules on surfaces which allowed for a clear identification of so-called σ^* shape resonances in the spectra, which has been questioned recently in the literature. It will be shown that the analysis of the helicity-dependence of XAS deepens the insight into the magnetism of nanostructures: because of the high sensitivity of the XMCD technique, the small induced moments in 5d and 3d metals can be studied. A magnetic moment profile will be presented for Ni–Pt multilayers which will be compared to *ab initio* calculations. The detailed analysis of the induced moment in W at the interface to Fe reveals the breakdown of the third Hund's rule in an atomic framework. A short-range polarization of V in Fe–V–Fe trilayers will be studied. The analysis of the induced moments in V is only possible with the help of the theory, since it will be shown here that the single-particle approximation used in the standard XMCD analysis breaks down for the light 3d elements. Furthermore, fundamental aspects of the XAS technique will be clarified by studying the electric dipolar and electric quadrupolar transitions and the spin and energy dependence of the matrix elements at the $L_{2,3}$ edges of rare earth single crystals.

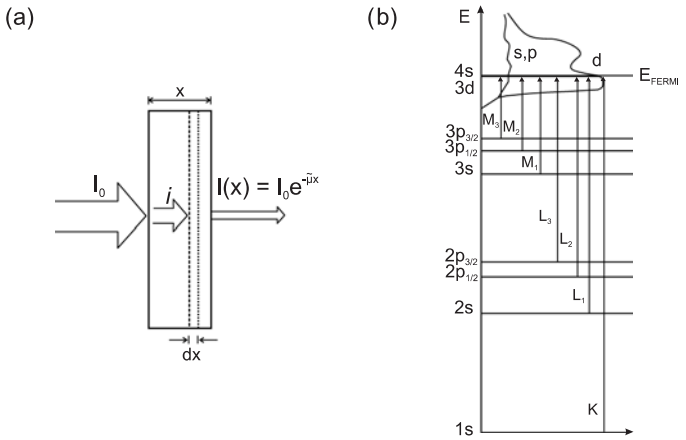

Figure 3. (*a*) Schematic description of the attenuation of x-rays in matter. (*b*) Relation of the x-ray absorption edges and the corresponding excitation of core electrons. The arrows indicate the threshold energy of each edge. The figures are adapted from [89].

The investigation of the temperature dependence of the magnetic EXAFS for these samples provides a deeper insight into effects of local spin dynamics on the dichroic fine structure in the extended energy range. All these examples will demonstrate the very close (in-phase) development of theory and experiment. This review is structured as follows: in section 2 the standard interpretation of XAS will be described and in section 3 the recent advances in experiment and theory are highlighted. Surface sciences mainly got support from investigations with linearly polarized x-rays: examples are given in section 4. New results for the magnetism of nanostructures are achieved using circularly polarized x-rays, as presented in section 5. Finally section 6 summarizes these studies and sheds light on future developments in this field.

2. Standard interpretation of x-ray absorption spectra

Electromagnetic radiation is attenuated in matter which is described by the attenuation coefficient $\tilde{\mu}(E)$. This property enters into Beer's Law:

$$I(x) = I_0 \, \mathrm{e}^{-\tilde{\mu}x}, \tag{1}$$

where I_0 is the intensity of the incoming x-rays and i is the intensity inside a slab of the absorbing material (total thickness x) (see figure 3(*a*)). There is a loss of intensity $\mathrm{d}I$ in each infinitesimal slab $\mathrm{d}x$. After traversing through the material, the x-ray intensity is reduced to $I(x)$. In the range of x-ray wavelengths investigated here the elastic Rayleigh and the inelastic Compton scattering can be neglected. Therefore, the attenuation coefficient $\tilde{\mu}$ is approximately identical to the photoelectric absorption coefficient μ, which is the key property in XAS. The characteristic features of the x-ray absorption coefficient are the absorption edges: if the photon energy is large enough to excite an atomic core electron into the continuum, a step-like increase is found in the x-ray absorption coefficient. These edges are labelled as given in figure 3(*b*) according to the Sommerfeld notation. Since the energies of the edges (or ionization energies) are unique for a specific element, XAS is element specific. In the vicinity of a specific absorption edge the photoelectric absorption coefficient is dominated by the absorption processes which start from this particular core level. The absorption coefficient

μ can be described by Fermi's golden rule in the one-electron approximation:

$$\mu(\hbar\omega) \propto \sum_f |\langle\psi_f|\boldsymbol{p}\cdot\boldsymbol{A}(\boldsymbol{r})|\psi_i\rangle|^2\delta(E_f - E_i - \hbar\omega), \tag{2}$$

where $|\psi_f\rangle$ and $|\psi_i\rangle$ are the final and initial states with energies E_f and E_i, respectively. The quantity $\boldsymbol{p}$ is the momentum operator and $\boldsymbol{A}(\boldsymbol{r})$ is the vector potential of the incident electromagnetic field. The vector potential can be taken as a classical wave $\boldsymbol{A}(\boldsymbol{r}) \cong \hat{\epsilon}A_0\,\mathrm{e}^{\mathrm{i}\boldsymbol{k}\cdot\boldsymbol{r}}$ with the polarization $\hat{\epsilon} \perp \hat{\boldsymbol{k}}$. In most of the cases the spatial dependence of the electromagnetic field can be neglected and therefore the core excitations can be described by electric dipole transitions (E1) by approximating $\mathrm{e}^{\mathrm{i}\boldsymbol{k}\cdot\boldsymbol{r}} \cong 1$. However, electric quadrupolar transitions (E2) must be considered, e.g. for the description of the $L_{2,3}$ edge rare earth XMCD spectra (see section 5.3) as well as for the analysis of transition metal K edges [62–65].

2.1. NEXAFS and XMCD

First, we start with the analysis of the near-edge structure of the x-ray absorption coefficient. NEXAFS depends on the local geometric structure and the spectral shape reflects the excited state electronic structure. This is due the creation of a screened core hole in the XAS process. Therefore, calculations to model the experimental data are performed in two limits, i.e. using static-initial or final-state potentials (see, e.g. [66, 67]). For various cases, as for example the heavy 3d elements Fe, Co and Ni, the experimental spectra can be described by initial-state calculations which neglect the core hole correlation effects. For these cases, the x-ray absorption coefficient $\mu(E)$ can be related to the angular momentum projected density of unoccupied states (LDOS), $\rho(E)$, by using the expressions for the transition matrix elements (see, e.g. [43, 48, 53, 68]):

$$\rho(E) = \gamma(E)\mu(E). \tag{3}$$

Here, $\gamma(E)$ is a smoothly varying function which can be determined from the atomic ground-state function $\rho_0(E)$ and the atomic x-ray absorption coefficient $\mu_0(E)$ by the ratio $\gamma(E) = \rho_0(E)/\mu_0(E)$ which can be determined theoretically [68]. In this review mostly the near-edge range of the dichroic spectra (XMCD) is analysed to study the magnetism of the samples. Therefore, the spin-dependent density of states must be investigated, as, e.g. the 3d states of the ferromagnets Fe, Co and Ni. Hence, the final 3d states are probed by electric dipole transitions at the $L_{2,3}$ edges for these metals. To describe the basic idea of the XMCD technique a two-step model can be applied: in the first step, a spin-polarization of the photoelectron is created by the Fano effect [69, 70], by using circularly polarized x-rays as schematically described in figure 4(*a*). At the L_3 edge more spin-down (spin-up) electrons are excited with right (left) circularly polarized x-rays ($\boldsymbol{M} \parallel \boldsymbol{k}$). In the second step, these polarized photoelectrons can be used to analyse the spin-split final density of states, thus the valence band acts as a spin-sensitive detector. Hence, for the case presented in figure 4(*a*), mainly the majority (minority) band is probed with right (left) circularly polarized x-rays. The difference in the x-ray absorption coefficients thereby reflects the imbalance of the spin-dependent empty density of states, i.e. the imbalance of the majority and minority bands. However, for a more accurate description of the XMCD line shape the initial and final state sublevels have to be taken into account, as shown for left circularly polarized x-rays in figure 4(*b*). This can be described in a single-step excitation from well defined initial and final states according to equation (2). In this formalism the angular part of the matrix elements depends on the spin of the sample and the helicity of the incoming x-rays. At the L_2 edge (initial state $2p_{1/2}$) the transitions are confined to final $3d_{3/2}$ states by the dipole selection rules

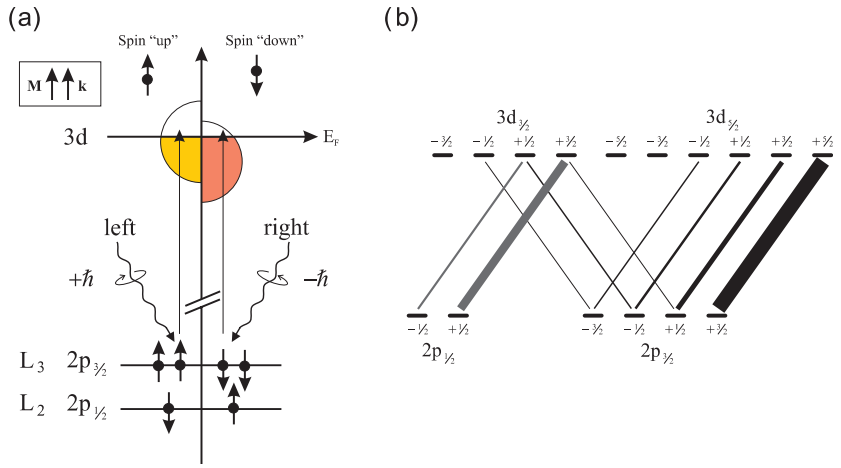

Figure 4. (*a*) Schematic description of the helicity dependent transitions at the $L_{2,3}$ edges of a 3d transition metal. By excitation with circularly polarized x-rays of the initial 2p states a spin-polarization of the photoelectron is created. The spin-split d density of states acts as a spin-sensitive detector (figure adapted from [71–73]). (*b*) Oscillator strength according to the angular matrix elements represented by the line thickness for left circularly polarized x-rays. For clarity the transitions to the 4s levels are neglected (figures adapted from [53, 73, 74]).

(transitions to 4s states are neglected for clarity). Therefore, the spectral shape of the XMCD signal at the L_3 edge and the L_2 edge must not be identical.

The arguments given above reveal that under certain assumptions the XAS spectra map the LDOS. Hence, the energy integrated isotropic spectrum measures the number of unoccupied states for the final states with l character if the energy dependence of the radial matrix elements is neglected. Consequently, the spin moment μ_S and orbital moment μ_L can be determined within the framework of the two-step model described above by applying the so-called sum rule procedure (see, e.g. [75–83]). For the $L_{2,3}$ edges these sum rules were derived by Thole *et al* [77] and Carra *et al* [78] and can be written in the following form:

$$\frac{\mu_L}{\mu_B} = -\frac{2N_h}{N}\int (\Delta\mu_{L_3} + \Delta\mu_{L_2})\,\mathrm{d}E, \tag{4}$$

$$\frac{\mu_S}{\mu_B} = -\frac{3N_h}{N}\int (\Delta\mu_{L_3} - 2\Delta\mu_{L_2})\,\mathrm{d}E + 7\langle T_z\rangle, \tag{5}$$

where $\Delta\mu_{L_3} = \mu^+_{L_3} - \mu^-_{L_3}$ is the XMCD difference of the x-ray absorption coefficients for right and left circularly polarized x-rays at the L_3 edge. Furthermore, the integrated spectrum for the unpolarized radiation $N = \int_{L_3+L_2}(\mu^+ + \mu^- + \mu^0)\,\mathrm{d}E$ and the number of unoccupied d states N_h enter into the equations given above. The asphericity of the spin magnetization is considered by the expectation value of the magnetic dipole operator $\langle T_z\rangle$. By angular-dependent measurements the influence of this term on XMCD can be identified [84]. Originally the sum rules are derived in an atomic framework. However, Ankudinov and Rehr demonstrated that the application of the sum rules is not only restricted to these atomic systems [81]. Various assumptions are made in the derivation of the sum rules (see, e.g. [53, 74]). Despite these assumptions the sum rules work astonishingly well as it is demonstrated, e.g. for the classical ferromagnets Fe, Co and Ni [68, 74, 80]. This is tested by using band-structure calculations and the corresponding calculated XMCD spectra.

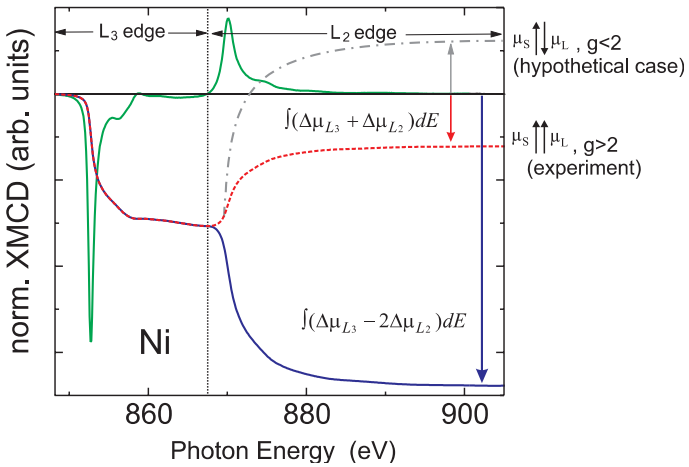

Figure 5. XMCD difference for Ni and the XMCD integrals which are necessary for the application of the integral sum rules.

To illustrate the application of the integral sum rules, a Ni XMCD spectrum at the $L_{2,3}$ edges is presented in figure 5. According to equation (4) the entire XMCD signal has to be integrated (marked area). This integral is given by the dashed line and the constant value indicated by the arrow is used to calculate μ_L. For the determination of the spin moment μ_S the L_2 edge contribution has to be subtracted from the L_3 edge one. Consequently these two contributions have to be separated. The resulting integral is given by the solid line, and from the value marked with the larger arrow the spin moment is calculated. Without going into details of the quantitative analysis, the relative orientation of μ_S to μ_L can be directly determined from these integrals. For the case of Ni (figure 5) a parallel alignment is found, since both values of the integrals exhibit the same sign. The g-factor is connected with these moments by $\mu_L/\mu_S = (g-2)/2$ [85,86]. Hence, the parallel alignment of μ_L and μ_S results in $g > 2$, as shown in figure 5. This is in agreement with the expectation, according to the third Hund's rule, in an atomic framework, since an antiparallel alignment of the orbital and the spin moment is anticipated for less than half-filled shells. For the 3d transition metals this would be the case for the lighter elements, as for example, vanadium. In this case the integral of the entire XMCD signal would cross the zero line as depicted schematically by the hypothetical dot-dashed line which corresponds to $g < 2$. The qualitative analysis of the relative orientation of μ_L and μ_S can be summarized by the following simple rule: if the integral of the entire XMCD signal $\int(\Delta\mu_{L_3}+\Delta\mu_{L_2})\,\mathrm{d}E$ exhibits a node, μ_L and μ_S are aligned antiparallel ($g < 2$); if this integral does not cross the zero line, μ_L and μ_S are oriented parallel ($g > 2$).

2.2. EXAFS

The characteristic feature of the extended energy range of the x-ray absorption coefficient (about 50 eV above the absorption edge) is the oscillatory fine structure. This fine structure is termed EXAFS by Prins and Lytle [87]. As pointed out by Kronig [88] in 1932 this oscillatory structure is related to the influence of neighbouring atoms on the transition matrix element in the golden rule, i.e. a short-range effect. Therefore, a precise information of the local atomic structure around the absorbing atom can be achieved by the investigation of the scattering of the photoelectron. The oscillatory fine structure $\chi(E)$ is extracted from the x-ray absorption

coefficient $\mu(E)$ by subtracting the atomic background $\mu_0(E)$ and normalizing to the edge jump of the smooth atomic-like background $\Delta\mu_0$:

$$\chi(E) = \frac{\mu(E) - \mu_0(E)}{\Delta\mu_0}. \tag{6}$$

The oscillatory fine structure is discussed as function of the photoelectron wavenumber

$$k = \sqrt{\frac{2m}{\hbar^2}(E - E_0)}. \tag{7}$$

Here, E_0 is the threshold energy and m is the electron mass. Within a multiple-scattering theory this oscillatory fine structure can be described by [89]

$$\chi(k) = S_0^2 \sum_{\text{paths}} \frac{|f_{\text{eff}}|}{kR^2} \sin(2kR + \Phi_k)\, \mathrm{e}^{-2R/\lambda_k}\, \mathrm{e}^{-2\sigma^2 k^2}. \tag{8}$$

This equation has the same form as the splendid formula reported by Sayers *et al* in 1971 [6]. Nevertheless, the quantities in this equation have to be redefined for a multiple-scattering framework which includes curved-wave and many-body effects. The important structural property is the effective path lengths $R = R_{\text{path}}/2$ of each scattering path. Furthermore, an effective curved-wave scattering amplitude $f_{\text{eff}}(k)$ is introduced, and S_0^2 describes an amplitude reduction factor due to many-body effects (intrinsic losses as, e.g. shake-up and shake-off excitations). The EXAFS mean free path depicts extrinsic losses (plasmons, electron–hole pairs, inelastic scattering) in a phenomenological way by its energy dependence $\lambda = \lambda(k)$. For a proper structural analysis the phase factor $\Phi_k = \arg f_{\text{eff}}(k)$ has to be known which reflects the quantum mechanical wavelike nature of the backscattering. A major contribution to this phase is the central atom phase shift since the photoelectron experiences the potential of this atom twice. The total phase is responsible for a difference between the R position in Fourier transform of EXAFS and the geometrical interatomic distance. Since this difference is in the range of some tenths of an angstrom it has to be corrected in the analysis by a theoretical or experimental standard. The temperature dependence is considered by the mean square relative displacement (MSRD) σ^2. This quantity can be disentangled into a temperature-independent contribution σ^2_{stat} which describes the static disorder and a temperature-dependent one σ^2_{dyn} which accounts for the dynamic disorder by lattice vibrations. σ^2 enters into the EXAFS Debye–Waller factor $\mathrm{e}^{-2\sigma^2 k^2}$ which leads to the stronger damping of the EXAFS oscillations at larger k-values. For a more comprehensive description of the configurational and thermal average, a radial pair-distribution function is introduced which is disentangled in its moments (cumulant expansion [56]). The first cumulant is the average distance of the absorber to the backscatterer; the second cumulant is the MSRD σ^2. The third cumulant is the first correction term that accounts for the anharmonicity of the effective pair potential. This term leads to an apparent contraction of the interatomic distances as determined by EXAFS. This is because the odd moments enter into the EXAFS phase Φ_k which determines the period of the oscillations. The even ones contribute to the EXAFS Debye–Waller factor and thereby influence the amplitude of the wiggles. As discussed in the following section the above-mentioned EXAFS theory is implemented into various codes that can be used to create theoretical standards. Using these standards the structural analysis of the experimental data can be carried out with well established fitting routines. In this work the FEFF [89–91] and FEFFIT [92] codes were applied for the EXAFS analysis.

An interesting question is whether these standard interpretations of XAS are adequate to analyse samples of today's technical as well as fundamental interest. The state-of-the-art EXAFS analysis is quite advanced and provides very reliable structural parameters including

static and dynamic disorder. However, the scattering of the photoelectron at interstitial charges is not considered in this standard analysis, although it can provide detailed insight into the nature of the bonding. Concerning the near-edge range the sum rule analysis of the XMCD spectra is established as for example for the heavier 3d elements Fe, Co and Ni where the $L_{2,3}$ edges are well separated. But the single particle model which is used in the derivation of the integral sum rules breaks down, e.g. for the light 3d metals. Furthermore, the fine structures resolved in the rare earth L edge XMCD cannot be described in the dipole approximation since electric quadrupolar transitions appear. In addition, it turns out that the transition matrix elements are strongly spin and energy-dependent, which actually results in the determination of the wrong sign of the 5d moments for rare earth metals with the standard analysis. The influence of these effects can be directly identified in the fine structures of XAS, however, they are disregarded when only the integrated intensity of a spectrum is analysed (sum rules). All these difficulties demonstrate the need for improvements in the experiment, in order to clearly resolve the fine structures, as well as in the theory, in order to model those.

3. Advances in experiment and theory

In the following the recent progress in the experiments and in theory is summarized. It will be shown that the use of insertion devices in the new third generation synchrotron radiation facilities offer the possibility to measure the x-ray absorption spectra with much better statistics and higher energy resolution. Thereby, small fine structures can be resolved in XAS which provide a detailed understanding of the ground state properties. This is only possible by comparison of the experimental data to *ab initio* calculations which yield the ground state properties and the corresponding spectra. Various advancements in the theoretical models were necessary (full multiple-scattering (FMS), self-consistent field and fully relativistic calculations) e.g. for a quantitative analysis of the near-edge regime. Different approaches also address the interaction of the core hole with the photoelectron and thereby pave the way to the theoretical description of an excited state spectroscopy.

3.1. Experiment

The main characteristic of the new third generation synchrotron radiation sources is the use of insertion devices in the linear sections of the storage rings. In contrast to the main utilization of *bending magnets* for the production of the continuous synchrotron radiation (second generation machines), nowadays the usage of periodic magnetic arrays consisting of permanent magnets dramatically increases the brightness (photons per [s mrad^2 0.1% $\Delta E/E$]) of the x-rays by orders of magnitude. Such a magnetic array is schematically shown in figure 6. These magnetic arrays can be applied in two modes for the production of x-rays which depend on the size of the K parameter. This parameter is defined by the period length of the magnetic array λ_0 and the peak magnetic field B_0 via: $K = 0.934\lambda_0 B_0/(\mathrm{cm\,T})$. The maximum deflection angle δ of the electron beam to the forward direction can be calculated from K and $\gamma = E/mc^2$ by: $\delta = K/\gamma$. A *wiggler* is realized through large magnetic fields and long period lengths ($K \gg 1$). In this case, the emitted radiation interferes incoherently and therefore the spectrum is similar to that of a bending magnet. However, the central brightness of the wiggler within the opening angle 2δ is increased by about two times the number of the wiggler periods N. An *undulator* employs smaller magnetic fields ($K \leqslant 1$). This results in a coherent superposition of the emitted radiation. Due to this interference effect the undulator spectrum consists of sharp peaks at characteristic wavelengths (fundamental and higher harmonics), and the central brightness of the undulator radiation is up to N^2 times larger when compared with that of a bending

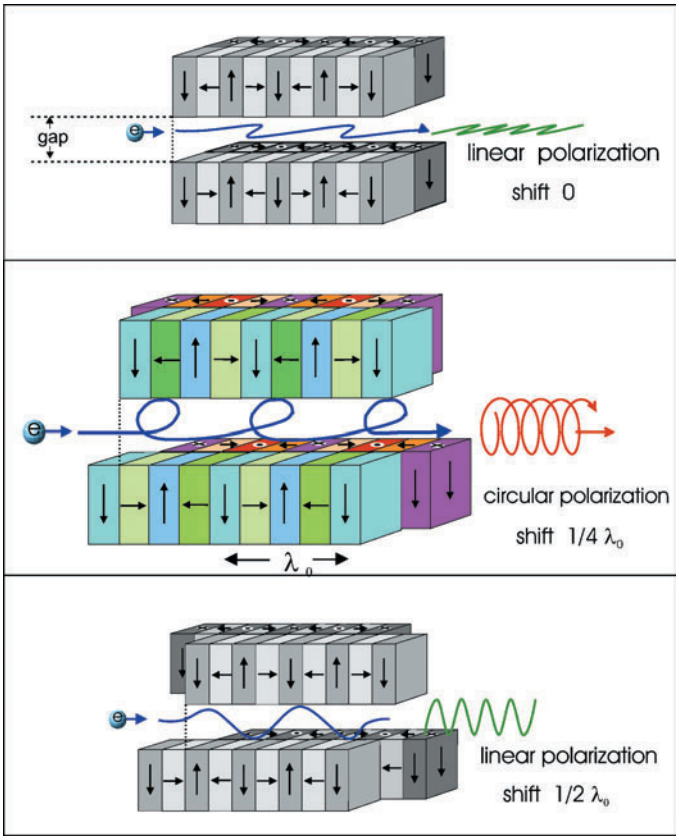

Figure 6. Schematic representation of a helical undulator of the APPLE II type used at BESSY II [93].

magnet. However, it should be noted that in contrast to the continuous bending magnet and wiggler spectrum, undulators are line sources. Therefore, the K parameter must be changed continuously at the same time with the monochromator in order to measure x-ray absorption spectra. This is done by changing the magnetic field by varying mechanically the gap between the arrays of magnets above and below the electron orbit (see figure 6). To illustrate the use of the gap-scan technique, an experimental x-ray absorption spectrum of half a monolayer of atomic oxygen chemisorbed on a Cu(110) substrate at the oxygen K edge is depicted together with the spectral flux of the third harmonic for specific fixed gap-settings in figure 7. The sharpness of these peaks demonstrates the need to vary the gap parallel to the monochromator, which is possible nowadays in a few third generation synchrotron radiation facilities like BESSY II and ESRF. The surface EXAFS (SEXAFS) data shown in figure 7 were achieved by changing the gap at the same time with the monochromator at every photon energy point of the spectrum (1 eV steps). The spectrum is an average of three spectra taken in one hour at BESSY II. This time has to be compared with the averaging time of two to three days which was necessary to achieve spectra as shown in figure 2(b) at BESSY I. The parallel motion of the gap and the monochromator might appear as a drawback since the trajectory of the electron bunches in the storage ring is permanently changed during a scan. However, this technical difficulty is solved and the gain in photon flux allows, e.g. for the measurement of prominent SEXAFS oscillations, nearly free of noise for coverages as low as 0.5 ML atomic oxygen. Thereby, it

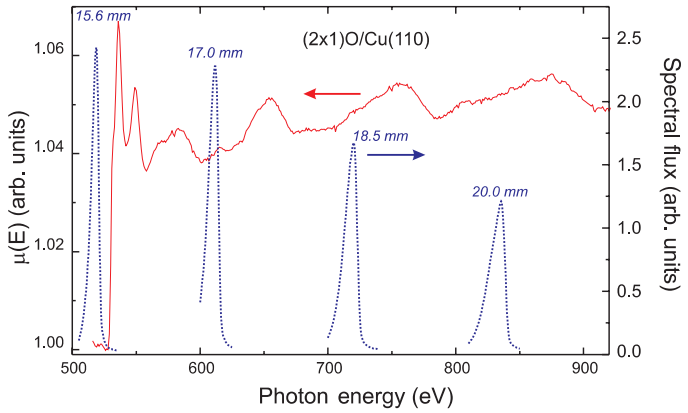

Figure 7. Gap-scan technique (U41/1-PGM beamline at BESSY II): x-ray absorption coefficient of 0.5 ML atomic oxygen chemisorbed on Cu(110) in the extended energy range of the O K edge at 50 K. For the measurement, the undulator gap was changed at the same time with the monochromator setting at every photon energy point (1 eV steps). The spectral flux of the third harmonic is given for specific gap settings in order to depict the linewidth of the undulator spectrum.

is possible for the first time to unambiguously detect small features in the fine structure of the x-ray absorption coefficient, an example of atomic EXAFS is presented in section 4.1. In addition to the larger photon flux provided by the undulator the energy resolution is much higher compared with the bending magnet radiation of the second generation sources. One reason for this improvement is the smaller source size of the third generation machines which is achieved by the higher stability of the electron bunches in the storage ring. Furthermore, the divergence of the insertion device x-ray radiation is lower compared to bending magnets. Therefore, the illuminated area of the optical components is reduced and the influence of the slope and shape errors is minimized. The physical quantity that describes these improvements is the brilliance which is defined as the photon flux per unit phase space volume (photons per [s mrad^2 mm^2 0.1% $\Delta E/E$]). The brilliance is enlarged by up to four orders of magnitudes compared with the older machines. This leads to a dramatic increase of the energy resolution which is of great importance when the near-edge fine structures are studied in detail as it will be discussed below.

A further advantage of insertion devices is the possibility to produce x-rays with variable linear, elliptical and circular polarization. This allows for the analysis of the magnetic properties of the samples, e.g. with the XMCD technique. The APPLE II type undulator [93,94], presented in figure 6, is an example of such an insertion device. It consists of two rows of planar permanent magnets above and below the electron orbit plane. By shifting the opposing magnet rows relative to each other the magnetic fields can be modified, producing various types of electron orbits such as vertical sinusoidal (figure 6, bottom), horizontal sinusoidal (top) or helical motion (centre). We applied the gap-scan technique also for these undulator types, which ensures a constancy of the degree of circular polarization in combination with a high photon flux. This technique allowed us to measure the detailed fine structure in the soft x-ray XMCD stemming from the induced magnetism in light 3d metals, as discussed in section 5.2. While various investigations of magnetic materials have been carried out in the soft x-ray range [95], the resolution of fine structures in the XMCD of rare earth metals in the hard x-ray range is also of technical as well as of fundamental importance. Thereby, the basic understanding of XMCD spectroscopy can be advanced. This is shown in figure 8 where the pioneering XMCD spectra at the $L_{2,3}$ edges of a Tb foil taken by Schütz *et al* in 1988

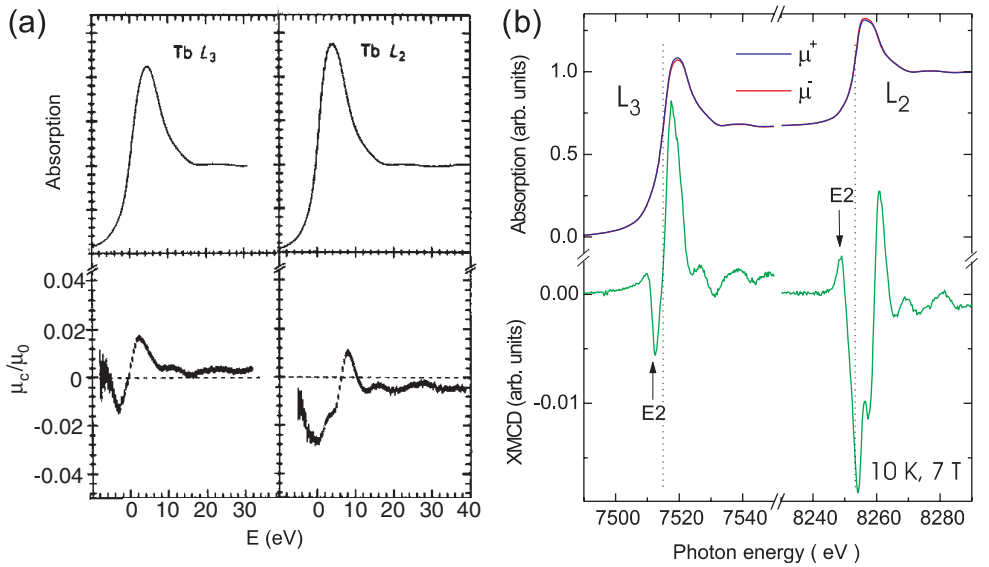

Figure 8. Comparison of (*a*) the pioneering XMCD results at the $L_{2,3}$ edges of a Tb foil taken by Schütz *et al* at HASYLAB in 1988 [96] to (*b*) the spectra for a Tb single crystal measured recently at the ID 12 beamline at the ESRF [97].

at HASYLAB [96] are compared with the spectra of a Tb single crystal measured recently at the ESRF [97]. It is to be noted that in the pioneering experiments the dichroic signal is divided by the isotropic XAS. Therefore, the maximum of the dichroic signal in the earlier work (figure 8(*a*)) appears to be reduced compared with recent measurements (figure 8(*b*)), where directly the difference $\mu^+(E) - \mu^-(E)$ of the x-ray absorption coefficients for right (μ^+) and left (μ^-) circularly polarized x-rays is presented. Because of the excellent performance of the third generation synchrotron radiation facilities, nowadays the fine structures in XMCD can be resolved much more clearly. For example, the structure in the pre-edge regime of the L_2 edge marked with E2 could not be detected in the earlier works (figure 8). However, it will be shown in section 5.3 that this feature can be assigned to electric quadrupolar transitions (E2) whereas the main XMCD signal originates from electric dipole transitions (E1). This disentanglement was not possible in the earlier work.

A further experimental advantage which is applied here is the *in situ* preparation of ultrathin magnetic films. This means that prototype samples, as, e.g. trilayer systems are prepared and measured step by step in the UHV chamber directly at the synchrotron radiation source. As will be demonstrated in section 5.2, this allows for a controllable growth of the ultrathin films *in statu nascendi* yielding samples with sharp interfaces. Thereby, structures can be prepared which are close to the idealized picture, as given, e.g. in figure 19. Approaching experimentally the ideal structures, which are used as inputs to theory, allows for the direct comparison of the modelling with experimental results.

3.2. Theory

In the last ten years there has also been striking progress in *ab initio* calculations of x-ray absorption spectra. These advances revolutionized the analysis of EXAFS. Nowadays, the EXAFS theory in a multiple-scattering framework is well established [89, 90, 98]. Today

theoretical standards eliminate the arbitrariness in the experimental analysis as it was done in the early days by means of tabulated standards [99,100]. The EXAFS theory is implemented in various *ab initio* codes like CONTINUUM [44], EXCURV [101], FEFF [91], GNXAS [102], WIEN2k [103], the Munich SPRKKR package [104,105] and others [45]. Even the description of the magnetic counterpart of this technique, i.e. MEXAFS, is now mature [51,104]. However, it turns out that a fully quantitative treatment of the near-edge structures is still challenging. This is due to various many-body effects, as for example the photoelectron-core hole interaction, multiplet effects, the photoelectron self-energy and inelastic losses. Various theoretical treatments, e.g. of metals, are based on the final state rule in an one-electron approach: the final states are calculated in the presence of an approximately screened core hole, and the many-body effects and inelastic losses are described by a complex optical potential. A different approach for the calculation of the near-edge structures is the atomic multiplet theory [106,107]. Unfortunately, both approaches have their specific drawbacks: on the one hand the one-electron approach ignores atomic multiplet effects. On the other hand the atomic multiplet theory makes use of a crystal-field parametrization of solid state effects and ignores delocalized states [90]. Recently, there has been progress to go beyond the one-electron approach in order to calculate x-ray absorption spectra [108–113]. In some of these works a GW approach is used [110,111]. The name of this approach originates from the electron self-energy which involves the product of the electron Green's function G and the dynamically screened interaction W (see, e.g. [114]). Another approach is based on a time-dependent density-functional theory (TDDFT), as it has been successfully applied to optical excitations in atoms [115]. The application of this approach to x-ray absorption spectra at the $L_{2,3}$ edges for the 3d transition metal series has been demonstrated recently [109, 112, 113].

All the experimental results of this review are compared to present state-of-the-art calculations. The advantage of the theoretical calculations available at present is the fact that they provide the (magnetic) ground state properties of the systems investigated *and* the corresponding x-ray absorption spectra. This is of great relevance, since it will be shown here that for systems of technical as well as fundamental interest, the standard analysis of the x-ray absorption spectra breaks down. Hence, the only possibility of analysing these spectra is by comparison to the *ab initio* theory. This comparison reveals that the experimental advances are crucial since they allow for the detection of a detailed fine structure in XAS which can be modelled nowadays with the calculations mentioned above. The calculations presented here have been carried out in collaboration with Rehr and Ankudinov (University of Washington) and were provided by Ebert and Minár (Ludwig-Maximilians-Universität München) by applying the FEFF code [91] and by using the fully relativistic spin-polarized Korringa–Kohn–Rostoker (SPR-KKR) Green's function method [53, 104], respectively. The FEFF code is based on a real space Green's function formalism. Relativistic effects are treated with a relativistic Dirac–Fock atom code. In this multiple-scattering formalism the photoelectron Green's function corresponds to a propagator in real space. This approach does not necessitate highly symmetric systems. To describe the oscillatory fine structure in the extended energy range (EXAFS) a path expansion is used. Thereby, it is possible to disentangle the multiple-scattering from the single-scattering contributions by calculating the contributions of specific scattering paths. An automatic 'path filter' is used, which determines the most important paths by analysing whether the contribution of a certain path is above or below a defined cutoff. To calculate EXAFS it is usually sufficient to use about 10^2 paths to model the data within the experimental accuracy. In order to consider curved-wave effects an effective scattering amplitude f_{eff} is used—the property which gave the FEFF code its name. The scattering potentials are constructed using the overlapped muffin tin approximation. To account for inelastic losses a complex and energy-dependent self-energy

is calculated. Thermal disorder is included by the EXAFS Debye–Waller factor which can be described for solids by the correlated Debye model [55]. The cumulant expansion is applied which is a parametrization of the vibrational distribution function expanded in its moments. With these advances the FEFF calculations reproduce the experimental EXAFS generally within the experimental errors (few per cent). To calculate NEXAFS a FMS calculation is carried out for a defined cluster size by matrix inversion. Chemical effects like charge transfer can become important for the description of the near-edge structures. Therefore, a self-consistent field approach is implemented into the code that provides an accurate estimate of the Fermi energy. These FMS calculations yield results that are equivalent to band structure methods like the KKR procedure. However, the FEFF code is not self-consistent with respect to the spin-dependence. Hence, SPR-KKR band-structure calculations utilizing a multiple-scattering formalism were carried out to quantitatively analyse the induced moments in 3d and 5d metals at the interface to ferromagnets. These calculations reproduce, e.g. the size of the induced moment in V in a $Fe_{0.9}V_{0.1}$ alloy within an error bar of about 10% as compared to polarized neutron studies. For the determination of the magnetic moment of Fe in this alloy the error reduces to a few per cent (see table 2). Detailed reviews on the SPR-KKR Green's function approach are presented by Ebert [53, 104]. Also in this formalism, a translational symmetry is not necessary and an atomic sphere approximation is applied as a geometrical constraint for the potential functions, charge density and spin magnetization.

4. Surface physics of atomic and molecular adsorbates

In this section, scattering phenomena of the photoelectron will be analysed for surface systems. Two examples are presented here: atomic oxygen chemisorbed on Cu(110) and oriented hydrocarbon molecules adsorbed on Cu(100). These systems were chosen to identify specific scattering processes that are still debated in literature. The highly anisotropic reconstructed O/Cu(110) system was selected to study the scattering of the photoelectron at interstitial charge densities which is responsible for the so-called atomic EXAFS (AXAFS). Oriented hydrocarbon molecules are measured to analyse the shape resonances which originate from photoelectron scattering at the intramolecular potential. Both investigations were performed at the K edges of the low Z elements C and O, respectively. At this absorption edge the 1s electron is excited to a final d state. Hence, the photoelectron is emitted basically into the direction of the electric field vector $\vec{E}$. This can be used as a 'searchlight' if angular-dependent measurements are carried out, i.e. with variable orientation of the sample with respect to the incident x-rays. This allows for the identification of scattering phenomena as the origin of the atomic EXAFS and of the shape resonances. To support these findings the experimental results are compared to *ab initio* calculations in the framework of a multiple-scattering formalism.

4.1. Atomic EXAFS

Here, we want to provide further insight into the so-called atomic EXAFS (AXAFS) effect by investigating the angular dependence of the x-ray absorption coefficient for a strongly anisotropic surface system. The AXAFS originates from the backscattering of the photoelectron at interstitial charge densities located between the atoms. At first, the regular surface EXAFS of the reconstructed (2×1)O/Cu(110) surface is studied in order to demonstrate the strong structural anisotropy (C_2 symmetry) of this system. This is followed by a thorough analysis of the atomic EXAFS by studying the structures in the Fourier transform of the SEXAFS at distances smaller than the nearest neighbour one. The clear angular dependence of the AXAFS reflects the non-spheric scattering potential due to the high directionality of

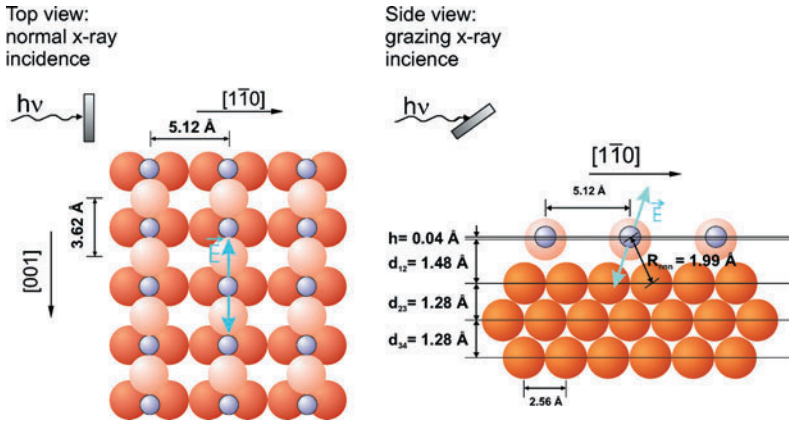

Figure 9. Schematic representation of the adsorption geometry for the (2 × 1)O/Cu(110) system in top view and side view as determined from [131]. Small shaded circles: oxygen atoms, large light circles: Cu atoms of the first layer, large dark circles: Cu atoms of the second and following layers. The E-vector for different x-ray incidences is given schematically.

the O–Cu bonds. For a detailed investigation of the AXAFS the experimental spectra are compared to *ab initio* calculations.

While the regular EXAFS stems from the backscattering of the photoelectron at neighbouring atoms, the AXAFS contribution is assigned to the scattering at the charge densities placed between the atoms. The presence of the controversial AXAFS effect (see, e.g. [116–126]) was definitively observed for the low Z elements nitrogen and oxygen for the (2 × 3)N/Cu(110) and ($\sqrt{2}$ × 2$\sqrt{2}$)R45° O/Cu(100) systems [127–130]. However, the lack of attention to the AXAFS effect over the years was partly due to the non-availability of high quality data. These data are nowadays achieved by scanning the gap of the undulator, parallel to the monochromator—the so-called gap-scan technique. Another reason for ignoring the backscattering of the photoelectron at the interstitial charge densities (embedded atom) may be the fact that many fitting procedures minimize the Fourier transform intensities for distances below the nearest neighbour one. Light adsorbates on metal surfaces are established as model systems for this kind of investigation since no MEEs can mimic the long-range oscillatory fine structure in the x-ray absorption coefficient [128, 129] as it can be the case for heavier atoms [118, 119, 123–126]. If the atomic EXAFS originates from the scattering of the photoelectron at the bonding electrons, the AXAFS contribution to the entire fine structure of the x-ray absorption coefficient should be highly directional for systems with strong anisotropic bonding. This is the case for the reconstructed (2 × 1)O/Cu(110) surface system discussed here [131]. There is general agreement that the O atoms are located in a long-bridge position along the [001] direction (see figure 9) forming O–Cu rows on the surface [132–141]. This C_2 symmetry results in a non-spherical scattering potential for the photoelectron. Therefore, a definite angular dependence of the AXAFS features is expected and reported for the first time in our recent work [131]. Obviously, the O–Cu bond in the surface plane is highly directional. There are two different types of bonds between the oxygen atoms and the first two Cu layers: the first bond is between the O atoms (being nearly located in the surface plane) and the two Cu atoms of the first layer. The second bond is to the second layer. This local structure makes the (2 × 1)O/Cu(110) surface an ideal candidate to study the angular dependence of the atomic EXAFS contribution. Therefore, temperature-dependent surface EXAFS (SEXAFS) measurements at the oxygen K edge were carried out for various polar and azimuthal orientations.

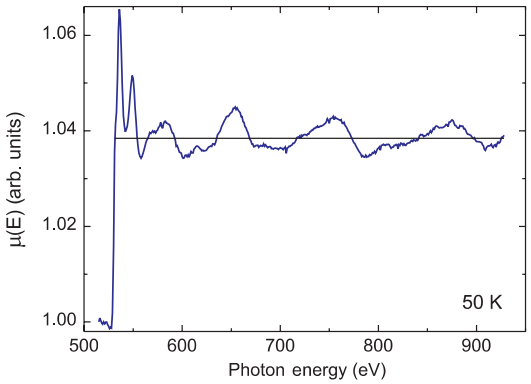

Figure 10. X-ray absorption coefficient $\mu(E)$ at the O K edge for (2×1)O/Cu(110) at 50 K [131]. The spectrum is divided by the spline function for clearer presentation.

It is well known that chemisorption of oxygen on Cu(110) surface leads to an adsorbate induced missing row reconstruction. This reconstructed state was achieved after dosing 12 L of O_2 at room temperature and annealing to 400 K after dosage. With this procedure the saturation coverage of 0.5 ML was achieved which was controlled by investigating the signal to background ratio (edge-jump) versus the oxygen dosage. The experiments were performed at BESSY II in Berlin. We used the U-41 beamline with a collimated plane-grating monochromator (PGM) and a refocusing unit [142]. Further experimental details are given in [131]. For the first time the gap-scan technique was used over an energy range of $\Delta E = 430$ eV (see figure 10). Therefore, the high photon flux provided by the undulator set-up was combined with the capability to scan the energy over an extended range [143, 144]. This guarantees for a high photon intensity with large spectral purity over the entire scan-range without background structures. The absence of background problems allowed for a clear identification of long-period oscillatory features in EXAFS as AXAFS. The SEXAFS data were taken at the O K edge with quasi total electron yield at a polar angle of $\alpha = 90^{\circ}$ (normal x-ray incidence, E-vector parallel to surface) and $\alpha = 20^{\circ}$ (grazing x-ray incidence) in both azimuths ([100] and [1$\bar{1}$0]).

In figure 10, the x-ray absorption coefficient $\mu(E)$ at the oxygen K-edge is presented for the reconstructed system (2×1)O/Cu(110). The SEXAFS oscillations are extracted with a stiff polynomial spline function [130] from the x-ray absorption coefficient $\mu(E)$ (which is divided by the spline function in figure 10 for clearer representation). Often EXAFS data are analysed with special analysis routines like AUTOBK [145]. By the use of those fitting routines the structures in the Fourier transform located below the nearest neighbour contribution are minimized, because it was thought that these features have no physical meaning. This minimization is achieved with a spline function which exhibits a low period oscillation. Hence, the information of the scattering of the photoelectron at the periphery of the absorbing is hidden in the oscillating spline function. If this spline is just taken as a tool in the process of the data analysis and is not investigated on its own the important information about the AXAFS is lost. However, for the analysis presented here a stiff spline function was used. Because of the high intensity of the SEXAFS oscillations for O/Cu(110), the AXAFS feature can be detected very reliably. It turns out that the AXAFS interferes destructively with the nearest neighbour scattering contribution. This results in a reduction of the SEXAFS wiggle at about 680 eV, which can be seen even by eye inspection. The detailed analysis of the SEXAFS wiggles is carried out in k-space as it is presented in the left side of

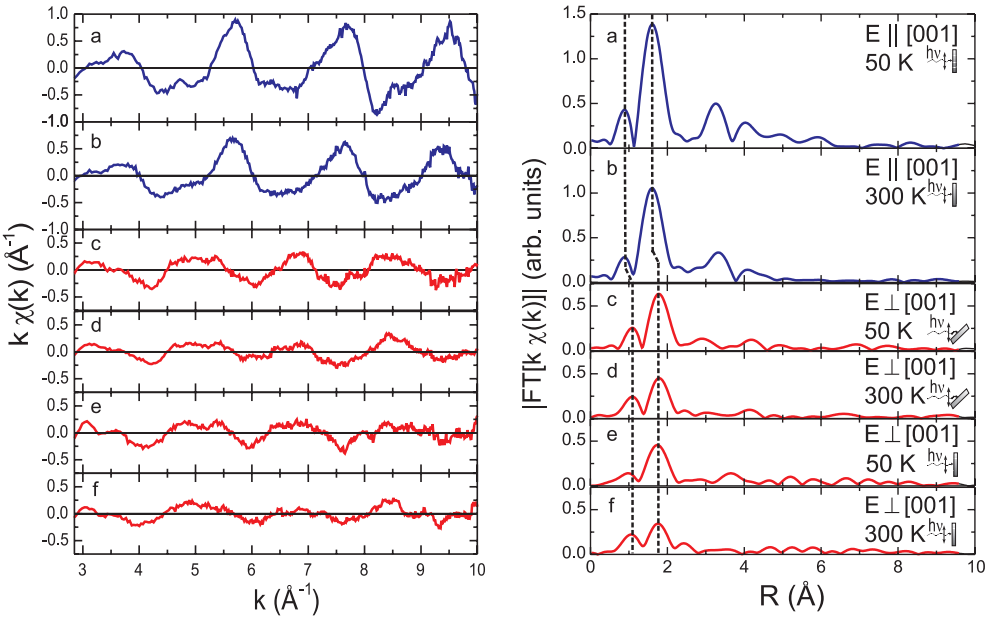

Figure 11. SEXAFS oscillations $k\chi(k)$ (left) and the corresponding Fourier transforms $|FT[k\chi(k)]|$ (right) for (2 × 1)O/Cu(110) for different x-ray incidences and sample temperatures [131]. The AXAFS and nearest neighbour contributions are marked by the dotted vertical lines. The orientation of the E-vector for each experimental set-up is given.

figure 11. The temperature-dependent data (50, 300 K) for the various polar and azimuthal orientations of the crystals are shown. The damping of the SEXAFS signals at 300 K is due to the larger dynamic disorder described by the MSRD $\sigma^2(T)$, which enters into the EXAFS Debye–Waller factor: $\exp[-2\sigma^2(T)k^2]$. From the temperature dependence of $\sigma_i^2(T)$ for every bond i, an Einstein temperature $\theta_{E,i}$ can be calculated that characterizes the bonding strength of every individual bond i [146]. The right side of figure 11 shows the Fourier transforms of the data. As discussed above, the SEXAFS is mainly determined by the two bonds of the oxygen atoms to the Cu atoms (R_{nn} and R_{nnn}). At normal incidence with the E-vector parallel to the O–Cu rows ($\vec{E}||[001]$) the nearest neighbour bond R_{nn} is probed (figures 11(a) and (b)). Whereas at grazing and at normal x-ray incidence with the E-vector perpendicular to the O–Cu rows ($\vec{E} \perp [001]$), the next nearest neighbour bond R_{nnn} of the O atoms to the second layer is analysed (figures 11(c)–(f)). That indeed two different bonds are probed can be seen by looking at the different phases of the SEXAFS oscillations in the k-space (figure 11, left) for (a), (b) compared with (c), (d), (e) and (f). Correspondingly, the main peak position in the Fourier transform (figure 11, right) is shifted to larger distances for (c), (d), (e) and (f), as indicated by the right vertical lines. The reason for the larger intensity of the main peak in the Fourier transforms in (c), (d) compared with (e), (f) is due to the larger effective coordination number $N_i^* = 3\sum_j(\vec{\epsilon}\cdot\vec{r}_{i,j})^2$ for this geometry. Here, $\vec{\epsilon}$ is the unit vector in the direction of the electric field and $\vec{r}_{i,j}$ is the unit vector in the direction of the bond, where j refers to all the backscattering atoms within a backscattering shell i. Fitting the main contributions in the Fourier transforms using FEFFIT [92] with a theoretical standard calculated with FEFF8.2 [91] the bond lengths and the corresponding Einstein temperatures $\theta_{E,i}$ can be determined as given in table 1. From these results the structure given in figure 9 is confirmed. The height of $h = 0.04$ Å of the oxygen atoms above the plane formed by the first Cu layer was determined by optimizing the intensity of the multiple-scattering forward-focusing peak located at about

Table 1. Bond lengths and Einstein temperatures for the nearest and the next nearest neighbour bonds [131].

	Nearest neighbour R_{nn}	Next nearest neighbour R_{nnn}
Bond length R (Å)	1.81 ± 0.03	1.99 ± 0.03
Einstein temp. θ_E (K)	420 ± 40	380 ± 40

3.2 Å in figure 11(a) (right) using the FEFF8.2 code [144]. The next nearest neighbour bond length of the O atoms to the second Cu layer is consistent with a layer expansion of 0.20 Å of the first layer (see d_{12} and d_{23} in figure 9). Similar expansions were found in various other structural investigations of this system [140,147–149]. The slightly larger Einstein temperature of the nearest neighbour bond (table 1) indicates that this bond is a little stiffer compared the next nearest neighbour one. But this anisotropy is small compared to other reconstructed systems (see, e.g. [146]), demonstrating that the bond strengths of the O atoms to the first and the second Cu layer for the present system is nearly isotropic, although the bond lengths are quite different (table 1).

Now, we turn to the investigation of the peak located at about half of the nearest neighbour distance (Fourier transforms (a) and (b) in figure 11) or at half of the next nearest neighbour distance (Fourier transforms (c), (d), (e) and (f) in figure 11), respectively. These contributions marked by the left vertical lines are assigned to the AXAFS contribution. Obviously, these contributions shift systematically according to the bond which is probed. This reveals that these structures located at about 0.9 Å (AXAFS nearest neighbor) and 1.1 Å (AXAFS next nearest neighbour) cannot be artefacts due to possible MEEs as discussed by Filipponi and Di Cicco [119, 120]. This is because MEEs lead to structures at a fixed energy in the x-ray absorption coefficient $\mu(E)$ (see also [150]). Therefore, features that originate from MEEs would show up at the same distance R in the Fourier transform, independent of the measuring geometry. The same argument is true for experimental artefacts which could be due to improper normalization of the data. Hence, the dependence of the AXAFS peak position on the bond being probed is a strong indication that this feature indeed stems from the scattering at interstitial charges between the absorbing and the backscattering atom. For the investigation of the anisotropy of the AXAFS, the Fourier transforms of the SEXAFS oscillations are directly compared at 50 K with the E-vector along ($\vec{E}||[001]$) and perpendicular to the O–Cu rows ($\vec{E} \perp [001]$) (figure 12(a)). The AXAFS peak A shifts to larger distances A' together with the position of the main peak (nearest neighbour: B, next nearest neighbour B'). In order to analyse the phases of the AXAFS, the inverse Fourier transforms of the peaks marked with A and A' are presented in figure 12(b). Interestingly, the AXAFS oscillation of the nearest neighbour bond (solid line) exhibits a maximum around $k \approx 6.3$ Å^{-1} whereas a minimum is determined for the regular SEXAFS oscillations at this k-value (figure 11(a)(left)). This results in a destructive interference of the two contributions leading to a dip in the enveloping amplitude of the complete SEXAFS as it can be detected even by eye inspection in figure 11(a)(left). This is also found for the next nearest neighbour bond: the AXAFS oscillation exhibits a minimum at $k \approx 6.8$ Å^{-1} (dashed line in figure 12(b)) whereas a maximum is found for the regular SEXAFS oscillations (figure 11(c)(left)).

Now, the experimental results are compared to *ab initio* calculations using the FEFF8.2 code [91] based on spherical potentials (muffin tin approximation). The scattering of the photoelectron at interstitial charge densities results in an oscillatory fine structure $\chi_e(E)$ of the atomic x-ray absorption coefficient $\mu_0(E)$ of the embedded atom:

$$\mu_0(E) = \mu_{0,\mathrm{free}}(E)[1 + \chi_e(E)]. \tag{9}$$

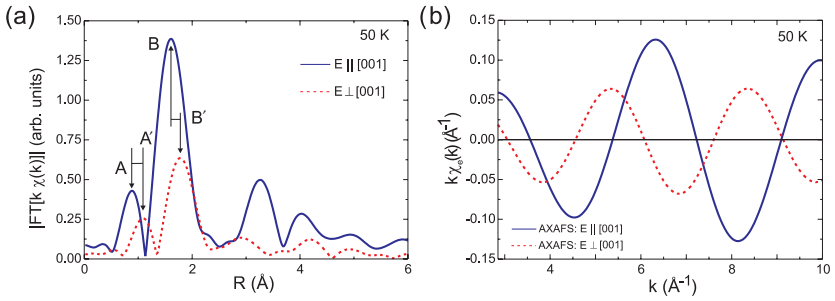

Figure 12. (*a*) Direct comparison of the Fourier transformed SEXAFS data with the E-vector along the O–Cu bond ($\vec{E}$||[001], normal x-ray incidence) and perpendicular to that direction ($\vec{E} \perp [001]$, grazing x-ray incidence). (*b*) Inverse Fourier transform of the AXAFS contributions labelled with A and A' in the left figure [131].

Here, $\mu_{0,\mathrm{free}}(E)$ refers to the smooth atomic x-ray absorption coefficient of the free atom. Therefore, the total x-ray absorption coefficient $\mu(E)$ becomes:

$$\mu(E) = \mu_{0,\mathrm{free}}(E)[1 + \chi_e(E)][1 + \chi(E)]. \tag{10}$$

In this representation of the total x-ray absorption coefficient, the scattering of the photoelectron at the interstitial charges is separated from the scattering at neighbouring atoms. As suggested by Rehr *et al* [117] the AXAFS oscillatory fine structure $\chi_e(E)$ can be described within the muffin tin approximation by

$$\chi_e(E) = -\frac{1}{kR_{\mathrm{MT}}^2}|f_e| \sin(2kR_{\mathrm{MT}} + 2\delta_l^a + \phi_e). \tag{11}$$

Here, R_{MT} is the muffin tin radius, $f_e = |f_e|\,\mathrm{e}^{\mathrm{i}\phi_e}$ is an effective curved-wave scattering amplitude of the interstitial charge density and δ_l^a is the central atom phase shift.

Looking at the AXAFS intensity relative to the nearest neighbour contribution in the Fourier transform in figure 12, the AXAFS is about 30% of the main contribution. However, to determine the intensity of the effective scattering amplitudes for the interstitial charge $|f_e|$ relative to those of the nearest neighbour $|f_{\mathrm{nn}}|$, the intensities seen in the Fourier transform have to be rescaled by $1/R^2$ (see equation (11)). Since the AXAFS contribution is located approximately at half the nearest neighbour distance, the ratio is $|f_e|/|f_{\mathrm{nn}}| \approx 8\%$. Interestingly, in a simplified atomic picture one can assume that each bond consists of 2 electrons (f_e) and each of the nearest neighbour Cu atoms (f_{nn}) has 27 ($3\mathrm{d}^9$) or 28 ($3\mathrm{d}^{10}$) electrons that scatter. Then the ratio becomes $|f_e|/|f_{\mathrm{nn}}| = 2/28 \approx 7\%$. This value is in reasonable agreement with the experimentally determined ratio which supports the interpretation that AXAFS is due to the scattering at the bonding charges while the main EXAFS contribution originates from the charges localized at the nearest neighbour atoms. With the FEFF8.2 code we calculated the atomic x-ray absorption coefficient $\mu_0(E)$. The oscillatory fine structure in $\mu_0(E)$ was extracted with a stiff polynomial spline function [131]. The normalization of the data to a constant edge jump reveals that the calculated AXAFS intensity is about 2% of the edge jump. The calculated AXAFS oscillations are compared to the experimental result in figure 13. A muffin tin radius of $R_{\mathrm{MT}} = 0.94$ Å (dotted line) was calculated by assuming charge neutrality. It turns out that the phase of the calculated AXAFS oscillations are off by about 180°. Since there is charge transfer from the Cu to the O atoms which is not automatically taken into account by the scattering potentials calculated with the program, the muffin tin radius had to be enlarged to $R_{\mathrm{MT}} = 1.11$ Å. This is because the muffin tin radii are kept constant even in the self-consistent field approximation. The phase is in reasonable

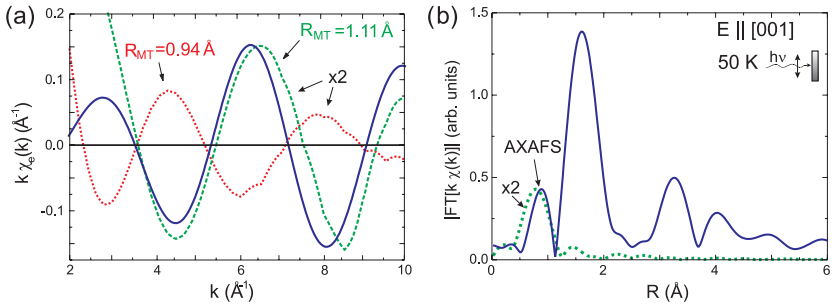

Figure 13. (*a*) Calculated AXAFS χ_e for two muffin tin radii ($R_{\mathrm{MT}} = 0.94$ Å: ·····, $R_{\mathrm{MT}} = 1.11$ Å: - - - -) and the inverse transformed experimental AXAFS contribution for O/Cu(110) (marked with *A* in figure 12) (——). (*b*) Fourier transform of the calculated AXAFS contribution ($R_{\mathrm{MT}} = 1.11$ Å) (- - - -) together with the Fourier transform of the complete experimental SEXAFS oscillations (——) [131].

agreement with the experimental data for the enlarged muffin tin radius. Both calculations had to be multiplied by a factor of 2 to match the experimental intensity. This is probably due to the extended continuum picture used in the calculation that may underestimate the real jump of the potential at the surface. Unfortunately, the anisotropy of the AXAFS peak position in the Fourier transform cannot be calculated using the FEFF8.2 code in the spherical muffin tin approximation. For this purpose a full-potential version of the code is needed which is under development right now.

Our angular-dependent study showed that the position of the AXAFS contribution in the Fourier transform reflects the anisotropy of the bond being probed. This gives the unique opportunity to measure the anisotropy of the local embedded atom potential for the first time. Hence, the investigation of the AXAFS provides a new experimental tool to study non-spherical embedded atom potentials. The combination of experiment and theory will help to study the charge densities that are responsible for the bond, for instance in oxides, in more detail in future works.

4.2. Shape resonances of oriented molecules

After investigating the scattering phenomena of the photoelectron for atoms on surfaces we now turn to the analysis of oriented molecules on surfaces. The focus here will be the broad structures in the continuum region of the x-ray absorption spectra of molecules. These resonances are studied by analysing the angular dependence of *ab initio* calculated NEXAFS spectra of oriented hydrocarbon molecules using a full multiple-scattering formalism. By comparison of the theoretical results to experimental data, the resonance in the experiment can indeed be assigned to a so-called σ^* shape resonance.

In the early works of Dehmer *et al* [151] the origin of these resonances was assigned to the temporary trapping of the excited core electron by a centrifugal barrier of the molecular potential in a quasi-bound state. However, it will be discussed below that these σ^* shape resonances can be described by the scattering of the photoelectron at the intramolecular valence region. A centrifugal barrier is not necessary since even a square-well potential can produce such a resonance [152, 153]. Important case studies, concerning the σ^* shape resonance, are carried out for the linear hydrocarbon molecules ethane (C_2H_6), ethylene (C_2H_4) and acetylene (C_2H_2). These molecules are prototypes with a single, double and triple bond, resulting in a systematic variation of the C–C bond length $d_{\mathrm{C–C}}$ (figure 14).

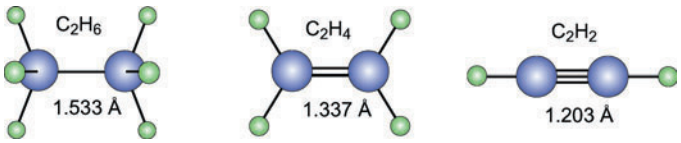

Figure 14. Schematic representation of the hydrocarbon molecules ethane (C_2H_6), ethylene (C_2H_4) and acetylene (C_2H_2). The C–C distances are given for the gas phase [173].

Therefore, the influence of the molecular geometry on the experimental results can be directly studied. Numerous experimental [11, 152–159] and theoretical [160, 161] studies have been performed on these hydrocarbon molecules, however, no systematic quantitative analysis of these resonances was carried out. While the empirical correlation between resonance energy and internuclear separation was investigated experimentally [11, 16, 154, 159, 162], a full analysis including oscillator strength and spectral shape is still missing. In several instances a pronounced asymmetry in the spectral shape of these resonances was observed. This feature was first discussed in terms of a strong coupling between vibrational and electronic motion leading to a breakdown of the Franck–Condon principle, as was observed in the case of the nitrogen molecule [151]. A cross-section of several Mbarn was calculated at the resonance maximum, however, no quantitative comparison to experimental data was performed. Interestingly, the existence of a shape resonance in the photoabsorption spectra of C_2H_6, C_2H_4 and C_2H_2 has been recently questioned by Kempgens *et al* [163, 164], who report to have measured the photoionization cross-section of the C 1s main line by means of angle resolved photoemission. The authors concluded that the broad feature in the absorption spectra of these hydrocarbons is caused by multiple-electron excitations, in contrast, Sorensen *et al* [165] found a non-Franck–Condon-like behaviour in the resonance region and took this as an indication for the presence of a shape resonance. This was concluded by separating the C 1s photoelectron spectrum of C_2H_4 into contributions from the C–C and the C–H stretch modes. Furthermore, Thomas *et al* [166] supported the existence of shape resonances by measurements of the photon energy dependent $1\sigma_u/1\sigma_g$ intensity ratio in the C 1s photoelectron spectra of C_2H_2. Therefore, a precise calculation of cross-sections and comparison to experimental data will help to solve this inconsistency. This allows us to illustrate for well known test cases, that quantum mechanical scattering theory does adequately describe the absorption coefficient.

A breakthrough in terms of the quantitative analysis of the σ^* shape resonance is the investigation of oriented molecules on surfaces at low temperatures [167, 168] as discussed here. These molecules are found to be weakly distorted, as compared to the gas phase, which allows for an identification and study of the continuous evolution of spectral features. For oriented molecules on surfaces it is possible to probe the angular dependence of the various transitions since the x-ray E-vector can be aligned parallel or perpendicular to the molecular C–C bond axis. In contrast, the study of the angular dependence of the σ^* shape resonance in the gas phase cannot be easily performed. Rabus and co-workers [152, 153] suggested a quantum mechanical scattering model which was applied in earlier experimental works. This model is based on the principle of the 'giant resonance' presented by Connerade [169]. Thereby, the asymmetric lineshape with the high-energy tail is reproduced satisfactorily, which is a result of general considerations in the theory of scattering from a bound state into the continuum (a quasi-bound final state). However, in this simple model only the resonant part of the spectrum is calculated and, hence, an adjustable parameter is used to scale the resonance intensity to the atomic continuum. Therefore, the calculation of absolute cross-sections is not straightforward using the simple square-well potential. In contrast, more realistic potentials and the advanced treatment of electron scattering improved the theoretical

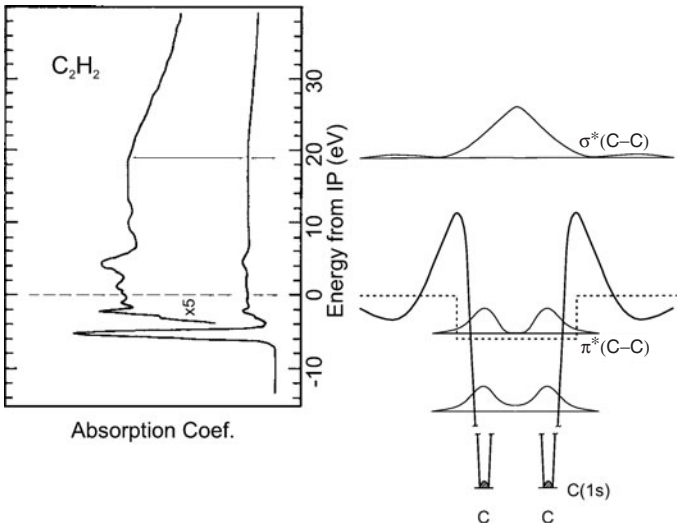

Figure 15. A schematic representation of processes leading to the existence of resonant features in the continuum [168]. The C 1s photoelectron is scattered at the intramolecular potential. Following an early analysis, an effective square potential (- - - -) of about 6 eV depth can describe the asymmetric resonance in the continuum. Here, gas phase data from the literature are shown [154]. One has to note, that the potential barrier can be lower than the resonance energy which highlights that a tunnelling process is not necessary. The orbital density for the shape resonance according to this effective potential scattering model [152, 153] is presented. Antibonding valence levels and a bonding one are also shown schematically.

description which is implemented in the FEFF8 code [91] applied here. An earlier version of this *ab initio* code, which did not include FMS, was used to calculate the photo-absorption cross-section of other small molecules like N_2 and O_2 [170, 171]. In these works, a comparison to NEXAFS spectra from physisorbed N_2 gave a satisfactory agreement between theory and experiment [170]. For O_2 it was found that high-order scattering (up to 13 backscatterings) is needed to reach convergence in the calculations. Thereby, the enhancement in oscillator strength can be reproduced, which results in the σ^* shape resonance close to the edge [170]. Here, we present further theoretical results on these molecules and compare those to spectra of oriented molecules on surfaces. The importance of the molecular vibrations and the effects of a finite temperature on the shape resonance energy and spectral shape are highlighted. Furthermore, we estimate the importance of the existence of the hydrogen atoms in the spectra and analyse the importance of MEEs.

For the basic understanding of the photo-excitation of a diatomic molecule a schematic description is given in figure 15. After monochromatic x-ray excitation the photoelectron can be scattered at the intramolecular potential resulting in various 'single-electron' resonances. Already in the early 'giant resonance' approach it was shown that shape resonances can be described by calculating the scattering of the photoelectron in the intra-molecular valence region. Modelling the scattering potential by a simple square potential (dashed line in figure 15) it is found that scattering from this effective potential (6 eV deep) can lead to a feature at about 17 eV above the ionization potential (IP) [152]. This analysis demonstrates that a tunnelling process is not necessary since the important contribution is the scattering of the photoelectron at the inner part of the effective potential [152, 153]. The simple potential in figure 15 illustrates the fundamental quantum mechanical process of the scattering of the photoelectron at a potential well. This basic process is expected to occur upon photon absorption and must

be considered before higher order multi-particle processes are discussed. In the case of MEEs more than one-electron is involved. One possibility is the simultaneous ejection of a second electron from a valence orbital into the continuum, leading also to a variation in the cross-section. Also a double-excitation in the continuum could occur, with a valence electron being promoted to an unoccupied orbital lying below the IP. Here, we present a basic case study for quantum mechanical scattering [167, 168] in a quantitative manner. The MEEs [172] are discussed on a qualitative base and are not dominant in the present case. Since it can be questioned whether the simple square potential is an oversimplification, we have performed state-of-the-art *ab initio* calculations.

These calculations were performed with the program FEFF8 [91]. Using this code, the x-ray absorption coefficient $\mu(E)$ in the near-edge region (NEXAFS) as well as in the extended energy range (EXAFS) can be calculated. The theory is based on a relativistic Green's function formalism, using an *ab initio* self-consistent field (SCF) real-space multiple-scattering (RSMS) approach for a defined cluster of about 100 atoms. The free atom potentials of each atomic type are calculated self-consistently, using a relativistic Dirac–Fock atomic code. The total muffin tin scattering potentials are obtained iteratively, by successive calculations of the density matrix and then of the potential until self-consistency is reached. These SCF potentials are essential for an accurate determination of the Fermi level. For the purpose of an improved calculation of NEXAFS spectra, a FMS approach is implemented into the code. FEFF8 calculates the excitation of a photoelectron in a muffin tin-like scattering potential of the cluster for a fully relaxed core hole. It does not include multi-electron effects like shake-up excitations. We use the advanced version (full matrix inversion, self-consistent potentials) and present the first angular dependent and variable cluster size calculations. Thereby, we study the effect of a stretched C–C bond and the influence of the H atoms as well as the Cu substrate. Our calculated values of the ionization potential (IP) for the three molecules given in [167] are in remarkably good agreement with the well known IP values. This means that the self-consistent calculation of the molecular potential determines the IP accurately within a few tenths of an electronvolt without any adjustable parameter. The onset of a finite cross-section starts below the IP in the regime of unoccupied bound states by using an extended continuum model ansatz. Figure 16 shows the C 1s NEXAFS spectra for a single free molecule of C_2H_6, C_2H_4 and C_2H_2 calculated for different orientations ($\theta = 0^\circ, 10^\circ, 45^\circ, 90^\circ$; see inset of figure 16(*b*)). The molecular geometry was taken from [173] as shown in figure 14. The intensity of the calculated cross-section ($T = 0$ K) is given in absolute units of Mbarn. For all three hydrocarbons a broad feature in the continuum regime is visible, which shows an asymmetry with a tail on the high-energy side. A clear angular dependence of this structure can be recognized, having a maximum intensity for the E-vector parallel to the C–C bond ($\theta = 90^\circ$), decreasing for 45° and 10° and vanishing completely for $\theta = 0^\circ$. This behaviour is in correspondence with predictions for the angular dependence of a σ^* shape resonance [16, 155, 157]. From the angular dependence in figure 16 we can distinguish between the atomic cross-section $\mu_0(E)$ (bold-dotted line) and the σ^* shape resonance. It can be seen that the resonance cross-section is 1 to 2 times larger than μ_0 at this photon energy, i.e. about 4 Mbarn at $T = 0$ K. The different bond strengths between the C atoms in the three hydrocarbons lead to varied bond lengths $d_{C–C}$ (figure 14). Figure 16 shows that the maximum position E_{max} of the resonance moves to lower energies for larger bond length $d_{C–C}$, in agreement with the scattering picture of the potential well. For C_2H_2 it is located at 311.6 eV, shifting to 301.8 eV for C_2H_4 and to 294.1 eV for C_2H_6. The dependence of this continuum resonance on the C–C bond length is further indication that the feature is a σ^* shape resonance. The present multiple-scattering calculations indicate the existence of a resonance for C_2H_6 in the continuum part of the spectrum, while earlier studies [160, 161] predicted a σ^* resonance of predominantly C–H character below the threshold. However, here

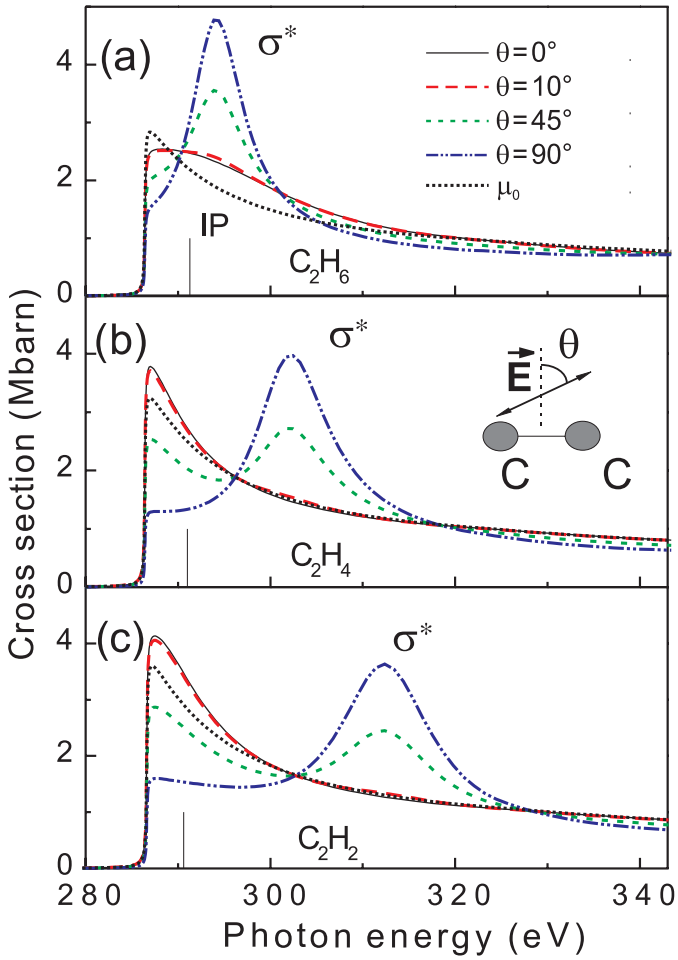

Figure 16. Calculated C 1s NEXAFS spectra of C_2H_6 (*a*), C_2H_4 (*b*) and C_2H_2 (*c*) for different orientations of the E-vector of the photon beam with respect to the intramolecular C–C bond [167]. $\theta = 0^\circ$ corresponds to a perpendicular orientation, $\theta = 90^\circ$ to a parallel one (see inset of (*b*)). The energy position of the σ^* shape resonance is changing depending on the C–C bond length of the hydrocarbon molecule. The atomic background $\mu_0(E)$ is indicated by the bold dotted line and the vertical lines represent the calculated ionization potentials.

we obtain a resonance maximum for C_2H_6, close to but above the IP (figure 16(*a*)). This is supported by angular-dependent NEXAFS measurements of oriented C_2H_6 molecules on Cu(100) [152, 156]. A resonance of σ symmetry is identified above the threshold in this case, indicating that this feature possesses mostly C–C character. Here, an isolated feature of C–H character is not identified.

With this study it is verified that the σ^* shape resonance can be accurately described by calculating multiple-scattering effects of the excited photoelectron between the C atoms of the hydrocarbon molecule. We will show that the properties of this quasi-bound state will depend on intramolecular properties alone and less on neighbouring atoms. In figure 17 the theoretical spectra are shown for three different 'chemical environments' of the C–C bond in C_2H_4. The calculations are performed for two different values of $d_{C–C}$: the value 1.337 Å corresponds to the gas phase bond length of ethylene, and 1.45 Å is the value for the molecule chemisorbed on

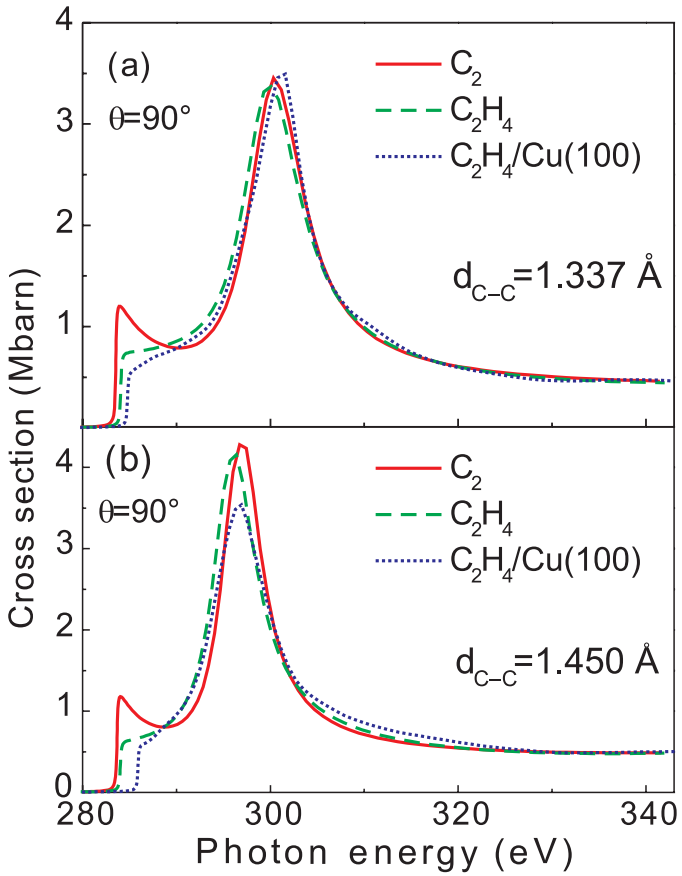

Figure 17. (*a*) Calculations for an artificial C_2 molecule, a C_2H_4 molecule and a C_2H_4 molecule adsorbed on Cu(100) for a fixed C–C bond length of 1.337 Å. (*b*) Corresponding calculations like in (*a*) using $d_{C-C} = 1.450$ Å [167].

the Cu(100) surface [156]. The solid lines depict the calculations for an artificial C_2 molecule without H atoms, while the dashed lines represent the calculations for an ethylene molecule, and the dotted ones are for a C_2H_4 molecule adsorbed flat on a Cu(100) surface [158, 167]. In both calculated sets in figures 17(*a*) and (*b*) no remarkable changes of the shape and the position of the resonances in the spectra, caused by the modification of the chemical environment, can be noticed. But as already described in figure 16, the resonance shifts to lower energy for the stretched C–C bond.

In earlier experiments, a relationship between d_{C-C} of the hydrocarbons and E_{max} was found for molecules adsorbed on different metal surfaces. Here, we analyse the NEXAFS spectra of ethylene, which was physisorbed (dosing 1 L C_2H_4 at 25 K) and chemisorbed (dosing 1 L C_2H_4 at 60 K) on a Cu(100) surface. The C *K* edge NEXAFS spectra for normal (90°) and grazing x-ray incidence (20°) of submonolayer coverages of ethylene were recorded at the synchrotron radiation facility BESSY II. The angular dependence of the observed molecular π^* and σ^* shape resonances can be seen in figure 18, where we plot the difference spectra $\mu(90°)$–$\mu(20°)$ for C_2H_4. Here, we will not discuss the π^* resonance at 285 eV and the C–H resonances around 289 eV. The intensity of the σ^* shape resonance for 90° is larger as compared to 20° and vice versa for the π^* resonance, which shows that the molecules lie flat

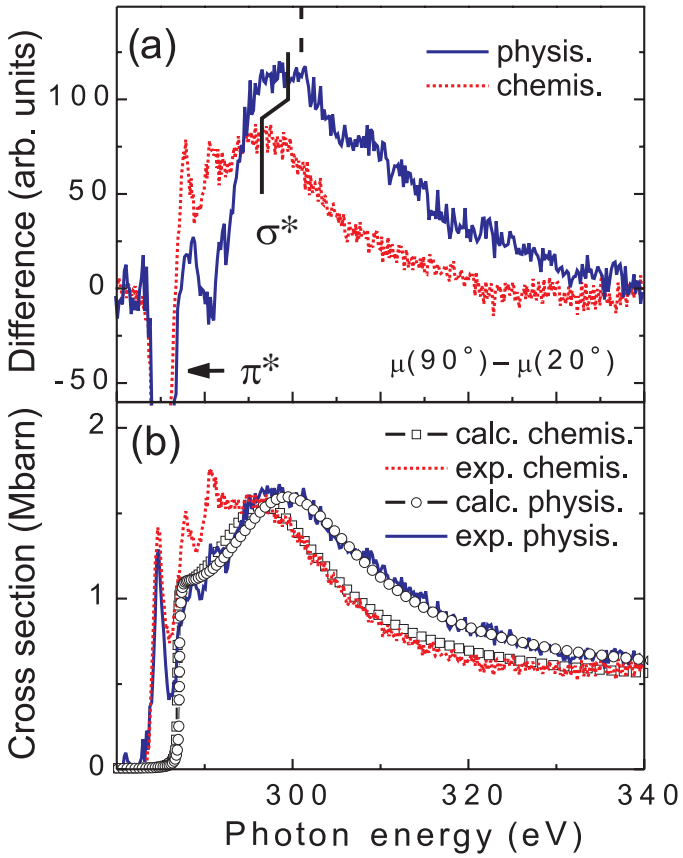

Figure 18. (*a*) Difference spectra $\mu(90^{\circ})$–$\mu(20^{\circ})$ of a submonolayer C_2H_4 on Cu(100), almost physisorbed at 26 K (——) and chemisorbed at 60 K (· · · · · ·) [167]. The dashed line at the top is indicating E_{max} for gas phase ethylene. (*b*) Experimental and calculated C 1s NEXAFS spectra of C_2H_4 adsorbed on a Cu(100) surface. Both the spectra of the almost physisorbed and the chemisorbed state are shown. In experiment and theory, a shift of the σ^* shape resonance of the chemisorbed phase towards lower energy can be recognized.

on the Cu surface. For the chemisorbed species the shape resonance peak is located at a lower energy compared with the physisorbed case, which reveals a stretching of the intramolecular distance due to the chemisorption. This stretching can be explained by a charge transfer from the Cu surface into the antibonding π^* orbital of ethylene and hence the weakening of the C–C bond [16]. From figure 18(*a*) we obtain $E_{max} = 299.5$ eV and 296.5 eV, for the physisorbed and the chemisorbed species, respectively. The shift of 1.5 eV of the resonance with respect to the gas phase (dashed line) illustrates that C_2H_4 is weakly bonded. The displacement is larger for the chemisorbed phase (4.5 eV), showing a stronger interaction with the substrate. In figure 18(*b*) we present calculations for both cases, together with the corresponding experimental data for 90°. In the experiment, the atomic positions vary slightly due to thermal vibrations and disorder. In order to take this into account in our calculations, we introduced damping by the Debye–Waller factor. Since a FMS approach is used in the FEFF8 code, the treatment of disorder in terms of Debye–Waller factors is only approximate. Turning off this approach, i.e. using the path expansion in FEFF8, we estimate a value for the MSRD of $\sigma^2 \sim 0.0036$ Å^2 for single-scattering. This value may appear high, but in a recent

work [165] it was found that the intramolecular vibrations are influenced by the excitation of the photoelectron into an antibonding state (σ^* shape resonance). Therefore, the interpretation of the MSRD in the present analysis of the σ^* shape resonance is more complicated as compared to ground state properties (see, e.g. [168]). Since we only use a single scaling parameter to match theory and experiment, the agreement is fairly good. We find no indication for satellite contributions as identified by Kempgens *et al* [163, 164]. They may either (i) be negligible for physisorbed molecules or (ii) do not play a role for the angle integrated detection scheme used here. In principle, only a full angle integration in the photoelectron yield leads to a measure of the absorption coefficient. Kempgens *et al* [163, 164] used only a fixed angle experimental electron analyser set-up with finite acceptance angle, but did not take non-dipolar effects in the angular distribution of the photoelectrons into account. The importance of such effects for a full analysis of absolute oscillator strengths was pointed out in recent studies [174–176].

A combined theoretical and experimental case study of scattering at potential wells applied to surface science and NEXAFS is presented. It is the advantage of today's theory is that one can 'disassemble' the molecule, and thereby study the influence of the hydrogen atoms and the metal substrate on the resonance.

5. Magnetism of ultrathin 3d, 5d layers and rare earth crystals

Nowadays, the investigation of layered magnetic structures is a very active field of research since these nanostructures offer the possibility to build new materials with unique magnetic properties. On the one hand, these nanostructures are of great importance for technical applications, e.g. as magnetic storage devices. On the other hand, the new magnetic properties of these devices are not completely understood regarding the fundamental mechanisms. The development of magnetic storage devices that consist of alternating ferromagnetic and so-called 'non-magnetic' layers is dramatic: since the discovery of the 'giant' dependence of the magnetoresistance (GMR) on the alignment of the magnetic moments in the individual ferromagnetic layers in those nanostructures in 1988 [177, 178] the field is rapidly growing. Nine years later, IBM announced read heads for magnetic storage devices (hard disk drives) [179]. Similar nanostructures are used as non-volatile magnetic random access memory (MRAM) devices [180]. Today, such magnetic nanostructures are even discussed for the realization of programmable magnetoresistive elements [181]: since the output of such magnetic logic element is non-volatile, it is expected that those structures can improve the clock speed of future processors dramatically. This is because the time-consuming transfer of the output to the cache memory as it is done for the transistor based devices is not required any more. One of the important mechanisms that determines the magnetic properties of these layered structures is the long-range oscillatory interlayer exchange coupling. This determines the coupling of the magnetic layers via the 'non-magnetic' ones. Various works have been carried out to study this phenomenon in detail (see, e.g. [182–186] and references therein). The magnetic layers that are investigated here are coupled ferromagnetically by the interlayer exchange coupling. In this review we will focus on the induced magnetism in the 'non-magnetic' layer at the interface to the magnetic layer. Interestingly, this effect is often neglected when the magnetic properties, e.g. of magnetic storage devices are discussed [181, 187]. This approach is justified if the properties of the films are not dominated by their interfaces, i.e. if the film thickness is in the range of several hundred angstrom. In contrast, for reduced film thicknesses down to few atomic layers, induced moments at the interfaces of the 'non-magnetic' layers due to hybridization become prominent. It turns out that in this ultrathin limit the induced moments significantly determine various magnetic properties like the magneto-transport properties [188], the magneto-optic response [189], and the magnetic anisotropy

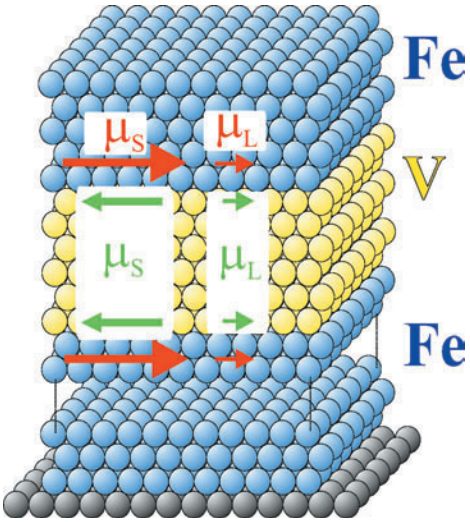

Figure 19. Schematic representation of a prototype Fe–V–Fe(110) trilayer. The relative orientations of the spin (μ_S) and the orbital moments (μ_L) determined by XMCD are given for Fe as well as the induced moments in V.

[190,191]. However, these properties are the crucial ones that will determine if these magnetic structures can be used in the future, as, e.g. advanced storage devices or even programmable magnetoresistive elements. Hence, a detailed understanding of the induced magnetism in layered structures is mandatory.

A prototype structure for the investigation of the induced magnetism is a Fe–V–Fe(110) trilayer (figure 19). Here, the iron layers are the ferromagnetic ones whereas the vanadium layers represent the 'non-magnetic' spacer. An induced total magnetic moment $\mu_{\mathrm{tot}}^{\mathrm{V}}$ is determined in V at the interface which is aligned antiparallel to Fe. In this case magnetometry that measures the entire sample, e.g. vibrating sample magnetometry (VSM) or superconducting quantum interference devices (SQUID), detects a reduced magnetization. If the spacer layer is assumed to be non-magnetic, then erroneously, a reduced moment per atom could be concluded for the ferromagnetic layers in the multilayer. This demonstrates the need for an element specific magnetometry which allows for the separation of the magnetism of the ferromagnetic layer from the spacer layer. The XMCD technique fulfils this demand: for different elements the x-ray absorption edges are located at different photon energies. Therefore, the magnetism of each element in the sample can be analysed separately by selecting the photon energy of the absorption edge. This element specificity was utilized here in order to clarify the inconsistency between earlier theoretical [188,192,193] and experimental works [194,195] concerning the range of the polarization in V.

Furthermore, the XMCD technique is able to disentangled the total magnetic moment into the spin moment μ_S and the orbital moment μ_L, and to determine their relative orientation. Another established technique to study μ_S and μ_L is the ferromagnetic resonance (FMR) which determines the g-factor (for details see, e.g. [186,196]). These quantities are related by [85,86]

$$\frac{\mu_L}{\mu_S} = \frac{g-2}{2}. \tag{12}$$

However, like VSM and SQUID, the FMR technique measures the entire sample. Therefore, an effective g-factor g_{eff} is determined [197,198]. In contrast, the XMCD technique can provide

the g-factors for the individual layers [199, 200] which are g^{Fe} and g^{V} by analysing the ratio μ_L/μ_S element specifically for the case given in figure 19. The XMCD results demonstrate that the induced spin and orbital moments in V are aligned antiparallel ($g^{\mathrm{V}} < 2$) whereas a parallel orientation is found for Fe ($g^{\mathrm{Fe}} > 2$). Hence, it is obvious from figure 19 that the effective g-factor g_{eff} determined by FMR is larger than the one for the ferromagnetic Fe layers g^{Fe} because the orbital moments μ_L^{Fe} and μ_L^{V} of the Fe and V layers add up whereas the spin moment of V μ_S^{V} (being oriented antiparallel to μ_S^{Fe}) reduces the total spin moment. For the detailed analysis of these results it is not sufficient to discuss the relative orientation of μ_L and μ_S in a qualitative manner but the absolute moments have to be analysed. It turns out that the moments of the heavier 3d element Fe can be safely determined from the XMCD spectra by applying the sum rules [77, 78] whereas the same type of analysis fails for the lighter 3d element V [201–205]. This is because the interaction of the photoelectron with the core hole becomes prominent for the light 3d elements. We were only able to determine absolute moments for the V layers by comparison of the experimental spectra to *ab initio* calculations carried out by Minár in the group of Ebert [201]. It is the strength of these calculations that the spectral distribution of the isotropic spectra $\mu(E)$ as well as the dichroic ones $\Delta\mu(E) = \mu^+(E) - \mu^-(E)$ can be determined (see, e.g. [53]). The detailed fine structures of these spectra can be identified experimentally and are then compared to the various features in the calculated spectra. Only by this interplay between advanced theoretical calculations and experimental spectra with high energy resolution, can the magnetic ground state properties of vanadium be determined. Using the same procedure, the magnetic moments of the light transition metals (TM) Ti, V and Cr in Fe–TM–Fe were determined. These experimental results are then systematically compared to the apparent moments determined with the integral sum rule analysis [205].

It is clear that in an atomic framework the relative orientation of μ_L to μ_S follows the expectations of the third Hund's rule: in this atomic model Fe represents the case of a more than half-filled 3d shell and a parallel alignment of μ_L^{Fe} and μ_S^{Fe} is expected (figure 19). Strictly speaking, Hund's rules are only applicable for purely atomic systems. However, interestingly, the third Hund's rule also holds for various solids as for example determined by our XMCD results for Fe and V layers. For the moments induced in V the third Hund's rule predicts an antiparallel alignment of μ_L^{V} and μ_S^{V} since in an atomic framework vanadium represents the case of a less than half-filled 3d shell. Also this antiparallel alignment for V (see figure 19) is found experimentally. However, we will show that this simple picture does not hold for induced moments in general. As will be discussed in section 5.1 for the induced moments in 5d metals, the third Hund's rule breaks down for the case of W in Fe–W multilayers [206], whereas it still holds for Ir in Fe–Ir multilayers and Pt in Ni–Pt multilayers. For the latter case a complete profile of both the ferromagnetic Ni layer and the induced moment in Pt could be determined by XMCD [207]. The breakdown of the third Hund's rule for W demonstrates that band-filling and geometrical effects have to be taken carefully into account to model the relative orientation of μ_L and μ_S theoretically [208, 209]. The sensitivity and the resolution of the experimental XMCD allows for a detailed comparison with theoretical studies [210] which were stimulated by our results. In addition, the anisotropy of the orbital moment $\Delta\mu_L$ was investigated by angular-dependent measurements at the $L_{2,3}$ edges of both constituents of the multilayered Ni–Pt structures, i.e. the ferromagnetic layer (Ni) in the soft x-ray regime [211] and the 'non-magnetic' layer (Pt) in the hard x-ray range [212]. These anisotropies in the orbital moment are the microscopic origin of the magnetic anisotropy, and are therefore of fundamental as well as technical interest.

In the discussion above, the induced magnetism in 3d and 5d elements at the interface to ferromagnetic layers is pointed out. In the case of rare earth metals, the local 4f moments induce

a spin-polarization of the 5d band. This polarization of the conduction 5d electrons establishes the ordering of the 4f moments through the exchange interaction [213, 214]. Therefore, the investigation of the induced moments in rare earth materials is of high interest for a fundamental understanding. Furthermore, compounds consisting of rare earth and 3d elements are of technical interest since they are used for high-performance permanent magnets [215]. For these materials the hybridization of the transition metal 3d band with the rare earth 5d band is of importance. The investigation of the induced 5d magnetism for rare earth metals is made possible by the shell-selectivity of the XMCD technique. However, the detailed analysis of the fine structure of the L_3 and L_2 edge XMCD demonstrates that not only electric dipolar contributions (E1: $2p \rightarrow 5d$) but also electric quadrupolar contributions (E2: $2p \rightarrow 4f$) exist in the x-ray absorption spectra, as it was discussed theoretically [216–219] and has been shown experimentally for rare earth compounds [220–222]. The experimental spectra discussed in these works present even more complicated fine structures in addition to the existence of the E1 and E2 transitions, because of the rare earth 5d—transition metal 3d hybridization. Therefore, the XMCD of single-element rare earth single crystals will be discussed here to achieve a more complete understanding of the physical origin of the spectroscopic fine structures including electric quadrupolar and dipolar contributions. In earlier works the E2 contributions were identified by angular-dependent measurements [220, 222–224]. Unfortunately, the disentanglement of the E1 and E2 spectral distributions cannot be done easily with this procedure, because for the angles investigated, the spectra present an overlap of the two contributions. Therefore, we present a different approach here, i.e. the comparison of the fine structure in the experimental Tb XMCD with theoretical calculations. In the calculations various effects can be switched on and off easily, and therefore the E1 and E2 contributions can be separated [97]. Hence, the shell-specific information can be extracted from the experimental data, i.e. the contributions from the 5d density of states can be separated from the 4f ones. Interestingly, an apparent antiparallel orientation of the induced 5d moments to the 4f can be determined erroneously by applying the integral sum rule analysis to the experimental spectra. It will be shown in section 5.3 that these results are in conflict with standard magnetometry investigations from which a parallel alignment of the 5d and 4f moments is expected. By comparison of the experimental data to *ab initio* calculations [83] it is shown that the spin-dependence of the E1 transition matrix elements is responsible for the erroneous results of the standard analysis procedure.

A precise investigation of the $L_{2,3}$ edge XMCD of rare earth metals reveals that a clear oscillatory fine structure can be identified in the dichroic spectra in the extended energy range—the magnetic EXAFS (MEXAFS). This oscillatory fine structure originates from the spin-dependent scattering of the photoelectron. It turns out that MEXAFS is relatively large for rare earth elements normalized to the near-edge XMCD signal in comparison to the dichroic $L_{2,3}$ edge signal of the ferromagnets Fe, Co and Ni. In the case of the 3d metals the $L_{2,3}$ edge XMCD and MEXAFS scale with the 3d moment. In contrast, the $L_{2,3}$ edge XMCD of the rare earths is dominated by the dipole transitions and scales with the induced 5d moment, whereas the MEXAFS intensity is essentially proportional to the 4f magnetic moment. Therefore, a relatively large MEXAFS fine structure affects the near-edge signal for the rare earth metals. Since the temperature dependence of MEXAFS originates from the dynamic disorder due to lattice vibrations (EXAFS Debye–Waller factor) and the spin dynamics, a larger damping with temperature is found for MEXAFS in comparison to XMCD [225–227]. EXAFS depends on the local environment of the absorbing atom. Thus, one goal is to determine whether the local spin fluctuations differ from the ones that determine the long-range ordering. Therefore, the two contributions to the temperature dependence (lattice vibrations and spin dynamics) have to be separated. Surprisingly, since the pioneering magnetic EXAFS works of Schütz *et al* [228],

no comprehensive theoretical description exists for the temperature dependence of MEXAFS. To overcome this drawback, we present a new procedure which models the spin-dependent density of states by subtracting the experimental normal EXAFS oscillations which are shifted in energy by $\Delta E(T)$. This means that the MEXAFS oscillations at a specific temperature T are simulated using this procedure just by fitting the only free parameter, $\Delta E(T)$, so that the modelled MEXAFS intensities match the experimental ones. Since the experimental EXAFS is used for the modelling, the temperature-dependent damping due to the EXAFS Debye–Waller factor is automatically included and the temperature dependence of $\Delta E(T)$ is only due to the spin-dynamics. Furthermore, we carried out *ab initio* calculations in order to separate multiple-scattering (MS) from the single-scattering (SS) contributions. Interestingly, it is found that for the investigated rare earth metals, Gd and Tb, the multiple-scattering oscillations interfere destructively with the single-scattering oscillations. This is different from what we know for 3d transition metals where a clear enhancement of these MS paths was found [229, 230].

This section is structured as follows: first, examples for the L edge XMCD will be given which allow to investigate induced moments in 5d and 3d metals. This will be followed by the analysis of the rare earth XMCD. The final example will be given for the extended energy range where the MEXAFS of rare earth metals will be analysed.

5.1. Induced moments in 5d transition metals

The multilayered structures studied here consist of ultrathin 3d and 5d films. A major number of atoms is located at the interfaces and therefore, the investigation of the interfacial properties is crucial. A prominent effect is the occurrence of induced moments in the 5d transition metal elements at the interface. It is discussed in literature that these induced moments significantly govern, e.g. the magneto-optic response [189], the magneto-transport properties [188] and the magnetic anisotropy [190, 191]. The polarization of the 5d metals due to hybridization at the interface with ferromagnetic transition metals is studied here for well characterized Fe–W, Fe–Ir [206] and Ni–Pt [207, 211] multilayers. This allows for the analysis of trends in the induced magnetic properties along the 5d transition metal series. Furthermore, the results for the induced magnetism in layered systems as presented here can be compared to the outcome of earlier investigations of 5d impurities in Fe. Thereby, the similarities and differences in the induced magnetism in layered systems are compared to impurities.

First, the results for the Ni–Pt multilayers will be discussed. These layered structures are of fundamental, as well as technical, interest: they are prototypes of magneto-optic recording media since they present a perpendicular magnetization at room temperature and a clear maximum of the Kerr rotation is detected in the blue wavelength regime [231]. Surprisingly, the fundamental question of the role of Pt in these multilayers was not completely answered. Therefore, a thickness-dependent XMCD study *both* at the Ni $L_{2,3}$ edges in the soft x-ray regime *and* the Pt $L_{2,3}$ edges in the hard x-ray regime was carried out to construct a complete magnetic moment profile [207]. This is of importance since also the magnetic properties of Ni in these multilayers were debated for layered structures [232, 233] in comparison to NiPt alloys [234]. The experimental results are compared to self-consistent calculations by means of the tight-binding linearized muffin tin orbital (TB-LMTO) method. The experimental data were achieved in the soft x-ray range at the ID12B (now ID8) beamline with the electron yield detection mode and in the hard x-ray range at the ID12A (now ID12) beamline with the fluorescence yield detection mode at the ESRF. Magnetic fields in the range of 2–5 T were applied in the direction of the x-ray k-vector to ensure complete magnetic saturation at 10 K. The experimental results for a Ni_2Pt_2 multilayer are given in figure 20. The indices

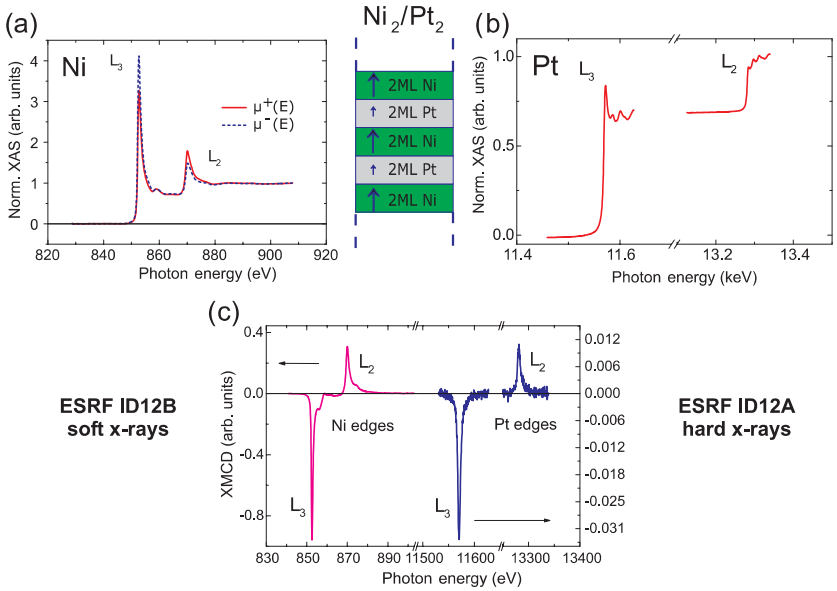

Figure 20. Experimental x-ray absorption spectra for a Ni_2–Pt_2 multilayer: (*a*) x-ray absorption coefficients for right ($\mu^+(E)$) and left ($\mu^-(E)$) circularly polarized x-rays at the Ni $L_{2,3}$ edges in the soft x-ray range, (*b*) isotropic XAS at the Pt $L_{2,3}$ edges in the hard x-ray regime, (*c*) XMCD spectra at the Ni and Pt $L_{2,3}$ edges [237].

refer to the thickness of the constituents of the multilayer, i.e. 2 monolayers (ML) of Ni and Pt for this specific sample. In figure 20(*a*) the x-ray absorption coefficients for right and left circularly polarized x-rays $\mu^+(E)$ and $\mu^-(E)$ are given for Ni. The XMCD difference is presented in figure 20(*c*)(left). For the case of the Pt $L_{2,3}$ edges the isotropic absorption spectra are shown because the difference of $\mu^+(E)$ and $\mu^-(E)$ cannot be made out by eye in this representation. However, an obvious XMCD signal is also detected at the Pt edges as depicted in figure 20(*c*)(right). Although this signal is only about 4% of the L_3 white line intensity, the XMCD signal is clearly larger than the noise demonstrating that indeed an induced moment in Pt is revealed. Since both the Ni as well as the Pt XMCD signals exhibit the same sign at the L_3 and L_2 edge, it can be concluded that the induced moment in Pt is aligned parallel to the Ni moment as indicated in the schematic representation in figure 20. The obvious Ni XMCD signal for a thickness of only 2 ML shows that the existence of so-called 'dead' Ni layers as it has been discussed in [233, 235] can be clearly excluded. For the construction of a magnetic moment profile two sets of samples have to be investigated: for the first set the Pt thickness is kept constant and the Ni thickness is varied; for the second set vice versa. Experimental results are given in figure 21 at the Ni as well as the Pt $L_{2,3}$ edges. In figure 21(*a*) the Ni XMCD results for multilayers with a constant Pt thickness of 5 ML are presented. One has to keep in mind that the XMCD signal scales with the averaged moment per atom of the element investigated. Therefore, the strong decrease of the Ni XMCD for thinner Ni films indicates that the Ni moment at the interface is reduced compared to the Ni bulk value. In contrast, the Pt XMCD signal for multilayers with constant Ni thickness (2 ML) increases for thinner Pt films. This demonstrates that the induced Pt moment is basically located close to the Ni–Pt interface and decreases rapidly for the inner Pt layers. We were able to construct a magnetic moment profile for both constituents for the specific case of a Ni_6–Pt_5 multilayer by using the following two sets of Ni_n–Pt_m multilayer samples: the first

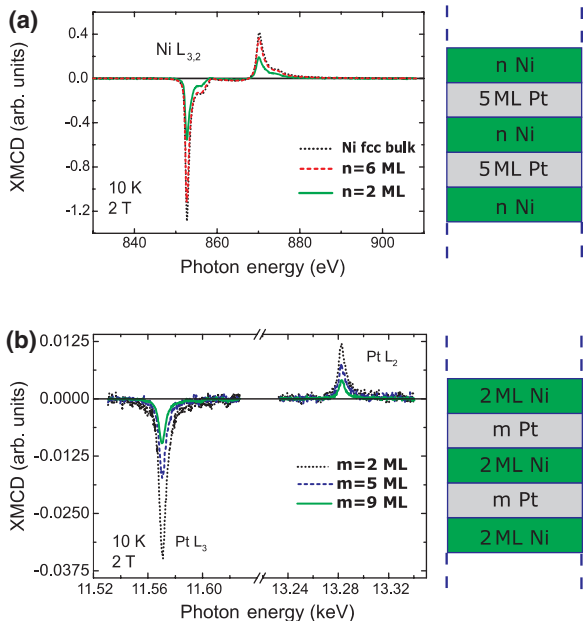

Figure 21. (*a*) XMCD at the Ni $L_{2,3}$ edges for two multilayers with constant Pt thickness (5 ML) and variable Ni thickness (Ni_n–Pt_5). (*b*) Pt $L_{2,3}$ edge XMCD for three multilayers with constant Ni thickness (2 ML) and variable Pt thickness (Ni_2–Pt_m) [237].

with constant Pt thickness ($m = 5$) and variable Ni thickness ($n = 2, 4, 6$), the second set with constant Ni thickness ($n = 6$) and variable Pt thickness ($m = 2, 5$) [207]. Since both constituents basically retain their bulk lattice parameters the residual strain is quite small (0–2%) [240]. Hence, the volume of Ni and Pt is kept constant in our samples and the profile can be constructed from different samples. For the construction of the profile it is assumed that the Ni as well as the induced Pt moments only depend on the position with respect to the interface. The procedure of this construction is explained, e.g. in [236]. In order to discuss absolute magnetic moments the sum rules have been applied (see [237–239] for details). The experimentally derived magnetic moment profile is given together with the outcome of the TB-LMTO calculation in figure 22. For the separation of the contribution of the second- to the third-from-interface Pt layer the ratio of the Pt moments by the TB-LMTO calculation was used. Since the Ni moment per atom differs for Ni_2–Pt_5 and Ni_2–Pt_2 [207], a larger error bar is given for the Ni interface moment. Concerning the induced Pt moment, both experiment as well as theory reveal the same trend: indeed an induced moment is determined at the interface which decays rapidly towards the inner Pt layers. Experimentally, an induced moment of $0.29 \pm 0.03\ \mu_B$ is found and the Ni interface moment is strongly reduced compared to bulk Ni. The calculated results, presented in figure 22(*b*), show a smaller reduction of the Ni interface moment and smaller induced Pt moments. Since perfectly sharp interfaces are assumed in the calculation these deviations can be explained as a small amount of intermixing at the interface [237] due to atomic exchange processes. Since the surface energies of Ni and Pt are quite similar [240] this effect is limited to the interface only. Our experimental results were resumed by another theoretical work where the influence of interface mixing was studied in detail [241]. These calculations show that already an intermixing of 25% located only at the interface reproduces the reduction of the Ni moment. This first magnetic moment profile for both elements of a multilayered structure will help to provide a more complete picture

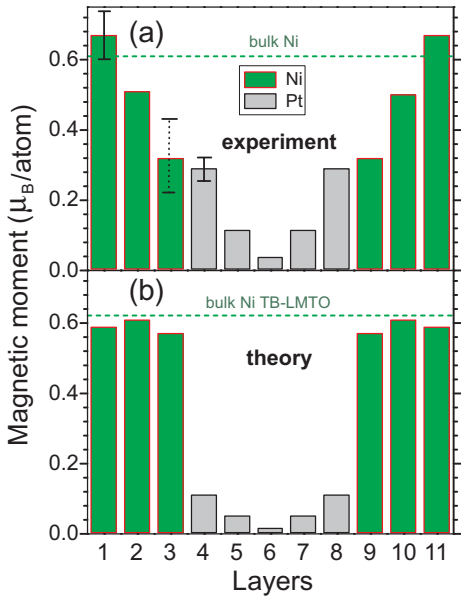

Figure 22. (*a*) Experimental magnetic moment profile for a Ni_6–Pt_5 multilayer. The error bars indicated with solid lines (±10%) are typical for all the moments except the Ni moment at the interface (· · · · · ·). (*b*) Theoretical result for the spin magnetic moments [207].

of the relevant mechanisms that are responsible for the new magnetic properties of these structures.

To understand the perpendicular anisotropy, which is of great technical relevance, we studied the orbital magnetism of a prototype Ni–Pt multilayer in detail. The magnetic anisotropy energy (MAE) determines the easy and hard magnetization directions. It originates from the anisotropy of the orbital moment $\Delta\mu_L$, since the spin moment is isotropic, as discussed in recent works [242–244]. If the spin–orbit coupling can be treated within a second-order perturbation theory, Bruno [245] demonstrated that these quantities are related by:

$$\mathrm{MAE} = \alpha \frac{\xi}{4\mu_\mathrm{B}} \Delta\mu_L. \tag{13}$$

Here, ξ is the spin–orbit coupling constant and α is a scaling factor which takes the electronic structure (which depends, e.g. on the film thickness) into account. A more generalized description was given by van der Laan [246]. The size of α depends on the quantity of the exchange splitting Δ_{ex} compared to the bandwidth W. In the case of 3d transition metals $\Delta_{\mathrm{ex}} < W$ and α is found to be smaller than 1 [247]. To study the anisotropy of μ_L angular-dependent XMCD investigations were performed for the Ni_2Pt_2 multilayered sample. The XMCD spectra for normal x-ray incidence ($\theta = 0^\circ$) and grazing x-ray incidence ($\theta = 75^\circ$) are given in figure 23(*a*). Since clear differences in these spectra at the L_3 edge can be made out, one might erroneously conclude that the angular dependence scales directly on the ratio μ_L/μ_S. However, these differences become smaller [211] when saturation effects in the total electron yield detection mode are corrected [248–250]. Hence, the data must be corrected before the sum rules analysis is applied, by taking into account the different absorption coefficients for the two components of the multilayer [251]. The angular dependence of the orbital moment after these corrections is given in figure 23(*b*) and can be described by [245]:

$$\mu_L(\theta) = \mu_L^\perp + (\mu_L^\parallel - \mu_L^\perp) \sin^2\theta. \tag{14}$$

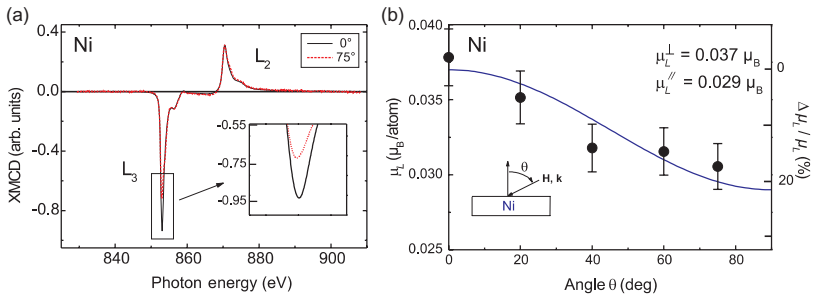

Figure 23. (*a*) Angular dependence of the XMCD spectra (10 K, 5 T) for a Ni_2–Pt_2 multilayer sample at normal ($\theta = 0^\circ$) and grazing x-ray incidence ($\theta = 75^\circ$). The magnetic field was applied in the direction of the x-ray beam. (*b*) Angular dependence of the orbital moment μ_L determined from the angular dependence of the XMCD spectra after correcting them for saturation effects. The solid line is a fit according to equation (14) [211].

Here, $\mu_L^{\parallel}$ is the orbital moment parallel to the film plane and $\mu_L^{\perp}$ is perpendicular to the film plane. Fitting the experimental points given in figure 23(*b*) with this equation, yields the anisotropy of the orbital moment $\Delta\mu_L = \mu_L^{\perp} - \mu_L^{\parallel} = (0.008 \pm 0.004)\ \mu_B$ per atom. The smallness of this difference originates from the size of the orbital moment itself. However, the relative change of $\mu_L(\theta)$ is about 20% with respect to $\mu_L^{\perp}$. This anisotropy of the orbital moment is the microscopic origin that enters into the right side of equation (13). To study the prefactor α in detail, the MAE was also determined macroscopically with magnetization-hysteresis loops measured with VSM [211]. Recently, also element specific hysteresis curves were recorded [212] which show that both the Ni and Pt hysteresis curves follow the same path along the magnetization reversal as seen in the VSM results. This demonstrates that the exchange interaction between Ni and Pt dominates the individual anisotropies of each layer. The MAE is determined directly from these measurements. Combining all these results, the prefactor of equation (13) can be determined to be $\alpha \approx 0.1$ [211] using a value of $\xi = 105$ meV per atom for Ni [252]. This value for α can be compared to results from *ab initio* calculations for ultrathin films on single crystalline substrates as given, e.g. in [253–255]. Since α depends on the bandwidth and the Coulomb integral, its value is not necessarily a constant when the film thickness is varied in ultrathin films or multilayers because the band structure changes as function of the film thickness. This is presented, e.g. in [254], where the volume anisotropy of tetragonally distorted Ni films versus the orbital moment is analysed. These calculations demonstrate that α varies in the range of $\alpha \approx 0.05$–1, which shows that the small values correspond to the ones determined for Ni in Ni_2–Pt_2 multilayers.

Now, we turn to the investigation of induced moments in the 5d metals by traversing the 5d series: the induced moments in Pt have been discussed above for Ni–Pt multilayers. In this paragraph we analyse the lighter 5d elements W and Ir in Fe–W and Fe–Ir multilayers [200,206]. The thickness of the 5d metals W and Ir in each multilayer period was 0.5 nm which corresponds to a thickness of 3.0 ML. The Fe thickness was 1.0 nm. The multilayers were structurally characterized by means of x-ray diffraction and transmission electron microscopy [206]. Similar to the measurements discussed above, the XMCD data were taken at 10 K in large magnetic fields of 5 T. The field was applied normal to the film plane in the direction of the x-ray beam. The x-ray absorption spectra at the 5d L edges for unpolarized x-rays are presented together with the XMCD spectra in figure 24 for (*a*) the Fe–W and (*b*) Fe–Ir multilayers [206]. Obviously, a clear XMCD signal can be observed nearly free of noise at both the W as well as well as the Ir $L_{2,3}$ edges although the signals are quite small (see the enlargement factors for W ($\times$50) and Ir ($\times$20)). Therefore, an induced moment can also be

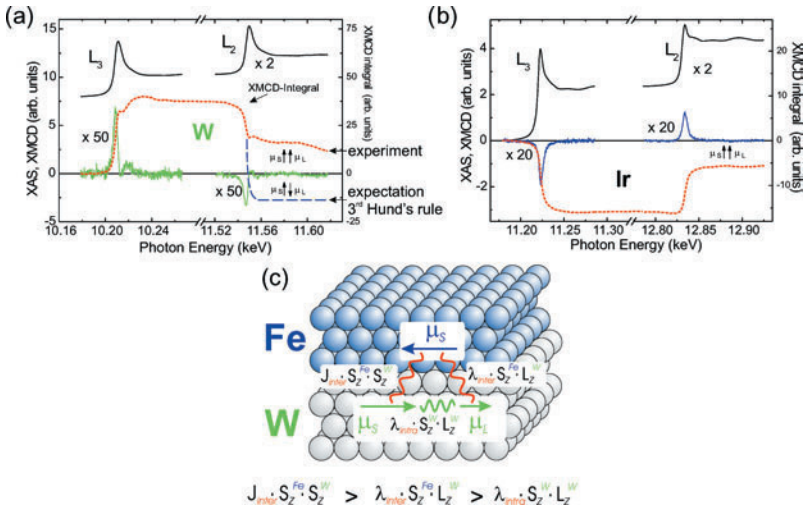

Figure 24. Normalized XAS and XMCD spectra at the $L_{2,3}$ edges of (*a*) W in Fe–W and (*b*) Ir in Fe–Ir multilayers (10 K, 5 T) [206]. For a clearer illustration the XMCD spectra have been scaled (W: ×50, Ir: ×20) and the XAS spectra have been shifted vertically. The XMCD integrals allow for the analysis of the relative orientation of the induced spin moment μ_S to the induced orbital moment μ_L (· · · · ·: experiment, - - - -: hypothetical). (*c*) Schematic representation of the relative orientation of μ_S and μ_L (element specific) for the Fe–W layers and the important interactions in an atomic model [200].

identified for these two 5d elements. The sum rule analysis shows that the induced moments are about $0.2\mu_B$ which is in good agreement with recent calculations [256]. Furthermore, a pronounced fine structure can be observed in the W XMCD which is of similar origin as the asymmetry of the V XMCD as will be discussed in section 5.2. Interestingly, the W L_3 edge XMCD signal is positive whereas the one for Ir is negative as it is also the case for Pt discussed above. This demonstrates that the induced moment in W is aligned antiparallel to the Fe layer as schematically presented in figure 24(*c*) and the induced moment in Ir is aligned parallel to the Fe moment. This parallel or antiparallel orientation of the induced moments versus the atomic number represents a general trend in the transition metal series described by the Bethe–Slater curve: the exchange interaction J depends on the ratio of the interatomic distance for the interacting electrons. The Bethe–Slater curve describes the change of sign of J versus the atomic separation normalized to the d-electron radius. Since the ratio of the interatomic distance and the d-electron radius decreases toward the lighter d elements, a negative J (antiferromagnetic coupling) is found for less than half-filled bands, whereas a positive J (ferromagnetic coupling) is determined for more than half-filled bands. Although this argument is based on a localized picture, the experimental results for the relative orientation of the Fe and the induced 5d spin moments confirm this simple picture. Since metallic layers are investigated here, one can discuss the orientation of induced moment also in an itinerant framework as shown, e.g. in [210]. Therefore, the Fe/5d hybridization has to be taken into account: since the minority W 5d bands are energetically close to the minority Fe 3d bands, a strong hybridization is found. This results in a shift of the W d bands towards smaller energies. However, the majority Fe and W d bands are separated in energy and therefore less hybridization is found for those bands. Hence, the shifted minority W d bands will be more filled, which results in a net spin moment in W which is aligned antiparallel to the Fe moment. Furthermore, the XMCD technique provides information on the induced orbital moment μ_L and its relative orientation to the induced spin moment μ_S. This relative orientation can

be directly determined from the integrated XMCD signal (see also section 2). If the XMCD integral crosses the zero line an antiparallel orientation of μ_S and μ_L is found, whereas parallel orientation is determined if the XMCD integral does not change the sign. Both for the W as well as the Ir case, the XMCD integrals (dotted curves in figures 24(*a*) and (*b*)) do not cross the zero line. Hence, a parallel orientation of the induced spin and orbital moments can be concluded for W and Ir. These results can be compared to the expectations from the third Hund's rule in an atomic picture. In general, Hund's rules are only applicable for purely atomic systems. However, interestingly, the third Hund's rule holds for various solids. This is not the case for the induced magnetism in uranium metal where a breakdown of the third Hund's rule is predicted theoretically [257]. A similar breakdown is determined here for the case of W: in an atomic picture the W 5d shell is less than half-filled. Therefore, an antiparallel orientation of μ_S and μ_L would be expected from the third Hund's rule and hence the XMCD integral should change sign as indicated by the dashed line in figure 24(*a*). However, experimentally a parallel orientation is found which is supported by recent calculations [208,210,256,258–260]. The experimental results are schematically presented in figure 24(*c*): the induced spin moment μ_S^{W} in W is aligned antiparallel to the Fe μ_S^{Fe}. The induced orbital moment μ_L^{W} is oriented parallel to μ_S^{W} and hence is aligned antiparallel to the spin moment of Fe. In a simple atomic picture these moments show the following interactions: (1) the direct *interatomic* exchange between the Fe and W spins: $J_{\mathrm{inter}} S_z^{\mathrm{Fe}} S_z^{\mathrm{W}}$, (2) the *intraatomic* spin–orbit interaction within W: $\lambda_{\mathrm{intra}} S_z^{\mathrm{W}} L_z^{\mathrm{W}}$ and (3) the *interatomic* spin–orbit interaction between the Fe spin and the W orbital moment: $\lambda_{\mathrm{inter}} S_z^{\mathrm{Fe}} L_z^{\mathrm{W}}$. The dominating interaction (1) leads to the antiparallel orientation of the tungsten and iron spins. The *intraatomic* spin–orbit interaction would favour an antiparallel orientation of S_z^{W} and L_z^{W} according to the third Hund's rule. Since experimentally a parallel alignment is determined, the *interatomic* interaction (3) must be larger than interaction (2) as depicted in figure 24(*c*). More advanced theoretical investigations for the layered Fe–W system which go beyond this simple atomic picture are recently given, e.g. by Qian and Hübner [256] and Tyer *et al* [208, 210]. In these theoretical works the influence of a large crystal field splitting in W (Hübner and co-workers) and hybridization between Fe and W taking into account the band-filling and geometrical effects (Tyer and co-workers) were studied. Our new experimental results for layered structures can be compared to earlier experimental works on Fe/5d alloys: surprisingly, an antiparallel orientation of the induced spin and orbital moments μ_S and μ_L for both W as well as Ir is determined for alloys [76] whereas a parallel orientation is found for the layered structures as indicated in the lower part of figure 25. The larger arrows in this figure indicate the orientation of the induced spin moment and the smaller arrows represent the alignment of the induced orbital moment with respect to the Fe spin moment ($\uparrow$: parallel to μ_S^{Fe}, $\downarrow$: antiparallel to μ_S^{Fe}). This indicates that the induced magnetism in alloys is different from the one in layered structures. Our first experimental investigation [206, 209] of layered materials stimulated theoretical works in which the induced magnetism along the 5d series at the interface to Fe was studied in detail for these structures [208, 210]. These results indeed reproduce our experimental findings for layers: for Fe–W and Fe–Ir multilayers the induced spin and orbital moments μ_S^{5d} and μ_L^{5d} couple parallel (Fe–W: $\downarrow\downarrow$, Fe–Ir: $\uparrow\uparrow$), whereas antiparallel orientations are determined for alloys (Fe–W: $\downarrow\uparrow$, Fe–Ir: $\uparrow\downarrow$) in experiment [76] and theory [261,262]. These results can be understood in the following way: in figure 26(*a*) the atomic Hund's rule values for the spin moments and the orbital moments across the transition metal d series are presented. According to the third Hund's the spin and orbital moments are aligned antiparallel (parallel) for less (more) than half-filled shells. The form of the curves for the spin moment and the orbital moment versus the d-count (figure 26(*a*)) [210] can be compared to the ones calculated for 5d impurities in Fe (figure 26(*b*)) [261]. The S-like curve determined for the 5d impurities stems from the hybridization effects discussed above,

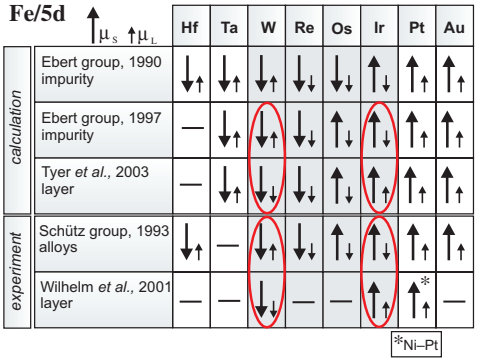

Figure 25. Schematic representation of the relative orientation of the induced spin moment μ_S to the induced orbital moment μ_L for the 5d series determined experimentally for alloys and layered structures (lower part). The experimental results can be compared to *ab initio* calculations for the corresponding structures (impurities, layers) in the upper part [200]. The references are: Ebert group, 1990, impurity [261]; Ebert group, 1997, impurity [262]; Tyer *et al*, 2003, layer [208, 210]; Schütz group, 1993, alloys [76]; Wilhelm *et al*, 2001, layer [206].

leading to negative spin moments at the beginning of the series and positive ones at the end. Interestingly, the orbital moment of the 5d impurities in Fe exhibits two nodes along the 5d series. As demonstrated by Ebert *et al* [261] the shape of this curve can be related to the 'magnetic' density of states, i.e. the difference $n^+(E_F) - n^-(E_F)$ of the local spin-dependent d density of states at the Fermi level. The specific shape of the orbital moment along the d series has the consequence that in the regime between the two nodes (orbital moment negative), the expectation for the relative orientation of the spin moment to the orbital moments according to the third Hund's rule is not fulfilled any more (marked in figure 26(*b*) and darker background in figure 25). This appears as a breakdown of this rule if one stays in an atomic framework. However, for the very beginning and the end of the 5d series the expectancy is met according to this rule. Therefore, an antiparallel orientation of μ_S^{5d} and μ_L^{5d} is found for the light 5d elements Hf and Ta, and a parallel orientation is determined for the heavy elements Pt and Au (lighter background in figure 25). This behavior is similarly discussed for the 3d series in [263] where the change in the relative alignment of μ_S and μ_L across the series is related to the 'remnant' of Hund's rule. Remarkably, the recent calculations for the induced moments in 5d layered structures reveal that the overall shapes of the induced spin and orbital moment curves along the series stay the same as for the 5d impurities [210], however, the curves shift toward the lighter 5d elements for the layers [208, 209]. Therefore, the third Hund's rule appears to break down according to the calculations for the elements W, Re and Os for the layers whereas the expectations according this rule are not fulfilled for the elements Re, Os and Ir in the case of impurities. Thus, the differences between the layered structures and the impurities are especially pronounced in the vicinity of the nodes of μ_L^{5d} along the d series, which are exactly located at the elements investigated here, namely W and Ir. These results demonstrate in which way the interplay of experiment and theory provides new important insight into the induced magnetism in 5d metals on a fundamental level. In a similar manner the induced magnetism in 3d metals will be examined systematically in the next section.

5.2. Induced moments in light 3d transition metals

In this section the induced magnetism in the light 3d elements at the interface to Fe will be discussed in detail. For this investigation trilayers were studied as schematically presented

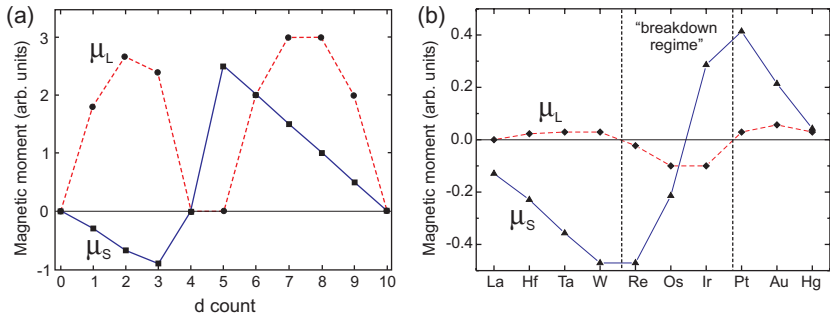

Figure 26. (*a*) Schematic atomic Hund's rule values for spin moments (——) and orbital magnetic moments (- - - -) across the transition metal d series (adapted from [210]). (*b*) Schematic representation of magnetic spin moments (——) and orbital moments (- - - -) of 5d transition metal impurities in Fe (adapted from [261]).

in figure 19. These trilayers are the smallest prototype of a magnetic multilayer where the ferromagnetic films (Fe) are separated by layers consisting of light 3d elements. The *in situ* preparation of these trilayers allows for a control of the growth *in statu nascendi*. We developed a preparation recipe that provides sharp interfaces by minimizing the intermixing due to atomic exchange processes [203]: first a bulk-like thick Fe buffer (∼100 Å) is evaporated on a Cu(100) single crystal [201]. This Fe film exhibits a bcc(110) structure [264–267]. To flatten the buffer the Fe film was softly annealed to 450 K. Then the sample was cooled back to room temperature before the light 3d element was deposited on the buffer. This growth recipe was established experimentally by scanning tunnelling microscopy [203] and theoretically by means of molecular dynamics calculations which demonstrate that this procedure reduces the atomic interface exchange processes [268]. To study the induced magnetism in the light 3d transition metals (TM) systematically the XMCD at the $L_{2,3}$ edges of the light TM was investigated. Similar to the case of the induced moments in 5d metals the induced moments in the light 3d elements are quite small. In order to achieve the XMCD data with the necessary statistics the measurements were carried out at the UE56/1-PGM undulator beamline [269] of the BESSY II synchrotron radiation facility using the gap-scan technique (see section 3). The experimental results are given in figure 27 together with the spectra for the heavy 3d ferromagnets Fe, Co and Ni. The metals Ti and V are nonmagnetic in their bulk whereas Cr is an antiferromagnet. Hence, the XMCD signals presented in figure 27 originate from induced moments in the cases of Ti and V, whereas uncompensated spins are probed for the 3 ML of Cr. For a clearer representation of the systematics the sign of the XMCD spectra of Ti, V and Cr was changed, as indicated by the negative enlargement factors. In the original data the main L_3 signals for Ti, V and Cr are negative, while the one for Fe is positive. Therefore, the induced moments in the light 3d layers are aligned antiparallel to Fe (figure 28). The same band-filling arguments for the orientation of the induced moment in the 5d metal W (section 5.1) also hold for the Ti and V cases presented here: the V minority d-band hybridizes with the majority d-band of Fe. Thereby, the V minority band is pulled down in energy [270] as schematically presented in figure 29. This results in an induced magnetic moment in V which is aligned antiparallel to the Fe moment.

While traversing the 3d series from the heavier elements toward the lighter ones systematic changes of the isotropic and the dichroic spectra can be identified: (i) the separation of the $L_{2,3}$ edges decreases. They are separated by about 17 eV for Ni which reduces to about 6 eV in the case of Ti. (ii) There is a clear transfer of spectral weight in the isotropic spectra from the L_3 to the L_2 edge. (iii) For the ferromagnets Fe, Co and Ni the XMCD signal of

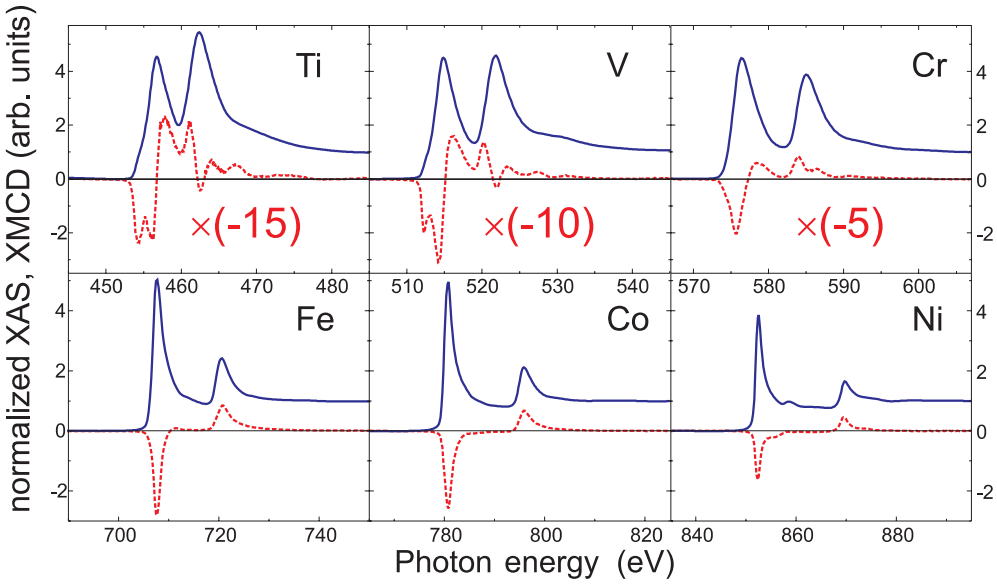

Figure 27. Normalized isotropic spectra (——) and corresponding XMCD spectra (- - - -) for the light 3d transition metals in the upper panel in comparison to the heavy 3d ferromagnetic transition metals Fe, Co and Ni in the lower panel [204] at the $L_{2,3}$ edges. The XMCD spectra for the light 3d transition metals (TM) are obtained for Fe–TM–Fe(110) trilayers, whereas the Fe, Co and Ni spectra are recorded for bulk-like films on Cu(100). The direction of the magnetization for the light 3d metals is defined with respect to the one of Fe in the trilayer. For a clearer presentation of the systematics, the sign of the Ti, V and Cr XMCD spectra was changed (please note the negative enlargement factors).

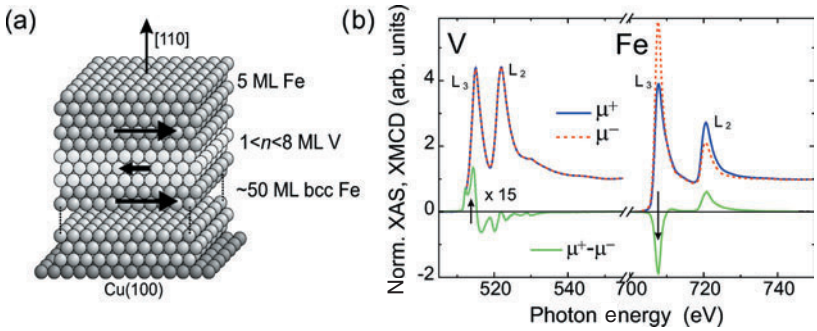

Figure 28. (*a*) Schematic representation of a prototype Fe–V–Fe(110) trilayer on a Cu(100) substrate. The bold arrows indicate the direction of the total Fe and V moments, respectively. The element specificity of the x-ray absorption technique allows for the disentanglement of the magnetism of the individual layers: (*b*) normalized XAS for right (μ^+) and left (μ^-) circularly polarized x-rays (top) and the corresponding XMCD at the V and Fe $L_{2,3}$ edges of a Fe–V_4–Fe trilayer [200, 202]. For a clearer representation, the V XMCD was multiplied by a factor 15. The positive XMCD signal at the V L_3 edge in contrast to the negative one at the Fe L_3 edge (see arrows) reveals that the induced moment in V is aligned antiparallel to the one of Fe.

each edge is basically symmetric, whereas already for the case of Cr an asymmetry of the L_3 edge XMCD can be determined. This asymmetry becomes more pronounced for V and Ti and a double peak structure appears at the L_3 edge. The explanations for these changes are: (i) the spin–orbit splitting of the core states reduces. This indicates a strong overlap of

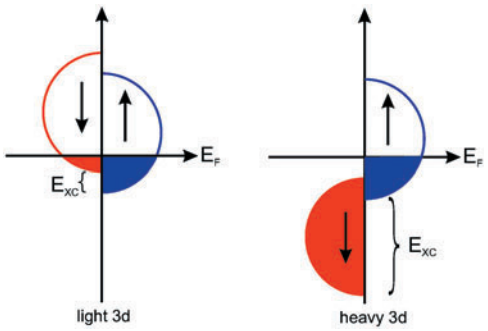

Figure 29. Schematic representation of the 3d spin-dependent density of states (DOS) for the heavy 3d elements (Fe, Co and Ni) in comparison to the DOS of the light 3d elements (Ti, V) at the interface to a 3d ferromagnet. The splitting of the light 3d bands is due to hybridization at the interface with the bands of the heavy 3d ferromagnet.

the $L_{2,3}$ contributions for Ti. This complicates the application of the spin sum rule, where these two contributions must be disentangled. (ii) The spin–orbit splitting in the initial states decreases until it is in the same range as the core hole correlation energies. This results in a mixing of the initial states which was analysed in various experimental and theoretical works [73, 109, 112, 113, 271]. As will be discussed later, these core hole effects are also responsible for the failure of the spin sum rule for the light 3d elements. (iii) For Fe, Co and Ni the majority spin-band is almost or completely filled because of the large exchange splitting of the spin-dependent bands, whereas the Ti and V bands are less than half-filled and present only a small exchange splitting as schematically presented in figure 29. Since the majority band is mostly filled for the heavy 3d elements the difference of the absorption coefficients for right and left circularly polarized x-rays is basically symmetric. This is because the XMCD signal is related to the difference of the spin-dependent empty density of states. Consequently, the XMCD difference becomes asymmetric for the light 3d elements, which is also the reason for the small asymmetry in the W XMCD (figure 24). However, this simplified picture neglects the effective exchange field splittings of the initial 2p and final 3d sublevels which are necessary for a more accurate description of the XMCD signal as discussed, e.g. in [53, 74, 272]. Unfortunately, a comprehensive theory for the dichroic spectra that includes these core hole correlation effects for metals is still missing. Therefore, we established a simple double-pole approximation within the framework of the TDDFT [73]. This double-pole model describes correctly the spectral shape of the isotropic XAS and consequently the dependence of the spectral $L_{2,3}$ intensity ratio (branching ratio) on the atomic number of the element analysed. Since the atomic number is correlated with the number of d-holes N_h and the spin–orbit splitting of the initial $2p_{1/2}$ and $2p_{3/2}$ states, the double-pole approximation allows us to relate the failure of the sum rules with these properties. As a result, the correlation energies can be given [73] following the procedure presented in [115]. These results can be applied to test various theoretical approximations for the exchange correlation functional f_{xc}. Together with the XMCD spectra of high quality (signal-to-noise ratio about 180) presented in figure 27 they can be used as references.

The induced magnetism will now be discussed using the Fe–V–Fe system as an example (see figure 28). There are various open questions in the literature that will be addressed here: conflicting results exist concerning the range of the polarization in V. Earlier experimental works for Fe–V multilayers determined a long-range polarization, i.e. a sizable induced moment in V was found for layers 4 ML away from the interface to Fe. This phenomenon was

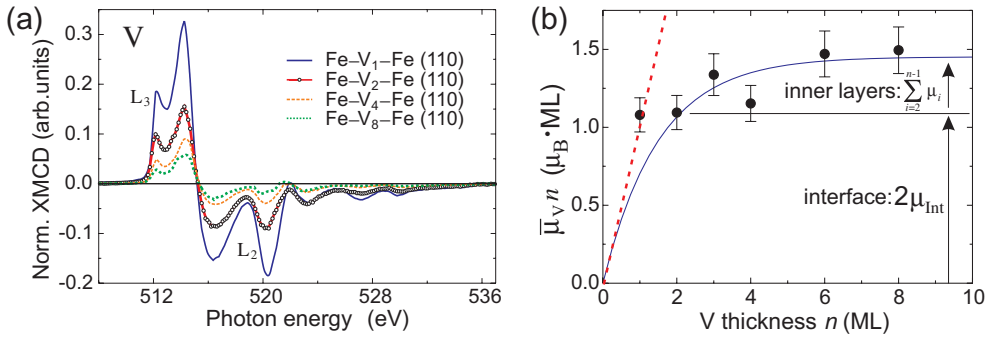

Figure 30. (*a*) Thickness dependence of the V $L_{2,3}$ XMCD for Fe–V_n–Fe(110) trilayers with $n = 1, 2, 4$ and 8 ML. (*b*) Average total V moment $\bar{\mu}_V$ times the V thickness n as a function of n. This product $\bar{\mu}_V n$ saturates above $n = 3$ ML, indicating a short-range polarization [200, 202].

attributed to a 'transient ferromagnetic state' of vanadium [194, 195]. In contrast, theoretical works revealed only a short-range polarization [188, 192]. Connected with this conflict is the question about the size of the induced spin and orbital moments at the interface to Fe. To solve these questions a thickness-dependent XMCD study was carried out for various trilayers. The V thickness was varied in the range of 1–8 ML. For these thicknesses the Fe films couple ferromagnetically by the interlayer exchange coupling and the temperature dependence of this coupling is studied in [273]. The experimental results are given in figure 30. The edge jumps of the isotropic spectra, that correspond to the XMCD spectra presented in figure 30(*a*), are normalized to unity as it is done for the spectra for the Fe–V_4–Fe trilayer in figure 28(*b*). Therefore, the XMCD intensities are a direct measure of the average V moment $\bar{\mu}_V$ per atom in the entire layer. If all the layers exhibit the same moment then the XMCD intensities would be equal for all the trilayers probed. This is obviously not the case as it can be seen from the decrease of the XMCD signals for larger V thicknesses shown in figure 30(*a*). This demonstrates that $\bar{\mu}_V$ strongly decreases for the samples with thicker V layers. Hence, similar to the magnetic moment profile given in figure 22 of section 5.1 the largest induced moment is found directly at the interface to the ferromagnet and a decrease of this induced moment is determined for the inner layers. Furthermore, the XMCD line shape is basically the same for all the trilayers since the XMCD signals can be scaled on to each other. This allows for a quantitative analysis of the range of the polarization without applying the sum rule analysis. When the XMCD spectra in figure 30(*a*) for the Fe–V_2–Fe system are compared with the Fe–V_4–Fe one, a decrease of the XMCD intensity by about a factor of two is determined for the thicker V layer. This demonstrates that the two additional layers hardly show an induced moment. Similarly, a reduction by a factor of two is found when the intensities for the trilayer with a vanadium thickness of 4 ML are compared to the 8 ML system. This is already a strong indication that the induced moment is basically located directly at the interface to Fe. The large signal for one layer of V is because it is in contact with the polarizing Fe layers from both sides. For a more detailed analysis, the product of the number of layers n with the average moment $\bar{\mu}_V$ is plotted versus the number of layers in figure 30(*b*). It will be discussed later how the absolute moments can be given for $n\bar{\mu}_V$. Here, it is sufficient to discuss the relative changes of $n\bar{\mu}_V$ which can be calculated from the number of layers times the integral XMCD intensity at the L_3 edge. If all V layers carry the same moment a straight line would be expected as indicated by the dashed line in figure 30(*b*). However, experimentally, a quickly saturated curve is found, as shown by the solid line. Saturation is reached already for about three atomic layers, which shows that the dominant signal originates from the two interface layers and only

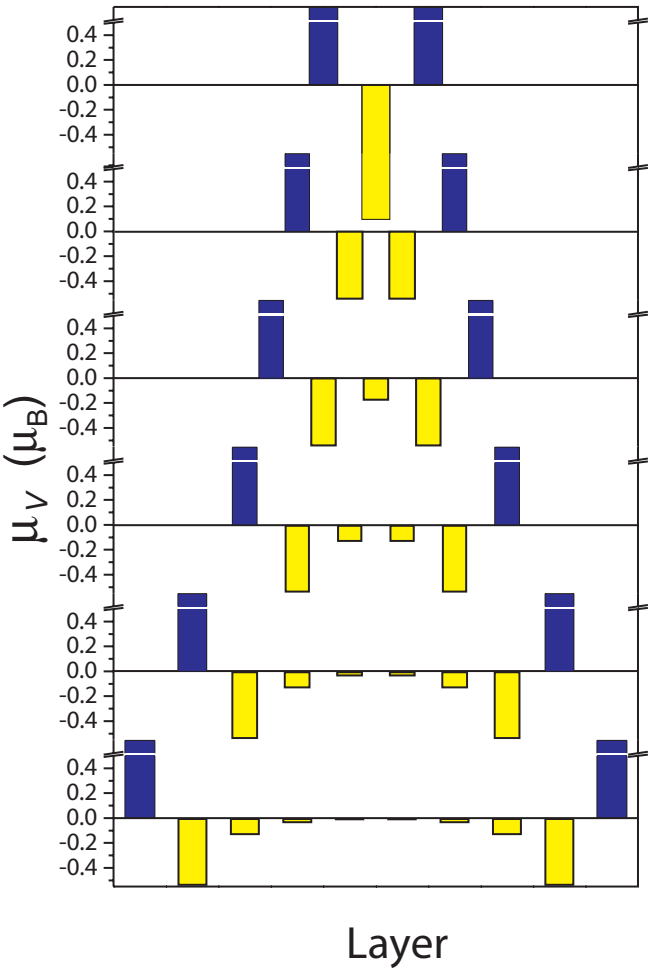

Figure 31. (*a*) Vanadium total magnetic moment profile (light bars) determined from the thickness-dependent study of the prototype Fe–V_n–Fe(110) trilayers with $n = 1, 2, 3, 4, 6, 8$. The errors of the V moments are ±15%. The dark bars represent the Fe moment in schematic form to visualize the antiparallel orientation of the Fe moment to the induced V moment [200].

a minor contribution is due to the inner layers (see arrows in figure 30(*b*)):

$$\bar{\mu}_{\mathrm{V}} n = 2\mu_{\mathrm{Int}} + \sum_{i=2}^{n-1} \mu_i . \tag{15}$$

Hence, a short-range polarization can be concluded from these experiments in accordance with theoretical predictions [188, 192]. A magnetic moment profile is determined under the same assumptions made in section 5.1 for the construction of the Ni–Pt profile. It is assumed that the induced moment only depends on the distance of the V layer from the (sharp) interface. With this model, the solid line in figure 30(*b*) is fitted. From this fit the profile presented in figure 31 can be determined. The layer-resolved V moments are given by the lighter bars. A profile for the Fe layers could not be determined because a bulk-like Fe buffer was used to polarize the V layers. If thinner Fe layers on the Cu(100) substrate were used, these films would be structurally and magnetically different (face-centred tetragonal (fct) structure) compared

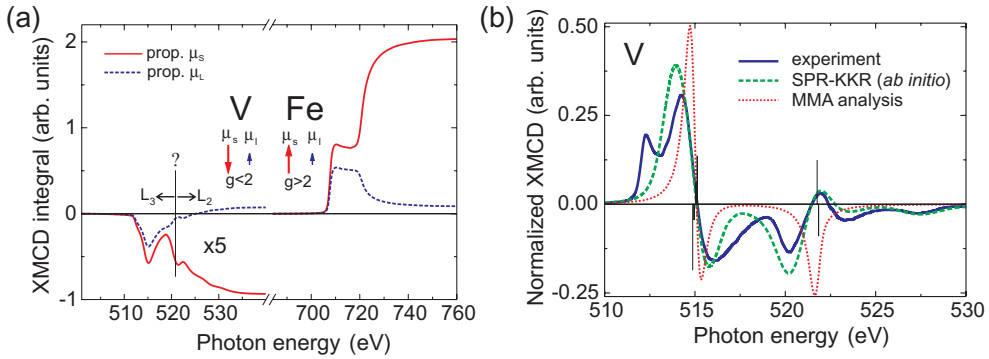

Figure 32. (*a*) Experimental XMCD integrals at the V and Fe $L_{2,3}$ edges for a $Fe_{0.9}V_{0.1}$ alloy [200] which are used for the standard XMCD sum rule analysis. (*b*) Result of the multiple-moment analysis (MMA) (· · · · · ·) of the experimental XMCD data (——) for the $Fe_{0.9}V_{0.1}$ alloy. The MMA results are compared to *ab initio* calculations (- - - -) [201].

to the Fe(110) structure of the thick buffer. To indicate the antiparallel alignment of the induced V moments, the positive dark bars represent the Fe moments. The Fe moments are reduced at the interface, compared to the bulk Fe moments as it was determined in various works for multilayers [199, 274–276] and for Fe films on a V single crystal [277]. The V moment profile shown in figure 31 clearly reveals that the induced moment is basically located at the interface, which demonstrates the short-range character of the polarization. This solves the inconsistencies between earlier theoretical and experimental works by supporting the theoretical results. The long-range polarization determined in the earlier experimental works for multilayered structures [194, 195] might be due to stronger interdiffusion at the interface because of the higher deposition temperature (570 K) used for the preparation of the multilayers. This highlights the need for a controllable growth procedure which was applied here, where the deposition temperature was 300 K only. To verify the effect of the deposition temperature on the range and the size of the polarization we also evaporated the V film at an elevated temperature (600 K) on the Fe buffer [203]. Indeed, an *apparent* long-range polarization could be falsely determined for these trilayers. In fact, this long-range polarization is only ostensible because sharp interfaces are assumed in the analysis although alloying is found at the interface at elevated temperature [203, 276, 278, 279].

Now, it will be discussed in which way absolute magnetic moments can be given for the V layers. It emerges that the standard analysis either by using the sum rules in their integral form or by fitting the spectral shape of the XMCD spectra with the multiple-moment analysis (MMA) [280] fails. To test this, a $Fe_{0.9}V_{0.1}$ alloy was investigated as a reference sample (for details of the sample preparation see [201]). The induced moment in V for this alloy is known from a polarized neutron study (PNS) [281]. Our experimental spectra for this alloy are given in figure 32(*b*). First, the applicability of the integral sum rule analysis is to be tested. The corresponding integrals which should be proportional to μ_S and μ_L are presented in figure 32(*a*) for V as well as for Fe. For Fe the integral which is proportional to μ_L (dotted line) does not cross the zero line. Thus, a parallel alignment of μ_L^{Fe} and μ_S^{Fe} can be concluded which results in $g^{\mathrm{Fe}} > 2$ (see equation (12)). To determine the spin moment, the contributions of the $L_{2,3}$ edges have to be separated. This procedure is straight forward for the case of Fe and leads to the integral presented by the solid line in figure 32(*a*). From this integral sum rule analysis the Fe moments given in table 2 are calculated. The XMCD results for Fe are in fair agreement with the ones of the PNS. However, this is not the case for the V moments. Due

Table 2. Spin and orbital moments of V and Fe for the $Fe_{0.9}V_{0.1}$ alloy calculated by theory and apparently obtained by XMCD by the sum rules [201]. The total magnetic moments are presented together with the ones obtained by PNS [281]. The V XMCD values (brackets) strongly deviate from theory and PNS, and cannot be taken as final results (see text). The errors for the Fe moments as determined from the XMCD results are ±10%.

$Fe_{0.9}V_{0.1}$	V			Fe		
(μ_B/atom)	XMCD	PNS	Theory	XMCD	PNS	Theory
μ_S^{3d}	(−0.20)	—	−1.01	2.09	—	2.22
μ_L^{3d}	(0.016)	—	0.020	0.093	—	0.053
μ_{tot}^{3d}	(−0.18)	−1.07	−0.99	2.18	2.23	2.27

to the reduced spin–orbit splitting of the initial $2p_{1/2}$ and $2p_{3/2}$ states, the separation of the $L_{2,3}$ edges is smaller for V in comparison to Fe (see figure 27). Therefore, a much stronger overlap of the XMCD contributions from the L_3 and L_2 edge is observed. The analysis of the relative orientation of μ_L^V and μ_S^V is still valid because the contributions of the V $L_{2,3}$ edges do not have to be separated. The integral being proportional to μ_L^V clearly crosses the zero line as shown in figure 32(a). Consequently, an antiparallel orientation of the induced μ_S^V and μ_L^V can be determined and $g^V < 2$. This is the reason for the larger g-factor for the entire sample determined by FMR measurements for Fe–V multilayers [197,198,282] in comparison to the element specific XMCD results [199]. The orbital moment μ_L^V for V is aligned parallel to the Fe orbital moment as depicted in figure 19. This is because (i) the induced spin moment μ_S^V in V is aligned antiparallel to the Fe spin moment μ_S^{Fe} and (ii) $g^V < 2$ is determined for V whereas $g^{Fe} > 2$ is found for Fe. Therefore, the Fe and V orbital moments add up, whereas the spin moments cancel each other. Hence, the effective g-factor g_{eff} [198] determined from FMR measurements is larger.

The strong overlap of the $L_{2,3}$ edges for V, hinders the quantitative analysis of the spin moment using the sum rules because these contributions must be separated. This ambiguity becomes obvious when investigating the solid line for V in figure 32(a). The uncertainty where to set the border between the L_3 and the L_2 edge contribution, leads to errors in the application of the spin sum rule. Furthermore, the smaller spin–orbit splitting in the initial states for V in comparison to Fe is in the range of the core hole interaction. Therefore, the initial $2p_{1/2}$ and $2p_{3/2}$ states mix and the quantum numbers j, m_j cannot be used to characterize the states. This is the origin of the shift of the spectral weight from the L_3 to the L_2 edge in the isotropic data as can be seen for the lighter 3d elements in figure 27. The result is the deviation of the branching ratio from its statistical value for the light 3d elements [73, 109, 112, 113, 271]. Consequently, the single-particle approximation used for the derivation of the magneto-optical sum rules breaks down leading to a failure, especially, of the spin sum rule. However, for the orbital sum rule the entire XMCD spectrum is integrated and therefore the determination of the orbital moment is expected to be less affected by the core hole effects, as discussed in theoretical works [283, 284]. The dramatic effect of the core hole interaction becomes obvious when inspecting the values of the sum rule analysis from the integrals shown in figure 32(a) which are listed in table 2. It turns out that the spin moment μ_S^V determined from the sum rule analysis differs by about 80% with respect to the PNS, whereas the orbital sum rule seems to be less influenced. Interestingly, despite these difficulties one can find applications of the sum rule analysis to determine the V moments in the literature, e.g. for XRMS experiments [285]. Another drawback of the integral sum rule analysis is the neglect of the detailed fine structure in the V XMCD spectra. Therefore, one might argue that a fitting procedure could be more reliable if the spectral shape of the spectra is fitted. The MMA is

such a fitting procedure (for details see [280]). This type of analysis is also derived from an independent-particle model and is therefore likely to fail for the light 3d elements if the core hole interaction is not taken into account [280, 286]. Surprisingly, this procedure was used for the analysis of Cr and V moments in recent works [287–289]. Therefore, we tested the multiple-moment analysis for our experimental results in the following way: usually, the experimental data are fitted by applying the MMA procedure with numerous free parameters (spin moment, orbital moment, number of d holes, effective exchange field, lifetime broadening at the L_3 and L_2 edges). Here, we employed a different approach by using the results of an *ab initio* calculation [201] for the MMA procedure. Therefore, two theoretical approaches are compared. The *ab initio* calculation which makes use of a fully relativistic SPR-KKR Green's function method will be discussed in detail later. In figure 32(*b*) the experimental XMCD data (solid line) are shown together with this *ab initio* calculation [201] (dashed line). It turns out that the SPR-KKR calculation reproduces all the fine structures of the experimental XMCD spectra. Hence, it is reasonable to simulate the spectra with the MMA approach by taking the values from the SPR-KKR calculation for the properties that enter into the MMA [73, 201]. The result is presented in figure 32(*b*) (dotted line). Interestingly, the general trend for the asymmetry of the XMCD signal at the L_3 edge can be modelled with the MMA procedure. However, the MMA analysis yields a symmetric contribution at the L_2 edge whereas in the experiment and in the *ab initio* calculation a clear asymmetry can be detected. Furthermore, the L_2 contribution in the MMA analysis is located at a photon energy which is about 2 eV too large with respect to the experimental result. This demonstrates that the SPR-KKR calculation accurately takes band structure effects into account which cannot be modelled within the atomic framework of the MMA analysis. Therefore, the two standard procedures (sum rule and MMA analysis) fail to determine magnetic moments from the XMCD spectra for V. To overcome this difficulty the magnetic ground state properties are determined by the help of the *ab initio* calculation (for details of the SPR-KKR method see [53,104,105,201]). The advantage of these calculations is that both the magnetic ground state properties *and* the corresponding isotropic and dichroic absorption spectra are calculated. Therefore, the detailed information in the fine structure of the absorption spectra can be compared for theory and experiment which is not the case when applying the integral sum rule analysis where this information is neglected. The result of the *ab initio* calculation is presented together with the experiment in figure 33(*a*) for V. The corresponding calculated spin-resolved unoccupied d density of states (DOS) are shown in figure 33(*b*). Interestingly, the spin-up and spin-down DOS do not exhibit pronounced fine structures, only the difference of the two does. Hence, the connection of the spectral shape of the XMCD spectra with this difference makes the XMCD technique a versatile tool to detect even small fine structures in the DOS itself. Since core hole correlation effects are not included in the calculation the deviation of the branching ratio from its statistical value as seen in the isotropic experimental data (top) cannot be reproduced by the theory. However, even in the isotropic data a broad satellite structure labelled A is also detected in the calculation (see inset of figure 33(*a*). Since this structure is located at 532 eV in the vicinity of the oxygen K edge it could have been falsely related to an oxygen contamination in the experiment. Fortunately, the SPR-KKR calculation reveals that this fine structure originates from fine structures in the V band structure, namely a van Hove singularity at the N point of the bcc Brillouin zone [201]. Turning to the dichroic spectra it becomes obvious that basically all the detailed fine structures are described by the theory. The asymmetric contributions at the L_3 edge (labelled B) and the L_2 edge (labelled C) match the experiment. Even the small oscillatory fine structures marked with D at photon energies larger than the L_2 absorption edge follow the spectral distribution in the experiment. Only the feature labelled E in the pre-edge regime is not reproduced by the theory which reveals that it might stem from a multiplet structure. The good agreement

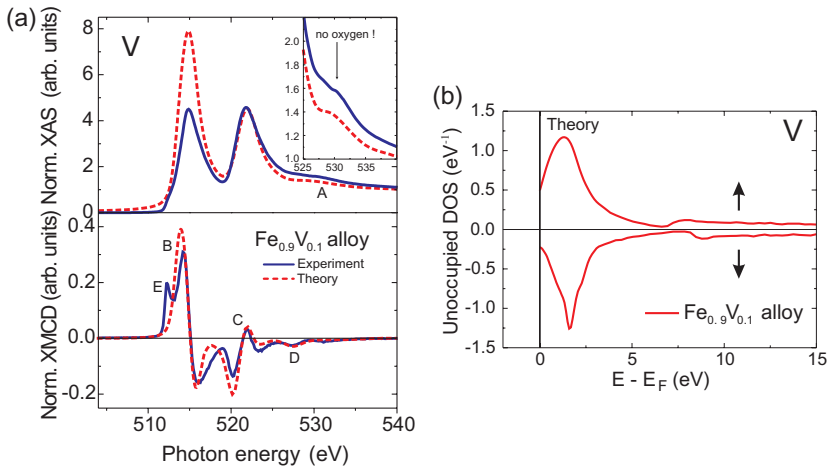

Figure 33. (*a*) Comparison of the experimental XAS and the corresponding XMCD at the V $L_{2,3}$ edges of a $Fe_{0.9}V_{0.1}$ alloy (——) to *ab initio* calculations (- - - -) [200, 201]. (*b*) Spin-dependent density of unoccupied d states of V for the $Fe_{0.9}V_{0.1}$ alloy. The zero energy corresponds to the Fermi level.

between theory and experiment allows for the adoption of the spin and orbital moments from the fully relativistic calculation to the experiment. The theoretical results given in table 2 have been corrected for the magnetic dipole term T_z (for details see [201]) which enters into the determination of the spin moment as described in section 2. The comparison of μ_S and μ_L for Fe as determined from the experiment (XMCD sum rule analysis) and the theory demonstrates that the calculation is in good agreement with the experiment for the heavier 3d element Fe. In contrast, the deviation of these values for V from the XMCD spectra with respect to the theory highlights the breakdown of the spin sum rule for the lighter 3d element V as discussed above. If one compares the experimental XMCD spectra of the $Fe_{0.9}V_{0.1}$ alloy (figure 33(*a*)) to the ones of the layered structures (figure 30) it turns out that the XMCD spectra exhibit the same fine structure and can therefore be scaled onto each other. This fact and the agreement of the SPR-KKR calculation for the $Fe_{0.9}V_{0.1}$ alloy with the experimental spectra establishes this alloy as an experimental standard for this specific itinerant system[1]. This procedure is justified because in the vicinity of the absorption edge the fine structures of XMCD are similar to the ones calculated in an atomic framework (see, e.g. spectra for V ions in [290]). However, the fine structures in the more extended energy range are related to band-structure effects which cannot be modelled by the atomic calculations. Therefore, the experimental standard is used here. As discussed above, the induced moment in V for the layered structure is basically found at the interface. Hence, the local environment of these V atoms is akin to the one of the alloy which is one reason for the similarity of the V XMCD spectra of the two systems. With the help of this standard the spin and orbital moments can be deduced for the layered structures. With this scaling procedure the absolute V moments can be provided for the trilayer structures and multilayered structures investigated earlier [199]. Examples are given in table 3. The induced spin moment per atom (corrected for T_z [201]) for the trilayer is $\mu_S(\text{trilayer}) = -0.57\mu_B$ which is nearly a factor of two smaller, compared to the multilayer with the same V thickness for which $\mu_S(\text{multilayer}) = -0.93\mu_B$ was found.

[1] However, for more localized systems like oxides a different standard must be used because of different core hole effects.

Table 3. Spin-, orbital- and total-moment for vanadium in the $Fe_{0.9}V_{0.1}$ alloy [201], a Fe–V_2–Fe(110) trilayer [200,202] and a $(Fe_4–V_2)_{60}$ superlattice [199] as deduced by scaling to the reference sample [201].

(μ_B per atom)	Alloy $Fe_{0.9}V_{0.1}$ (exp. standard)	Trilayer Fe–V_2–Fe(110) (scaled)	Multilayer $(Fe_4–V_2)_{60}$ (scaled)
μ_S^{3d}	−1.01(15)	−0.57(8)	−0.93(15)
μ_L^{3d}	0.020(10)	0.025(12)	0.015(7)
μ_{tot}^{3d}	−0.99(15)	−0.54(8)	−0.91(15)

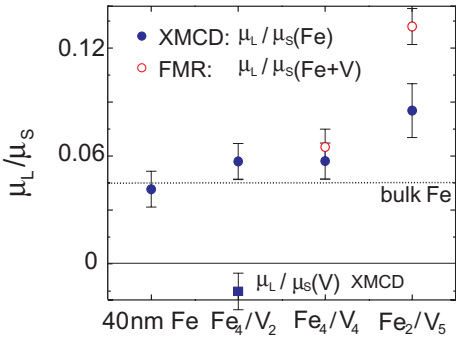

Figure 34. The ratio μ_L^{Fe}/μ_S^{Fe} for Fe (●) in three multilayers and a bulk reference sample [199]. The ratios $\mu_L^{Fe+V}/\mu_S^{Fe+V}$ for the samples (○) are deduced by FMR [197, 282].

This again supports the finding of interdiffusion at the Fe–V interface for the multilayers as aforementioned which is an intrinsic difficulty of the multilayer preparation itself. For the multilayer a total magnetic moment of μ_{tot}(multilayer) = 0.91(15) μ_B is determined from the V XMCD spectra [201]. This value is in good agreement with the one we determined by means of a combined Fe XMCD and VSM investigation on the identical sample [199] which yielded μ_{tot}(multilayer) = 1.06(15)μ_B. This demonstrates that the procedure applied here works reasonably well in order to determine the V moments from the V XMCD by the help of *ab initio* calculations and of an experimental standard. The induced orbital moment is aligned antiparallel to the induced spin moment for all the cases as listed in table 3 and presented by the negative ratio μ_L/μ_S for V in figure 34 for the Fe_4V_2 sample. In relation to the spin moment, the orbital moment is largest for the trilayer and consequently the calculated g-factor for V (see equation (12)) ranges from 1.91 for the trilayer to 1.96 for the alloy and 1.97 for the multilayer. The quantitative results of the element specific investigation of the multilayers by means of the XMCD technique [199, 201] can be compared to FMR investigations of the identical samples [197, 198, 282]. The results are given in figure 34. As discussed above, the FMR technique measures an effective g-factor of the entire sample g_{eff}(Fe + V) which is connected to the averaged ratio $\mu_L^{Fe+V}/\mu_S^{Fe+V}$ [198]. This is because the total magnetization originating from the Fe and V layers precesses when interacting with the microwave field and the static magnetic field in the FMR measurements (see, e.g. [198, 291]). The element specific results presented above reveal that the orbital moments of Fe and V are aligned parallel whereas an antiparallel orientation of the spin moments is obtained. Therefore, a larger ratio $\mu_L^{Fe+V}/\mu_S^{Fe+V}$ is expected to be determined from the non-element-specific technique (FMR) compared to the ratio μ_L^{Fe}/μ_S^{Fe} from the XMCD technique. This is indeed found as shown in figure 34. For

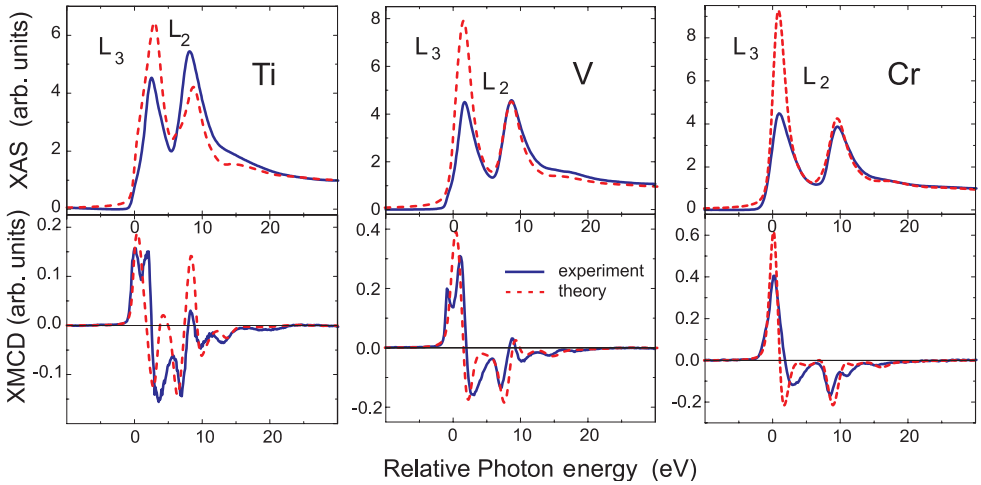

Figure 35. Normalized XAS (above) and XMCD spectra (below) for the light 3d TM's Ti, V and Cr at the $L_{2,3}$ edges: (——) experimental data versus (- - - -) *ab initio* calculations [205]. The experimental data have been corrected corresponding to measurements with 100% circularly polarized light with the k-vector parallel to the magnetization. Note that scaling factors between theory and experiment as well as between the XAS and XMCD intensities do not exist.

the Fe_4–V_4 and Fe_2–V_5 multilayers the FMR results are larger than the ones determined from the XMCD measurements because of the induced moments in V. Furthermore, one can make out an increase of μ_L/μ_S with decreasing Fe thickness from both the FMR and the XMCD investigations. This trend is also supported by recent calculations [278]. The origin of the enhancement of μ_L/μ_S is the unquenching of the orbital moment due to the lowering of the symmetry at the Fe–V interface as has been seen in other experimental works for different samples [247, 292].

Now, we turn back to the systematic investigation of the line shape of the XMCD spectra for the light 3d elements Ti, V and Cr (figure 27). The magnetic moments for the Ti and Cr were determined in the same way as described above for V. The experimental XMCD spectra are compared to *ab initio* calculations which provide the absolute moments and the corresponding fine structure. The results are presented in figure 35. For a clearer representation of the systematics, the experimental and theoretical results for the $Fe_{0.9}V_{0.1}$ alloy are plotted together with the spectra for Fe–Ti–Fe(110) and Fe–Cr–Fe(110) trilayers [205]. A $TiFe_2$ compound was used for the theoretical modelling. It turned out that this is the most reasonable description because the experiments revealed that the Ti XMCD signal is independent of the deposited Ti film thickness up to a thickness of 15 Å. This suggests that a $TiFe_2$ structure is formed as it has been also determined for Fe–Ti multilayers [293]. To model the Cr spectra an $Fe_{0.9}Cr_{0.1}$ alloy was utilized to account for some intermixing at the interfaces [205]. As can be seen in figure 35, basically all the fine structures in the experimental XMCD spectra are reproduced by theory. This good agreement justifies the use of the absolute moments from the calculations to determine the magnetic ground state properties from the experimental results for Ti and V (table 4). For Cr a moment of about $-0.6\mu_B$ is determined from the experiment by scaling to the theoretical spectra. This value is in agreement with the one determined in earlier investigations for trilayers by Idzerda *et al* [294]. For comparison the results of the sum rule application to the experimental data are also given in table 4. For all the cases the spin sum rule yields values which are much too small with respect to the theory. This again demonstrates the breakdown of this sum rule because of the core hole interaction for the light 3d elements, as was discussed

Table 4. Spin and orbital magnetic moments as calculated by *ab initio* theory corresponding to the theoretical XAS and XMCD spectra in figure 35 [205]. The apparent magnetic moments derived by the application of the sum rules to the experimental data are given for comparison. The spin sum rule results clearly underestimate the spin moments revealing the breakdown of this standard analysis procedure.

	Theory		Experiment apparent moments (sum rule)	
	μ_S/μ_B	μ_L/μ_B	μ_S/μ_B	μ_L/μ_B
Ti ($TiFe_2$)	−0.70	0.014	−0.17	0.069
V ($Fe_{0.9}V_{0.1}$)	−1.01	0.020	−0.20	0.016
Cr ($Fe_{0.9}Cr_{0.1}$)	−0.95	0.014	—	—
Cr (Fe–Cr_3–Fe)	—	—	−0.28	0.011

above in detail for V. For Ti and V the spin sum rule results differ by about a factor of 4–5. Interestingly, for the Cr spin moment the sum rule result ($-0.28\mu_B$) deviates by about a factor of 2 with respect to the scaled theoretical value ($-0.6\mu_B$, see above). This shows that the application of the sum rules becomes justified for the heavier elements as it was determined in earlier experimental investigations for Fe and Co [80] and in atomic calculations for Mn, Fe, Co and Ni ions [82]. Despite the drawbacks of the sum rule application the relative orientation of the orbital moment to the spin moment can be correctly determined. In agreement with the theory an antiparallel alignment is found for the three elements as shown in table 4. However, detailed analysis also reveals clear deviations of the theoretical values for the orbital moments with respect to the sum rule results. Hence, the sign of the moments can be determined by the standard analysis with the integral sum rules whereas the quantitative analysis breaks down.

5.3. XMCD of rare earth metals: Tb

In the preceding sections the induced magnetism in 5d and light 3d metals at the interface to ferromagnets was studied. Now, we turn to a different form of induced magnetism, i.e. within the same element: in rare earth metals the localized 4f moments polarize the electrons of the 5d conduction band which causes the ordering of 4f moments. In various studies at the $L_{2,3}$ edges of rare earth compounds the possible appearance of electric quadrupolar transitions (E2: $2p \rightarrow 4f$) in addition to electric dipolar contributions (E1: $2p \rightarrow 5d$) was discussed for XMCD investigations [216–224,295–298], for resonant inelastic x-ray scattering measurements [299,300] and for XRMS studies [301–303]. Hence, one encounters the general possibility to study both the 4f and the 5d magnetism at the $L_{2,3}$ edges. Surprisingly, in other studies no indications for an E2 contribution to the L_2 edge XMCD were found for various rare earth ions [304]. Unfortunately, the earlier investigations have been mostly carried out for rare earth compounds which exhibit a complicated electronic structure because of various many-body interactions. The pioneering XMCD studies by Schütz *et al* [96] have indeed been carried out for single-element rare earth metal foils. However, because of the performance of the synchrotron radiation facilities at that time the detailed fine structures in the XMCD could not be resolved clearly (figure 8(*a*)). A further difficulty in the $L_{2,3}$ edge XMCD analysis is the strong spin dependence and energy dependence of the E1 transition matrix elements. However, the effect of this spin dependence on the applicability of the sum rule analysis has not yet been studied. Therefore, the fundamental questions that will be addressed here are the following: What is the spectral shape of the E1 and E2 contributions in the $L_{2,3}$ edge XMCD?

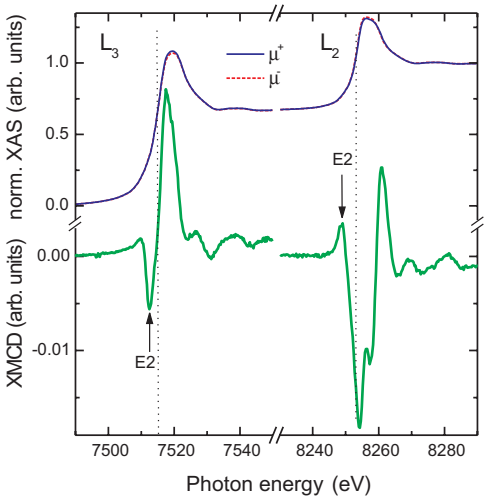

Figure 36. Normalized Tb absorption (up) and XMCD (bottom) spectra [97] at 10 K and 7 T. Possible quadrupolar transitions (2p → 4f) are marked with arrows (E2).

How can these contributions be disentangled? What is the influence of the spin-dependence of the E1 transition matrix elements on the spectral shape of the XMCD spectra? How can this effect be corrected in the sum rule analysis?

The measurements presented here have been carried out using a Tb single crystal. The small static disorder of a single crystal helps to analyse the fine structures in the XMCD spectra, as for example the onset of the magnetic EXAFS oscillations (see section 5.4) that are also detectable in the near-edge regime. The data have been taken at the ESRF beamline ID12 at 10 K using the fluorescence yield detection mode [97]. At this temperature Tb is in the ferromagnetic state. The data have been corrected for self-absorption effects according to [248]. The Tb single crystal was mounted at normal incidence to the x-rays with the c-axis parallel to the photon k-vector. The XMCD signal was achieved consecutively by flipping the magnetic field of 7 T which was applied along the photon k-vector and by reversing the helicity of the x-rays. It was assured that the sample was magnetically saturated by investigating the field dependence of the magnetization $M(H)$. The experimental results for the helicity-dependent x-ray absorption coefficients at 10 K and the corresponding XMCD spectra are presented at the upper and lower part of figure 36, respectively. Although, a difference can hardly be made out by eye between the x-ray absorption coefficients for right and left circularly polarized x-rays $\mu^+(E)$ and $\mu^-(E)$, various fine structures can be identified in the XMCD spectra which are nearly free of noise. In the pre-edge regime sharp features are resolved (marked by arrows) which exhibit a different sign than the corresponding main signals. It will be shown later that these structures can be assigned to the E2 transitions. The main XMCD signal at the L_3 edge is mostly positive whereas the L_2 edge signal is mostly negative. This main signal at the L_2 edge exhibits a pronounced shoulder which is located about 5 eV above the absorption edge. The resolution of this fine structure clearly reveals the improvement of the quality of the XMCD data by the use of a single-element single crystal investigated at a third generation synchrotron radiation facility since this structure could not be detected in earlier investigations [296]. Furthermore, the magnetic EXAFS oscillations in the onset of the extended energy range can be identified. At first glance the signs of the E1 and the E2 contributions are quite surprising. The reason for the negative sign of the quadrupolar contribution at the L_3 edge can be given in a

simple picture: the '+' polarization excites the photoelectron to the majority band whereas the '−' polarization promotes the electron to the minority band (figure 4). The quadrupolar signal at the L_3 edge is proportional to the difference of the majority and minority states. Since all the majority 4f states are occupied, one expects a negative quadrupolar XMCD contribution at the L_3 edge which is indeed found in the experimental spectra. Due to the stronger Coulomb interaction of the 4f states with the core hole this E2 contribution appears in the pre-edge regime [218]. However, if this simple picture is used to discuss the sign of the E1 contribution one yields results which are at odds [83] with total magnetization measurements. Since the E1 signal is mostly positive, one would falsely conclude that the induced 5d moment is aligned antiparallel to the 4f moment. To see this conflict the total moment of Tb of $9.34\mu_B$ [305] must be discussed. In an atomic framework (Hund's rules) the spin contribution from the eight 4f electrons is $+6.0\mu_B$, and the orbital contribution is at most $+3.0\mu_B$. Thus the remainder is attributed to the 5d spin moment, which must be positive and larger than $+0.3\mu_B$, and therefore is aligned parallel to the 4f spin moment, as it is similarly discussed for Gd [213, 214]. The same conflict is found when applying the integral sum rule analysis to the experimental spectra. The origin of this apparent inconsistency is the spin dependence of the E1 transition matrix elements. Therefore, the assumption that the XMCD signal represents the spin-dependent DOS $\Delta\mu \propto \rho^{\uparrow} - \rho^{\downarrow}$ as it has been done in the pioneering rare earth XMCD works [96] is not correct for the $L_{2,3}$ edge XMCD for rare earth metals. One rather has to take the spin-dependent dipole matrix elements $\mu^{\uparrow}$ and $\mu^{\downarrow}$ into account [83] and therefore $\Delta\mu \approx [\mu^{\uparrow}\rho^{\uparrow} - \mu^{\downarrow}\rho^{\downarrow}]/4$ [51]. The reason for this dramatic effect lies in the exchange potential of the 4f electrons which is attractive for spin-up and repulsive for spin-down electrons [219]. Hence, the 5d spin-up radial wave function tends to be pulled in (compressed) while the 5d spin-down radial function is pushed out, which results in a larger dipole matrix element for spin-up electrons, i.e. $\mu^{\uparrow} > \mu^{\downarrow}$. Due to this spin dependence, the XMCD spectra *do not* simply reflect the profile of the spin DOS $\rho^{\uparrow} - \rho^{\downarrow}$ as it is often assumed. Hence, the determination of spin and orbital moments by applying the original integral sum rules to rare earth elements yield questionable results [297]. The discussion above reveals that two steps have to be carried out in order to determine the 5d moments from the experimental $L_{2,3}$ spectra for rare earth metals: (1) the E1 contributions must be disentangled from the E2 ones. (2) The spin dependence of the transition matrix elements must be included in the sum rule analysis of the E1 contribution.

Concerning point (1) the angular dependence of the XMCD experimental spectra was studied in detail in earlier works because the E1 and E2 contributions exhibit different angular dependencies (see, e.g. [220, 222, 224, 298]). Unfortunately, for all investigated angles an overlap of these contributions is determined. Hence, a separation of the dipolar and quadrupolar contributions using this method is not straight forward. Therefore, we applied a different approach here. It is the advantage of theoretical calculations that certain mechanisms can be switched on and off easily (e.g. the quadrupolar and dipolar transitions). To carry out these calculations we used a real space Green's function approach, which is implemented in the FEFF8 code [91]. The E1 and E2 contributions were calculated separately and are compared to the experimental XMCD in figure 37. Because of the narrowness of the 4f bands the default atomic configuration was redefined to the 'solid state' configurations instead of using the atomic configurations to help convergence. In order to reproduce the peak separation the Dirac–Harra self-energy was used. Since the FEFF code is not self-consistent with respect to spin-density, the theoretical results had to be scaled down to match the experimental data. However, the line shape of the calculated E1 and E2 contributions nicely reproduce the experimental data. This confirms that the sharp features in the pre-edge regime indeed stem from the electric quadrupolar transitions (dotted lines in figure 37) whereas the main signals at both edges are due to the electric dipolar transitions (dashed lines). Furthermore, the calculations reveal that

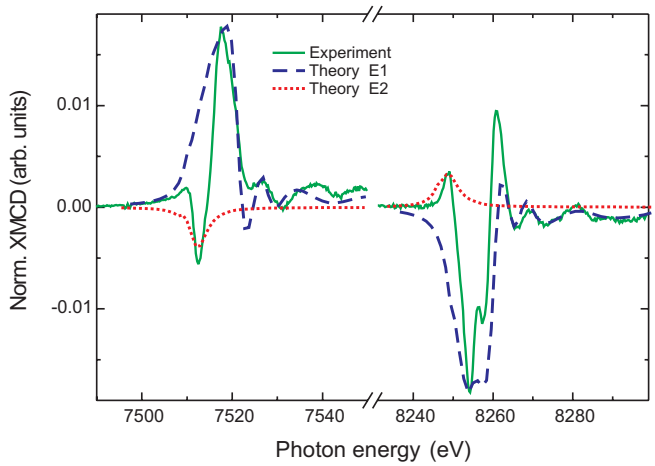

Figure 37. Comparison of experimental (——) and theoretical XMCD spectra (FEFF) at Tb L_3 (left) and L_2 (right) edges: dipolar (- - - -) and quadrupolar (· · · · · ·) contributions [97].

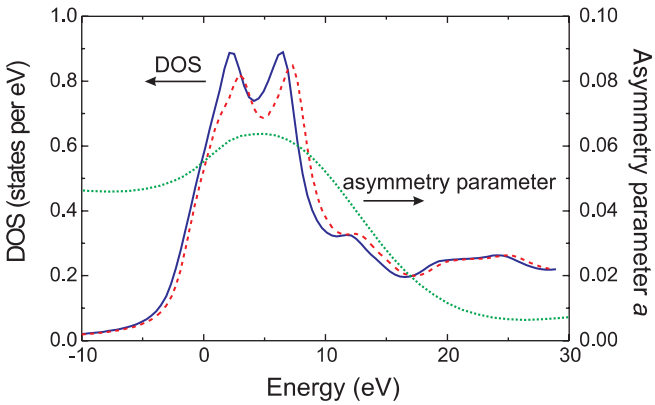

Figure 38. Density of states for spin-up (——) and spin-down (- - - -) electrons in Tb using the FEFF8 code [83]. The asymmetry parameter a (· · · · · ·) characterizes the difference from unity of the ratio between spin-up and spin-down matrix elements (equation (16)). The zero of the energy is the Fermi level E_F.

the dipolar contribution exhibits a derivative-like line shape of the isotropic XAS spectra [296]. This allowed us to establish a procedure to disentangle the E1 and E2 contributions directly from the experimental data as it is presented in detail in [97].

After separating these two structures (E1, E2) in the experiment, the spin dependence of the E1 transition matrix elements has to be taken into account in order to determine the 5d moment. If this dependence is ignored the result of the standard integral sum rule analysis applied to the experimental spectra is $\mu_S = -0.27\mu_B$. This again emphasizes the conflict with the total magnetization measurements from which a positive 5d moment is expected. The same sign problem is found in applying the integral sum rule analysis to the calculated spectra: to show this we use the same density matrix $\rho(E)$ to calculate both the XMCD signal (figure 37) and the spin-dependent electron DOS for Tb (figure 38). From the difference in the DOS, the spin moment is positive and has a value $\mu_S \approx +0.16\mu_B$. However, the integral sum rule analysis applied to the calculated XMCD gives a negative spin moment of $\mu_S = -0.60\mu_B$ [83]. Instead, we used

the FEFF code which takes the spin dependence of the transition matrix elements into account and thereby reproduced the sign and the experimental spectral shape of the E1 contribution (figure 37). Therefore, this calculated spin dependence can be used to correct the results of the sum rule (SR) analysis which increases their generality and utility. Here, we suggest a practical procedure to extract spin and orbital moments by combining experimental measurements and theoretical calculations. Therefore, a 'spin-asymmetry parameter' is defined which enters into the sum rules. However, the general form of the sum rules is kept. It turns out that the spin dependence is of importance especially for the spin sum rule if the number of holes is large. Furthermore, the corrections due to the finite integration range [306] are automatically taken into account. The problem of removing the magnetic dipole contribution T_z (see, e.g. [84]) is also analysed below. The dimensionless spin-asymmetry parameter is defined as:

$$a_j \equiv \frac{R_{j,nl\uparrow} - R_{j,nl\downarrow}}{R_{j,nl\uparrow} + R_{j,nl\downarrow}}. \tag{16}$$

Here, $R_{j,nl\uparrow}$ represents the matrix element the for majority spin and $R_{j,nl\downarrow}$ that for the minority spin. If one defines $R_{j,nl} \equiv 1/2(R_{j,nl\uparrow} + R_{j,nl\downarrow})$, one yields $R_{j,nl,m_s} = R_{j,nl}(1 - 2a_j m_s)$, where $m_s = \pm 1/2$ corresponds to spin-down(up), respectively. It is a warrantable assumption that a_j is basically independent of j, since the matrix elements are essentially j-independent in the original derivation [78]. Hence, the effects of the spin dependence on the matrix elements are the same at the L_3 as well as at the L_2 absorption edges. Hence, the spin dependence is taken into account by simply substituting the above m_s dependent definition of R_{j,nl,m_s}, instead of the spin-average. The spin asymmetry parameter a is given in figure 38. It can be seen that a is clearly energy-dependent (see also [53]) and exhibits a maximum of $\approx$0.06 at about 5 eV above the Fermi level. This is in the vicinity of the XMCD maximum. At the L_3 edge, using right circularly polarized x-rays, the photoelectron is excited basically into the majority spin band. Consequently, with left circularly polarized x-rays, the minority band is reached which possesses more empty states. Therefore, one expects a negative XMCD signal at the L_3 edge. However, for the case discussed here the density of empty states for the majority spin is apparently enlarged by the spin-asymmetry parameter whereas the minority spin DOS is seemingly reduced: hence, the wrong sign of the induced spin moment is determined with the XMCD technique if this effect is not taken into account.

Our detailed calculation given in [83] reveals that in order to account for the spin dependence it is sufficient to substitute for each operator $\hat{O}$

$$\langle \hat{O} \rangle \rightarrow \langle (1 - 2as_z)\hat{O}(1 - 2as_z) \rangle, \tag{17}$$

where s_z is the z-component of the one-electron spin operator. Since all operators are modified in the same way, their linear combinations entering into the SR must also be modified similarly. In our discussion, presented in [83], first the differential sum rules (i.e. SR for each energy point) are derived. For the differential SR a distributed oscillator strength is present and the spin asymmetry parameter becomes energy-dependent $a = a(E)$ (for the analysis of the energy dependence of the transition matrix elements see also [53]). However, we will neglect the energy argument below unless needed for clarity. With this knowledge the ratio of the integrals for XMCD and for the average absorption can be related to expectation values of the total operators (summed over all electrons) $\langle S_z \rangle$ and $\langle L_z \rangle$ by the generalized form of the integral sum rules [83]:

$$\frac{2\tau}{3}\frac{\langle S_z \rangle - \Delta S_z}{N_h + \Delta N_h} = \frac{\int_{L_3} \mathrm{d}\omega(\mu^+ - \mu^-) - 2\int_{L_2} \mathrm{d}\omega(\mu^+ - \mu^-)}{\int_{L_3+L_2} \mathrm{d}\omega(\mu^+ + \mu^- + \mu^0)}, \tag{18}$$

$$\frac{1}{2}\frac{\langle L_z \rangle - \Delta L_z}{N_h + \Delta N_h} = \frac{\int_{L_3+L_2} \mathrm{d}\omega(\mu^+ - \mu^-)}{\int_{L_3+L_2} \mathrm{d}\omega(\mu^+ + \mu^- + \mu^0)}. \tag{19}$$

Here, ΔS_z, ΔL_z and ΔN_h are the spin-dependent correction terms for the spin and the orbital expectation values as well as the number of d-holes. These can be estimated from the theoretical calculations [83]:

$$\Delta S_z = \int_{E_F}^{\infty} \mathrm{d}E(-an_h + a^2 s_z) \approx -a^* N_h, \tag{20}$$

$$\Delta L_z = \int_{E_F}^{\infty} \mathrm{d}E(l_z a^2 - 4a l_z s_z), \tag{21}$$

$$\Delta N_h = \int_{E_F}^{\infty} \mathrm{d}E(n_h a^2 - 2a s_z), \tag{22}$$

where n_h is the energy-dependent hole operator. We account for the magnetic dipole term T_z in equation (18) by introducing τ which is given by: $\langle S_z\rangle + (2\ell+3)/\ell\langle T_z\rangle = \tau\langle S_z\rangle$. For the final 4f states τ can be estimated analytically from Hund's rules as presented similarly by Carra *et al* [78]. For many bulk systems the magnetic dipole term can be neglected and hence $\tau \approx 1$ as it has been tested by calculations for the final d-electrons. However, for atoms on surfaces τ can be significantly different from unity, and can even be directionally dependent [84]. To investigate the primary contribution to T_z, we assume that the 5d electron spin and angular momentum decouple (see [83] for details). This yields

$$\tau \approx 1 + \frac{4\langle Q_{zz}\rangle}{l(2l-1)}, \tag{23}$$

where we used the definition $\langle Q_{zz}\rangle = [3\langle l_z^2\rangle - \ell(\ell+1)]/2$ as given in [218]. Interestingly, most of the spin-dependent corrections are relatively small because ΔO is mainly determined by the operator $\langle O\rangle$ itself times $|a|$ to a certain power. Since here $a^2 < 0.01$ the original sum-rules can be reasonable approximations for those cases where the above assumption is valid. The exception is the correction to the spin moment which can be large, since $|\Delta S_z/\langle S_z\rangle| \approx |a^*|N_h/\langle S_z\rangle$. This is the case for the 4f metals where the number of the 5d holes is $N_h^{5d} \approx 9$ and $|\Delta S_z/\langle S_z\rangle| > 18|a^*|$. Therefore, we focus on this sum rule here. For Tb, $a(E)$ (figure 38) is varying smoothly and is about $a^* = 0.05$ near the maximum XMCD signal. This implies that the correction to the spin moment is $a^* N_h \approx 0.45$ which has to be compared to the calculated spin moment of $\langle S_z\rangle \approx -0.08$ from the difference in the DOS (figure 38). This reveals that even if a is small, the correction to the spin SR is significant when the number of holes N_h is large and can be even larger than the extracted quantity itself. It can be seen from equation (20) that the experimentally measured moment is proportional to $\langle S_z\rangle + a^* N_h$, and therefore the correction can even change the sign of the integral spin sum rule result.

Now, a procedure is suggested to extract spin and orbital moments from XAS data using the generalized sum rules. This procedure also makes use of theoretical calculations as it is the case for the original sum rules, which rely on theoretical calculations or estimates of N_h and T_z. Using the FEFF8 code [91] we calculate the expectation value of a certain operator $\langle O\rangle_{\mathrm{calc}}$ and also apply the original sum rule analysis to the calculated spectra which yields $O^{\mathrm{SR}}_{\mathrm{calc}}$. Then the discrepancy between these two results ΔO is used to correct the experimental estimate $O^{\mathrm{SR}}_{\mathrm{exp}}$ which is determined by the original sum rule analysis to the experimental spectra. Thus, the procedure is given by

$$\Delta O = \langle O\rangle_{\mathrm{calc}} - O^{\mathrm{SR}}_{\mathrm{calc}}, \tag{24}$$

$$\langle O\rangle_{\mathrm{exp}} = O^{\mathrm{SR}}_{\mathrm{exp}} + \Delta O. \tag{25}$$

It should be noted that this approach accounts not only for the corrections due to the spin-dependent matrix elements, but also for the finite integration range. A further modification is

needed in order to consider the T_z operator. This is done by assuming that T_z is proportional to S_z, i.e. $\langle S_z \rangle = S_z^{\mathrm{SR}}/\tau + \Delta S_z$. The correction for a given operator may be calculated more accurately than the operator itself. The FEFF8 code is based on an independent electron theory with an approximate self-energy. However, the code is not self-consistent with respect to the spin-density, and hence the calculated spin moment may not be very accurate. Fortunately, the dominant correction to the spin SR is $\int \mathrm{d}E\, a(E) n_h(E)$, where $n_h(E)$ is spin-independent, while $a(E)$ is expected to be directly proportional to the total spin of the absorber. For rare earth applications the spin is dominated by the 4f contributions, and thus is practically independent of the 5d spin moment.

The above procedure is now applied to the Tb $L_{2,3}$ data shown in figure 36. Since the SR are derived assuming dipole transitions, the quadrupolar contributions to XMCD are subtracted from experimental data, as discussed above [97]. We use the FEFF8 code to calculate the XMCD spectrum and the operators of interest obtaining $\langle S_z \rangle_{\mathrm{calc}} = -0.08$ and $\tau = 1.59$. The application of the spin SR to the calculated XMCD gives $S_{\mathrm{calc}}^{\mathrm{SR}} = +0.30$, and therefore $\Delta S_z = \langle S_z \rangle_{\mathrm{calc}} - S_{\mathrm{calc}}^{\mathrm{SR}}/\tau = -0.27$. This value is then used to correct the experimental XMCD SR results of $S_{\mathrm{exp}}^{\mathrm{SR}} = +0.135$, and we obtain a 5d spin moment of $\mu_S = +0.37\,\mu_{\mathrm{B}}$ from the experiment. This result is consistent with the total magnetization measurement, which requires it to be larger than $+0.34\,\mu_{\mathrm{B}}$. Note that if we neglect T_z and use $\tau = 1.0$, we obtain $\mu_S = +0.49\mu_{\mathrm{B}}$ from the experiment. The same procedure for the orbital moment gives a correction which is an order of magnitude smaller $\Delta L_z = 0.014 - 0.008 = +0.006$, but still a significant fraction of the FEFF8 result $\langle L_z \rangle_{\mathrm{calc}} = +0.014$. The application of the orbital SR to the experiment gives $L_{\mathrm{exp}}^{\mathrm{SR}} = 0.021$ and adding the correction ΔL_z we determine the orbital moment of $\mu_L = -0.027\,\mu_{\mathrm{B}}$ from the experiment. Hence for the orbital SR, the correction appears to be dominated by the finite integration range because a magnetic background can be identified in figure 36 that extends far above the Fermi level. However, for the spin SR the correction is dominated by the spin dependence of the matrix elements.

In conclusion, we have shown that the spectral shape of the Tb $L_{2,3}$ edge XMCD in the pre-edge regime is dominated by electric quadrupolar transitions. In order to determine the 5d moments from the spectra these E2 contributions have to be identified and subtracted from the data. We demonstrated that this identification is possible by the help of *ab initio* calculations where the E1 and E2 contributions were calculated separately. Furthermore, the strong spin dependence of the dipole transition matrix elements for the RE metals has to be considered. Therefore, even after separating the E2 from the E1 contributions, the results of the sum rule application have to be corrected for this effect with the help of the theory. If these corrections are not carried out, an apparent 5d spin moment per atom of $\mu_S^{\mathrm{5d}} = -0.27\mu_{\mathrm{B}}$ is determined from the experiment and hence erroneously an antiparallel orientation of the 5d to the 4f moments would be concluded. However, we show in which way the XAS sum rules can be generalized by including the spin dependence of the matrix elements in the sum rule analysis. With this procedure we obtained $\mu_S^{\mathrm{5d}} = +0.37\mu_{\mathrm{B}}$ from the experiment, accentuating the need for this correction. This correction brings XMCD data in agreement with the total magnetization measurement, which predicts that the 5d contribution $\mu_S + \mu_L > +0.34\mu_{\mathrm{B}}$. Using the calculated $\tau = 1.59$, we obtain $\mu_S + \mu_L = +0.34\mu_{\mathrm{B}}$. The inclusion of these spin-dependent corrections into the standard sum rule analysis thus permits a more reliable determination of magnetic moments with the XMCD technique, and therefore makes the technique more robust and more generally useful. This now opens the new, fascinating possibility to use the XMCD technique with its full strength also for rare earth elements and compounds in order to determine the spin and orbital magnetic moments element and shell specifically.

5.4. L edge magnetic EXAFS: Gd and Tb

In the preceding section already an oscillatory fine structure could be detected in the magnetic background of the XMCD signal starting about 20 eV larger than the L_3 edge position. This is the onset of the magnetic EXAFS signal (MEXAFS) which originates from the spin-dependent scattering of the photoelectron. Hence, the MEXAFS is related to the local magnetic structure of the sample investigated. The analysis of the dichroic signal in this energy range is especially interesting for rare earth metals. The rare earth MEXAFS at the $L_{2,3}$ edges is essentially proportional to the 4f magnetic spin moment [76, 307, 308] whereas the near-edge XMCD is dominated by dipole transitions to the spin-dependent 5d DOS only (see above). Therefore, the rare earth MEXAFS intensity in relation to the near-edge XMCD signal is larger compared to the 3d transition metals where MEXAFS and XMCD scale with the 3d magnetic moment. Gd metal is a model system for the investigation of the magnetic EXAFS effect. One reason is that Gd can be described in a good approximation by a half-filled 4f shell and therefore $\langle L_z \rangle \approx 0$ which facilitates the theoretical description (see, e.g. [51]). The first MEXAFS oscillations were detected for a Gd metal foil at 100 K [228]. Since then the Gd MEXAFS was discussed in various experimental [308–312] and theoretical works [51,313,314]. Looking at the enormous work on this subject it is surprising that no temperature-dependent investigations of the rare earth L edge MEXAFS were carried out yet, as we have demonstrated for 3d transition metals [130,225,230,266,315]. Nowadays, the theoretical descriptions of the MEXAFS effect are quite advanced. However, the magnetism is modelled at $T = 0$ K [52, 54, 316, 317]. This reveals that no comprehensive theory existed so far for the detailed temperature dependence of MEXAFS which originates both from spin fluctuations and lattice vibrations. However, up to now it was not clear how to separate these effects. Another open question is, in which way local spin-fluctuations on a nearest neighbour scale influence MEXAFS. Therefore, we carried out the first temperature-dependent study at the L edges of a Gd single crystal [226,227]. Another reason to choose Gd was that no helical magnetic phase is present at any temperature, in contrast to Tb and Dy, for example. Bulk Gd is ferromagnetic up to $T_C = 293$ K. This relatively low Curie temperature allowed us to study MEXAFS in a wide range of the reduced temperature $t = T/T_C$. This was not possible in our earlier temperature-dependent MEXAFS investigations at the $L_{2,3}$ edges of bulk Fe where only $T/T_C \approx 0.4$ was reached [225,230,315] because of the larger value of $T_C = 1043$ K.

The use of a single crystal sample enabled us to discuss high quality MEXAFS data with small static disorder at the L_3 edge up to $k_{max} = 13.0$ Å^{-1}, which were therefore used for the detailed analysis. This k-range is larger compared with the L_2 edge range which is limited by the L_1 edge. Furthermore, MEXAFS at a single absorption edge can be investigated for rare earth metals in contrast to the 3d transition metals where the largest signal is found at the $L_{2,3}$ edges, which overlap [130, 230][2]. The Gd(0001) single crystal with a shape of a plate (c-axis normal to the surface) was mounted so that the x-rays were incident normal to the surface ($\vec{k}_{photon} \parallel c$-axis). The L edge MEXAFS data were measured at the ID 12 beamline [319] at the ESRF at 10, 100, 200 and 250 K corresponding to reduced temperatures of $t = 0.034$, 0.34, 0.68 and 0.85. To ensure that the sample was completely saturated, the magnetization $M(H)$ versus the magnetic field was measured at each temperature point. Since the saturation field H_S was changing with temperature, the MEXAFS data were recorded at the same reduced field $H/H_S = 1.2$. From the $M(H)$ curves the following applied magnetic fields for the

[2] Generally, the K edge MEXAFS of 3d metals could be investigated in order to circumvent this difficulty and to access a longer k-range. However, the dichroic signal at the K edge is about an order of magnitude smaller compared to the $L_{2,3}$ edge signals because of the lower spin-polarization of the photoelectron at the K edge which originates from the spin–orbit splitting in the final p states. Furthermore, the K edge MEXAFS signal is related to the orbital polarization only [308, 312, 316–318].

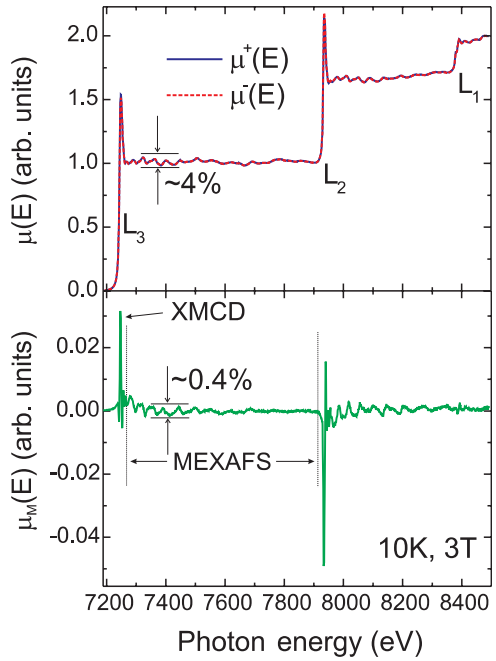

Figure 39. X-ray absorption coefficient at the Gd L_3, L_2 and L_1 edges for right $\mu^+(E)$ and left $\mu^-(E)$ circularly polarized x-rays (top) [227]. The dichroic signal $\mu_M(E) = \mu^+(E) - \mu^-(E)$ is given at the bottom. A clear oscillatory fine structure can be detected in the isotropic data (EXAFS) and the dichroic signal (MEXAFS).

MEXAFS measurements were determined: 3.0 T (10 K), 2.8 T (100 K), 2.5 T (200 K) and 2.0 T (250 K). The fluorescence of the sample was detected with silicon photodiodes [320] and the resulting data were corrected for self-absorption effects [248]. To measure EXAFS and MEXAFS in the energy range of 7185–8500 eV with a constant degree of circularly polarized x-rays the undulator gap-scan technique was used [321]. We measured the dichroic signal $\mu_M(E) = \mu^+(E) - \mu^-(E)$ in two ways: by changing the direction of the magnetization for a fixed helicity and by changing the helicity of the x-rays for a fixed magnetization. Both methods revealed the same dichroic signal indicating that no experimental artefacts were observed. The x-ray absorption coefficients for right $\mu^+(E)$ and left circularly polarized x-rays $\mu^-(E)$ in the range of the Gd L_3, L_2 and L_1 edges are presented in the upper part of figure 39 in a scan-range of $\Delta E = 1300$ eV. The EXAFS oscillations are about 4% of the signal to background ratio (edge jump). In the lower part of figure 39 the dichroic signal is presented. This signal is shown here according to the discussion of the sign of XMCD in section 5.3: the L_3 edge XMCD signal of the rare earth metal Gd is mostly positive and the L_2 one is basically negative because of the spin dependence of the transition matrix elements[3]. Figure 39 reveals that in the dichroic signal an obvious oscillatory fine structure can be identified in the extended energy range—the magnetic EXAFS, which is about 0.4% of the L_3 edge jump. Hence, the MEXAFS is about an order of magnitude smaller compared to the normal EXAFS

[3] In contrast, in our earlier works [225–227] we adopted the presentation of the rare earth MEXAFS by Ahlers *et al* [312] with opposite sign of the dichroic signal in order to compare the magnetic background in the extended energy range to the one found for the 3d metals. However, the proper definition of the sign of the dichroic signal is discussed in section 5.3. The MEXAFS signals presented in our earlier works [225–227] have to be multiplied by −1 to correspond to the ones given here.

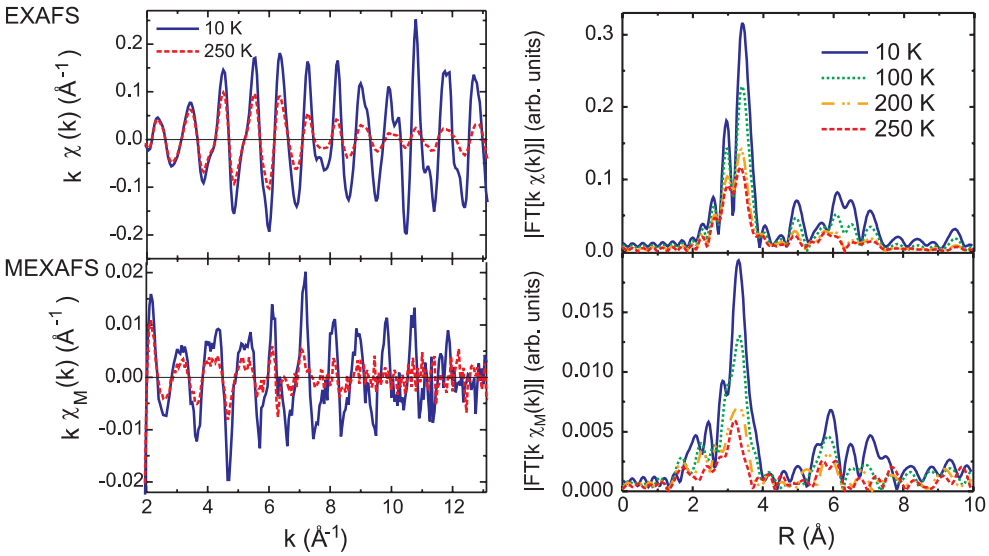

Figure 40. Temperature-dependent Gd L_3 edge EXAFS (top) and MEXAFS (bottom) oscillations (left) $k\chi(k)$ and $k\chi_M(k)$, and the corresponding Fourier transforms (right) $|FT[k\chi(k)]|$ and $|FT[k\chi_M(k)]|$ [226]. For the EXAFS and the MEXAFS Fourier transforms a clear splitting of the main peak due to the so-called RT resonance can be detected.

signal. The clear visibility of the oscillations in the dichroic signal emphasizes the excellent signal-to-noise ratio. The analysis of the MEXAFS wiggles reveals that the noise level in the present case is about 0.01% of the edge jump underlining the high performance of the beamline and the detection system. The EXAFS and MEXAFS oscillations were extracted with a standard spline-analysis as described in [130]. For that purpose a smooth magnetic background was subtracted from the difference $\mu_M(E)$ in order to extract the MEXAFS oscillations $\chi_M(k)$.

The temperature-dependent EXAFS and MEXAFS data are presented in figure 40. The Fourier transformed data of EXAFS and MEXAFS exhibit a clear splitting of the main peak due to the so-called Ramsauer–Townsend (RT) resonance. The splitting of the main peak corresponds to a minimum of the enveloping amplitude in k-space at about $k = 9\,\text{Å}^{-1}$. This indicates a clear improvement of the quality of the MEXAFS data compared to spectra published previously where these features could not be detected [308, 310]. One reason might be that the measurements in earlier works were not carried out with a single crystal but with metal foils at 100 K [228]. Therefore, one expects a much stronger effect of static and dynamic disorder on EXAFS and MEXAFS compared to the results for a Gd single crystal at 10 K, as presented here. Furthermore, a k-weighting of k^1 was used in our work, whereas the Fourier transforms of the simple EXAFS ($|FT[\chi(k)]|$) and MEXAFS ($|FT[\chi_M(k)]|$) oscillations are discussed in the earlier works [228, 308, 311]. As shown in figure 40, a clear temperature dependence for EXAFS as well as MEXAFS can be determined. For a quantitative analysis of the temperature dependence of the regular EXAFS we carried out a fit of the main peak in R-space using the FEFFIT code [92]. The fit (not shown) reveals that the reduction of the intensity of the main peak due to the EXAFS Debye–Waller factor can be accurately described within the correlated Debye model. With the help of the FEFFIT analysis a Debye temperature of $\theta_D = (160 \pm 7)$ K is calculated in good agreement with 163.4 K given in the literature from heat capacity measurements [322]. This value is relatively low compared for instance to 3d

transition metals, where values of about $\theta_D = 350$–$450\,K$ are found. Surprisingly, the effect of lattice vibrations is often neglected in various MEXAFS works even when intensities in the Fourier transforms are compared to investigate magnetic moments quantitatively [323]. This can lead to erroneous results, since the Debye temperatures of these materials differ seriously. Therefore, when MEXAFS intensities are compared, the data must be corrected not only for temperature dependence of the magnetization (reduced temperature T/T_C) but also for the lattice vibrations (EXAFS Debye–Waller factor). A Debye temperature of $\theta_D = 160\,K$ for a Gd metal foil also explains the strong damping of the EXAFS and MEXAFS already at $T = 100\,K$ as determined in the earlier works by Ahlers *et al* [308]. A clear temperature-dependent damping of MEXAFS is revealed in our experiment (figure 40): the MEXAFS wiggles $\chi_M(k)$ at $k = 4.5\,\text{Å}^{-1}$ are damped at $T = 250\,K$ to about 50% of their $T = 10\,K$ value. However, the wiggles are hardly detectable for $k = 10.0\,\text{Å}^{-1}$ at $T = 250\,K$, whereas they can be seen obviously at $T = 10\,K$ in the same k-range. This is an indication that the thermal disorder also decreases the MEXAFS signal by the EXAFS Debye–Waller factor $e^{-2\sigma^2k^2}$ in addition to the magnetic fluctuations.

The procedure applied in this work to disentangle the effect of the lattice vibrations from the spin fluctuations is based on the description of MEXAFS in various theoretical works: the MEXAFS fine structure is related to the energy derivative of the DOS which is linked to the derivative of the spin-averaged EXAFS [51, 52, 310, 314]. Ebert and co-workers showed that the MEXAFS fine structure is connected to the spin and orbital polarization $(d/dE)\langle\sigma_z\rangle$ and $(d/dE)\langle l_z\rangle$ by analysing sum rules in their differential form [79, 312, 316, 317, 324]. Even in the near-edge range similar theoretical treatments can be found [31, 325]. In a simplified picture MEXAFS can be described as the difference of the spin-dependent scattering at the potentials which are modelled from the normal EXAFS scattering potentials being shifted in energy by an exchange-related energy $\Delta E(T)$. In this case the MEXAFS oscillations can be simulated with χ_M^{sim} by calculating the difference of the regular EXAFS oscillations χ which are shifted in energy by $\pm\frac{1}{2}\Delta E$ [326]:

$$\chi_M^{sim}(E,T) = \chi\big(E - \tfrac{1}{2}\Delta E(T)\big) - \chi\big(E + \tfrac{1}{2}\Delta E(T)\big). \tag{26}$$

To test this assumption we applied this procedure to the experimental Gd MEXAFS data at 10 K and simulated them with the experimental EXAFS spectra at the same temperature. The only free parameter to fit the experimental data according to equation (26) is the energy shift ΔE which is varied until the simulated MEXAFS intensities match the experimental ones. The results are given in figure 41(*a*). With this procedure a value of $\Delta E_{Gd} = (0.48 \pm 0.05)\,eV$ is determined for Gd which will be related to the one for Tb below. Surprisingly, this simple approach can reproduce various fine structures of the experimental MEXAFS seen for instance at $k = 4.0\,\text{Å}^{-1}$ for Gd. Also the enveloping amplitude of MEXAFS is correctly described. This demonstrates that the rigid-band model as suggested by Brouder *et al* [314] holds for the modelling of MEXAFS even up to large k-values of about $11\,\text{Å}^{-1}$. It turns out that the shape of the L edge MEXAFS can be described by the first derivative of the EXAFS $d\chi/dE$ and $\Delta E(T)$ is there to scale the intensity. Thinking in terms of a Taylor series the higher order terms can be neglected because of the small size of $\Delta E(T)$. This is not the case for K edge MEXAFS where Brouder *et al* [314] showed that MEXAFS is proportional to the second derivative of the EXAFS $d^2\chi/dE^2$ and Ebert *et al* [316] discussed these results on the basis of the differential form of the sum rules. The procedure to disentangle lattice vibrations from spin fluctuations is carried out by simulating MEXAFS at the specific temperature T with the experimental EXAFS data at the same temperature. This automatically takes the reduction by the EXAFS Debye–Waller factor into account. Hence, the temperature dependence of the energy shift ΔE is not due to the influence of

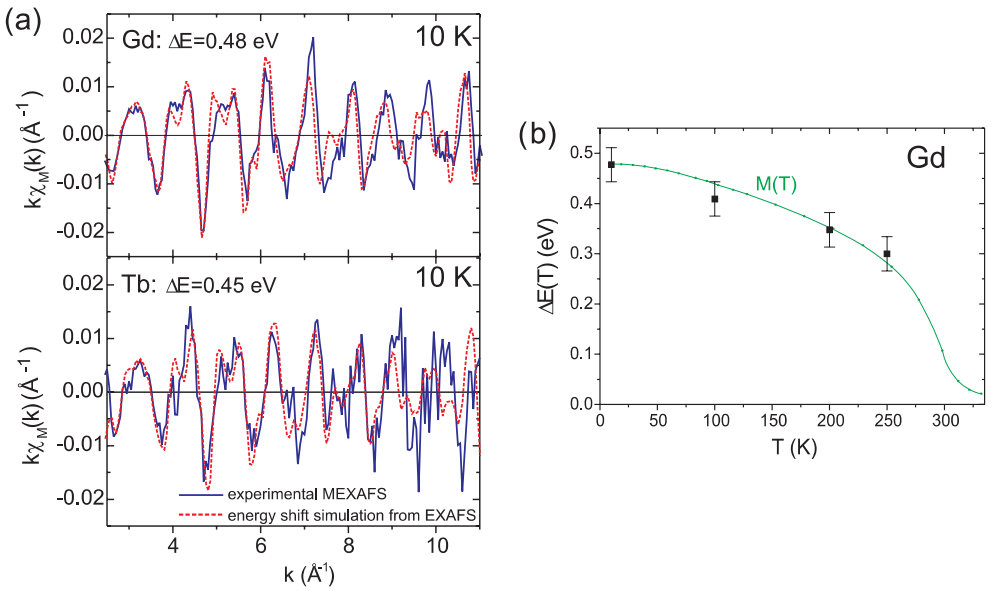

Figure 41. (*a*) Experimental MEXAFS data (——) for Gd (top) and Tb (bottom) single crystals at 10 K in comparison to simulation (· · · · · ·) of MEXAFS with the spin-averaged EXAFS data [326]. For the simulation the difference of the energy shifted EXAFS oscillations $\chi(E-\frac{1}{2}\Delta E)-\chi(E+\frac{1}{2}\Delta E)$ was analysed. (*b*) Temperature dependence of the exchange related energy shift $\Delta E(T)$ for the Gd single crystal in comparison to the temperature dependence of the magnetization (scaled) taken from [327] (applied field of 0.5 T).

the lattice vibrations but spin fluctuations only and therefore these two contributions can be separated[4].

The temperature dependence of the Gd MEXAFS is analysed in detail in order to achieve a more complete understanding of the underlying physics. Therefore, the temperature dependence of $\Delta E(T)$ will be investigated which is determined by fitting the temperature-dependent MEXAFS oscillations with the procedure described by equation (26). The experimental results for Gd are given in figure 41(*b*). Obviously, the temperature dependence of ΔE follows the one of the magnetization $M(T)$ [327], as we have suggested it in our recent theoretical work [307], showing that the temperature dependence of MEXAFS can be described by the factor $M(T)\,\mathrm{e}^{-2\sigma^2(T)k^2}$. Therefore, one has to correct not only for the amplitude reduction by the temperature dependence of the magnetization (reduced temperature T/T_C) but also for the EXAFS Debye–Waller factor when the MEXAFS intensity is correlated to the spin moment [307]. In various MEXAFS works this effect was neglected although there is a strong influence by the factor $\mathrm{e}^{-2\sigma^2(T)k^2}$. This is crucial when the MEXAFS intensity of 3d transition metals is compared to the ones of the rare earths. We observe that local spin–spin correlations cancel for single-scattering paths and the temperature dependence for these paths is determined only by the magnetization $M(T)$. This is different for multiple-scattering paths. Our calculations reveal that double scattering paths contain information on 3-point spin–spin correlation functions [307]. Unfortunately, these contributions are orders of magnitudes smaller than the regular magnetic scattering contributions (being proportional to the spin at

[4] We also applied successfully the simple procedure given by equation (26) to model the $L_{2,3}$ MEXAFS of 3d elements. For these metals the $L_{2,3}$ edges overlap in contrast to the rare earth metals presented here, where the $L_{2,3}$ edges are well separated by several hundred electronvolts.

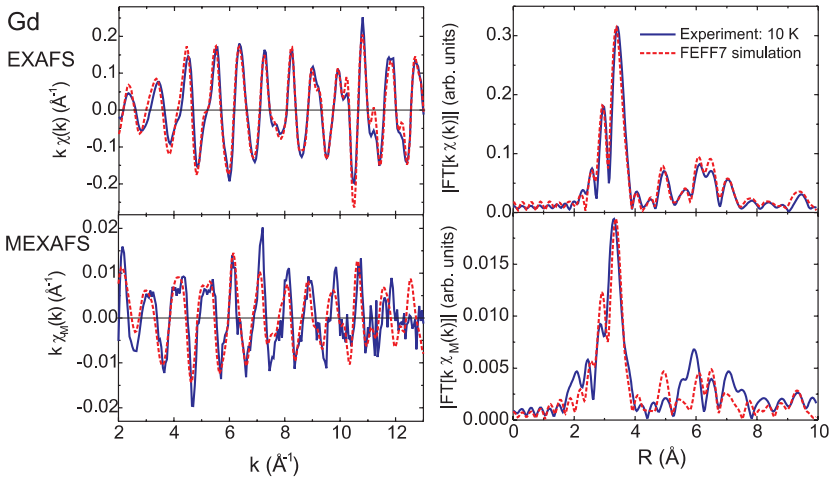

Figure 42. Comparison of the experimental EXAFS (top) and MEXAFS (bottom) data at 10 K to *ab initio* calculations (FEFF7) [226]. The calculations show good agreement for the enveloping amplitude and phase in k-space as well as in R-space for the splitting of the main peak (RT resonance) and the peaks at larger distances.

each scattering site) for the double scattering paths. For a more complete understanding of the nature of the magnetic scattering leading to MEXAFS, the contributions of multiple-scattering paths to MEXAFS will now be analysed by the help of the theory.

The comparison of the experimental Gd data at 10 K to *ab initio* calculations carried out in the framework of a real-space multiple-scattering theory implemented into the FEFF code [91, 328] using bulk Gd structure is presented in figure 42. Since the FEFF calculations are not self-consistent with respect to the spin dependence, the MEXAFS data were scaled down to match the experiment. However, the agreement of the wiggles of the experimental regular EXAFS with the calculation is perfect in k-space as well as in R-space: all the fine structures seen, e.g. at $k = 10.0\,\text{Å}^{-1}$ and $k = 11.5\,\text{Å}^{-1}$, are reproduced in the calculation. Also the enveloping amplitude in k-space in the calculation agrees very well with the experimental data. This can also be seen in R-space, where the splitting of the main peak (RT resonance) as well as the intensities and positions of the peaks at larger distances are correctly described. The presented calculations are carried out including single-scattering and multiple-scattering effects. If one calculates EXAFS without multiple-scattering contributions one finds larger intensities of the peaks in the Fourier transform at about $R = 6\,\text{Å}$ [227]. This shows that in the case of Gd the multiple-scattering contributions interfere destructively with the single-scattering contributions of larger scattering shells. This effect is correctly reproduced by the FEFF code. The agreement of the experimental MEXAFS data with the calculation is also fairly good. The phase shift of about $\pi/2$ of the MEXAFS oscillations $\chi_M(k)$ compared to the EXAFS oscillations $\chi(k)$ is correctly described. The enveloping amplitude of the calculation is in reasonable agreement with the experimental data. Therefore, the splitting of the main peak in the MEXAFS Fourier transform is reproduced in the calculation. Deviations between theory and experiment can be detected in the Fourier transform at larger distances in the range of 4.0–8.0 Å. These differences are not due to the feature seen at $k = 6.3\,\text{Å}^{-1}$ which can be assigned to the so-called magnetic MMEs (MMEEs) [308, 309, 311, 329]. More serious are the differences seen in the k-space in the range of $k = 7.0$–$8.5\,\text{Å}^{-1}$. As the negative and positive part of the experimental wiggle are larger compared to the calculated data, it is not very likely that this difference is also due to MEEs as these lead to an additional feature

only. Therefore, we assign the main differences to scattering effects. It was already discussed for the normal EXAFS data that the single-scattering contributions interfere destructively with the multiple-scattering contributions. It seems that the phase of the multiple-scattering contributions (enhanced in MEXAFS of 3d metals [230]) are not yet described accurately enough in the FEFF7 calculations.

In a further experiment the MEXAFS of Tb was studied. Tb was chosen in order to analyse the effect of the orbital moment on MEXAFS. As discussed in section 5.3 an orbital moment of the 4f electrons of $\mu_L = 3\mu_B$ is expected in an atomic framework. The EXAFS and MEXAFS data were taken using a Tb single crystal with the same experimental set-up described in section 5.3. The same procedure to model the experimental MEXAFS from the experimental EXAFS data with the energy shift procedure was applied first. Also for the case of Tb even detailed fine structures in the MEXAFS can be reproduced, e.g. at $k = 8.0\,\text{Å}^{-1}$ (figure 41(a)). Since the modelled MEXAFS intensity χ_M^{sim} scales with $\Delta E(T)$ the absolute values of this property provides information on the magnetic scattering amplitude. Interestingly, it is found that the 10 K value for Tb of $\Delta E_{\text{Tb}} = (0.45 \pm 0.05)$ eV is only a little smaller than the value for Gd of $\Delta E_{\text{Gd}} = (0.48 \pm 0.05)$ eV. This indicates that indeed the MEXAFS intensity basically scales with the spin moment only since $\mu_S(\text{Gd}) = 7\mu_B$ and $\mu_S(\text{Tb}) = 6\mu_B$ is expected from Hund's rules. In general, the value of $\Delta E(T)$ extrapolated to $T = 0$ K has to be investigated for the discussion given above. However, the detailed temperature-dependent investigation for Gd shows that it is a reasonable approximation to use the $\Delta E(T = 10\,\text{K})$ value as the $T = 0$ K value for our analysis here. Interestingly, a similar scaling of the size of a magnetic splitting of certain valence states (extrapolated to $T = 0$ K) with the spin moment has been determined recently by photoemission measurements [330]. The temperature dependence of bulk Tb is more complicated because of the occurrence of a helical phase in the range of $T = 219$–231 K [331] and has therefore not been studied here.

For the structural investigation the MEXAFS oscillations are Fourier transformed. In order to do so the MMEEs [308, 309, 311, 329] found in k-space at about $k = 6.5\,\text{Å}^{-1}$ have to be removed since these contributions are larger for Tb compared to Gd. The experimental MEXAFS data are given in figures 41 and 43 after the peak-like MMEE structure was removed. To determine the multiple-scattering contributions to MEXAFS we performed *ab initio* calculations. The results of the calculation using the FEFF8.2 code for EXAFS and MEXAFS agree quite well with the experiment in k-space as well as in R-space since all the fine structures are reproduced (figure 43). Interestingly, various fine structures of the MEXAFS that were already seen in the energy shift simulation in figure 41, e.g. at about $k = 5.3$, 6.8 and $7.8\,\text{Å}^{-1}$, can also be detected in the FEFF8.2 results. The splitting of the main peak in the Fourier transforms, which is due to a minimum in the enveloping amplitude at about $k = 9\,\text{Å}^{-1}$, is accurately modelled. Even all the peaks in the Fourier transform for EXAFS and MEXAFS with respect to their position as well as their relative intensity are well described by the theory. In order to disentangle those peaks into their multiple- (MS) and single-scattering (SS) contributions, we used the advantage to switch on/off those effects in the theory. The result of this separation is given in figure 44(a). All the peaks up to 6.0 Å can be described by single-scattering contributions. The triangular scattering path 0–2–2′–0 (figure 44(b)) at about 3.0 Å hardly contributes to the overall intensity. However, at distances larger than 6.0 Å clear contributions from various triangular paths can be found. Surprisingly, smaller intensities are found for the multiple-scattering calculation (solid line) above 7.5 Å. This demonstrates that the multiple- and the single-scattering paths interfere destructively as it was also determined for the Gd MEXAFS [227]. In contrast, such an effect was not seen for the L edge MEXAFS of the 3d metals Fe and Co where even an enhancement of MS paths was found [230].

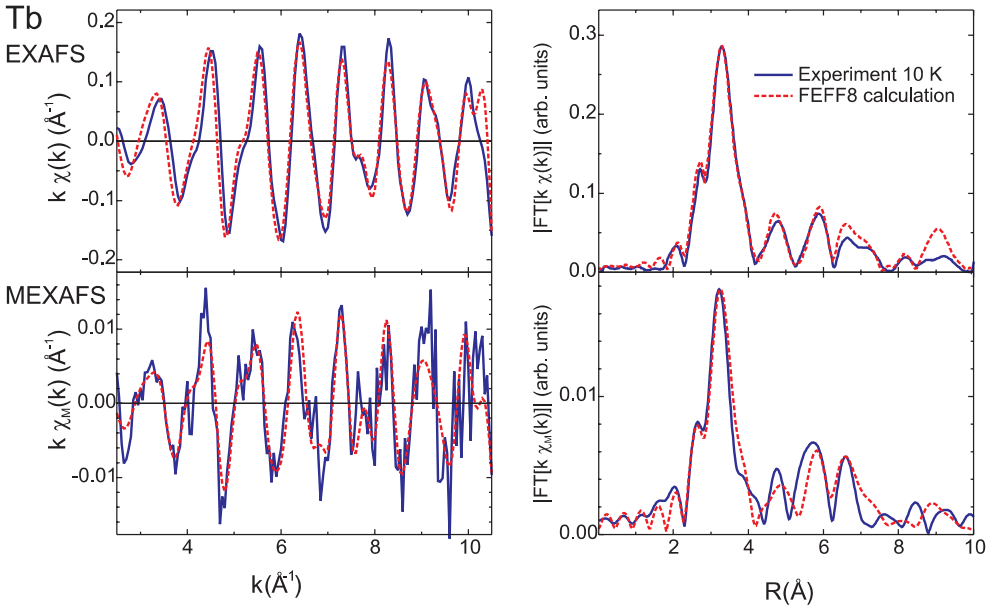

Figure 43. Experimental Tb EXAFS (top) and MEXAFS (bottom) oscillations $k\chi(k)$ and $k\chi_M(k)$ (left) and the corresponding Fourier transforms (right) in comparison to *ab initio* calculations (FEFF8.2) [326].

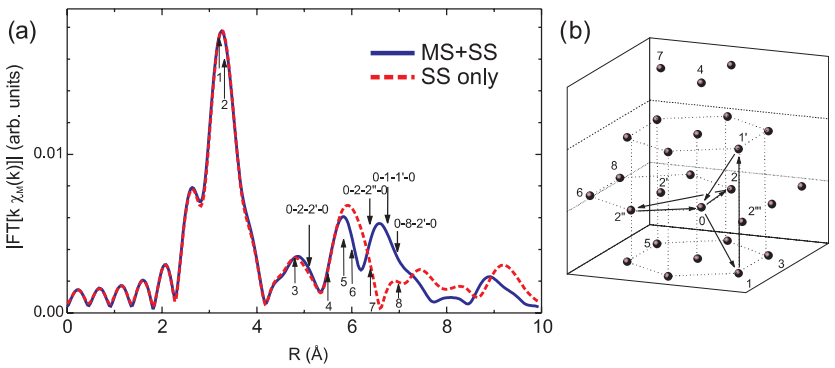

Figure 44. (*a*) Theoretical separation of multiple- and single-scattering contributions in the Tb MEXAFS (FEFF8.2) [326]. (*b*) Depiction of the dominant multiple-scattering paths.

We have shown that the temperature-dependent MEXAFS can be modelled by the difference of the energy-shifted EXAFS spectra. This procedure allows to disentangle the effect of spin fluctuations from lattice vibrations. We find experimentally that the temperature dependence of the energy shift follows the one of the magnetization. This demonstrates that the MEXAFS intensities have to be corrected for the reduced temperature T/T_C and the effect of the EXAFS Debye–Waller factor when the MEXAFS intensities are correlated to the spin-moment. Furthermore, we find by means of *ab initio* calculations that the multiple-scattering contributions in the rare earth MEXAFS interfere destructively with the single-scattering ones, in contrast to the findings for the 3d L edge MEXAFS.

6. Conclusion and outlook

The recent advances in XAS in experiment as well as in theory initiated progress in a large variety of fields: examples were given for surface physics of atomic and molecular adsorbates as well as for magnetism of nanostructures and even for the solution of fundamental questions of the spectroscopy itself. High brilliant x-rays provided by undulators at third generation synchrotron radiation sources allowed for the identification of fine structures in the x-ray absorption coefficient that were not resolved in the past. For example, it was possible to unambiguously ascertain the scattering origin of specific features in the XAS: the angular-dependent SEXAFS investigations of the strongly anisotropic oxygen induced surface reconstruction of Cu(110) allowed for the clear verification of the AXAFS effect. Thereby, the unique opportunity is established to study the anisotropy of the embedded atom potential. These new fundamental results are also of technical interest since AXAFS is already applied in electrochemistry to study the electronic structure of various Pt based electro-chemical and catalytic materials [123–126]. However, for the experimental detection of the AXAFS, self-controlled fitting codes for the determination of the spline function cannot be used since those eliminate the effect by allowing for a long period oscillatory background function. For the theoretical analysis the atomic background function must be investigated which is not a standard procedure. By studying the angular-dependent NEXAFS spectra of oriented hydrocarbon molecules on surfaces, the existence of the σ^* shape resonance could be proven, which has been questioned recently in literature. This provides new insight into the basic understanding of molecular spectroscopy. Also for this example the limits of the standard analysis procedures are reached: for the quantitative investigation of the σ^* shape resonance of hydrocarbon molecules FMS calculations had to be applied. The combination of experiment and theory advanced NEXAFS spectroscopy beyond the identification of 'fingerprints' towards a quantitative analysis.

The induced magnetism in 3d and 5d metals at interfaces of ultrathin films was investigated exploiting the element specificity of the x-ray absorption technique. The disentanglement of the total magnetic moment into the spin and orbital moment made it possible to link the magnetic anisotropy with the anisotropy of the orbital moment and yielded a microscopic picture of the characteristics of interfaces. Thereby, open questions were solved that could not be answered by non-element-specific techniques like FMR, VSM or SQUID: a complete magnetic moment profile for both constituents of Ni–Pt multilayers was constructed from XMCD measurements. Furthermore, the relative orientation of the induced spin and orbital moments in 5d metal layers at the interface to Fe was studied. This revealed the breakdown of the third Hund's rule for the case of W in an atomic framework. The comparison of these results to the ones for 5d impurities in Fe of earlier works provided a deeper insight into the nature of the induced magnetism. A short-range magnetic polarization was observed for the light 3d element V at the interface to Fe. Furthermore, the apparent long-range polarization for this system of earlier studies is explained by interdiffusion effects at the interfaces. This reveals the importance of atomically flat interfaces without interdiffusion also for technical applications. The detailed investigation of fine structures in the dichroic spectra demonstrated that the standard analysis (sum rules) fails, e.g. for light 3d elements and rare earth metals. Only with the help of theory can the magnetic ground state properties be determined from the spectra. This provided a more fundamental understanding of the spectroscopy itself: the interaction of the core hole with the photoelectron must be taken into account for the light 3d elements, E1 and E2 contributions have to be disentangled and the spin and energy dependence of the transition elements must be considered for the analysis of rare earth XMCD. If this is ignored, even the sign of the determined magnetic moments can be wrong. With this

work a step forward to a comprehensive description of rare earth L edge XMCD is taken. This offers a new insight into more complex rare earth compounds, as, e.g. new strong permanent magnets for technical applications. The temperature-dependent analysis of the magnetic EXAFS provided a deeper understanding of the effects of local spin dynamics on the dichroic fine structure in the extended energy range. For the separation of the effects of lattice vibrations and local spin dynamics on MEXAFS, a new method has been applied which models the magnetic EXAFS by the difference of the energy shifted isotropic EXAFS spectra.

Future work will focus on the present limits of experiment and theory. The combination of *in situ* preparation under UHV conditions with the applicability of large magnetic fields (several Tesla) and low temperatures ($T \approx 10$ K) is still demanding. These extreme measuring conditions are necessary for the study of further miniaturized magnetic nanostructures [244, 332, 333]. Joint XAS and microscopy studies add lateral resolution to the technique which, e.g. allow for the investigation of magnetic domains and their dynamics [334,335]. The present limits of theory were highlighted in this review for several examples: the experimentally determined anisotropy of the AXAFS could not be modelled by theory within the muffin tin approach. Full potential codes are under development right now. As it became obvious in the analysis of the XMCD of light 3d elements, the one-electron approach breaks down. This demonstrates the need for an excited state spectroscopy which is currently emerging [108–113, 115]. Furthermore, the magnetism is only theoretically described at $T = 0$ K. The theoretical modelling of the temperature dependence, e.g. of the spin-dependent DOS and the corresponding x-ray absorption spectra is not yet carried out. Today, experimentalists are able to probe materials with unprecedented resolution with the new generation of synchrotron radiation sources, which offers the potential for novel material studies. The computational physics has achieved enormous successes in describing ground state properties in the recent decades. However, the quantitative and reliable descriptions of excitations and response functions are just emerging. As a next step, time-dependent phenomena and nonlinear effects will be addressed theoretically. This is of major importance when looking at the rise of free-electron laser projects (fourth generation sources) [336–339] which will provide coherent x-ray pulses of even higher brilliance and clearly defined time structure in the femtosecond range. Today, a time-resolution in the picosecond range is only accessible at third generation sources. In the future, time-dependent studies will be carried out in the x-ray range that are today only possible in the visible and UV regime with advanced laser set-ups. The dynamics in quite different fields as for example magnetism, chemical reactions or biology will be studied. This reveals that the x-ray spectroscopy field looks into a bright future which will shed light on some more secrets in nature.

Acknowledgments

K Baberschke is gratefully acknowledged for imparting his detailed knowledge of XAS to me. His continuous encouragement was one of the driving forces which led to the advances presented here. I want to thank all co-workers and collaborators of his group—a number too large to be mentioned here. Several diploma and PhD students contributed to the results. Especially, I want to thank the Freie Universität Berlin and the University of Washington for supporting my stay at the University of Washington in spring 2003. Parts of the results reviewed here are the outcome of the fruitful collaboration with J J Rehr and A L Ankudinov during this visit. Furthermore, I want to thank H Ebert and his group for providing us with their calculations. During the measurements at the synchrotron radiation facilities we got strong support from the ESRF and BESSY staff members, which is highly appreciated. I would like

to thank in particular the BMBF and the DFG for the continuous support of our synchrotron projects.

References

[1] de Broglie M 1913 *Comptes Rendus* **157** 924–6
[2] Hüfner S 1995 *Photoelectron Spectroscopy (Springer Series in Solid-State Sciences)* vol 82 (Berlin: Springer)
[3] Warren B E 1969 *X-Ray Diffraction* (Reading: Addison-Wesley)
[4] van Nordstrand R 1960 *Adv. Catal.* **12** 149–87
[5] Sayers D, Lytle F and Stern E 1970 *Adv. X-Ray Anal.* **13** 248–71
[6] Sayers D E, Stern E A and Lytle F W 1971 *Phys. Rev. Lett.* **27** 1204–7
[7] Lengeler B 1992 *Synchrotronstrahlung zur Erforschung kondensierter Materie* (Vorlesungsmanuskripte, 23. IFF-Ferienkurs des Forschungszentrums Jülich, ISBN 3-89336-088-3)
[8] Lytle F W 1999 *J. Synchrotron Radiat.* **6** 124–34
[9] Schwinger J 1949 *Phys. Rev.* **75** 1912–25
[10] Stöhr J, Baberschke K, Jaeger R, Treichler R and Brennan S 1981 *Phys. Rev. Lett.* **47** 381–4
[11] Stöhr J, Sette F and Johnson A L 1984 *Phys. Rev. Lett.* **53** 1684–7
[12] Citrin P H 1985 *Phys. Rev.* B **31** 700–21
[13] Citrin P H 1986 *J. Physique* **12** C8-437–72
[14] Teo B K 1986 *EXAFS: Basic Principles and Data Analysis* (Berlin: Springer)
[15] Koningsberger D C and Prins R 1988 *X-Ray Absorption: Principles, Applications, Techniques of EXAFS, SEXAFS and XANES* (New York: Wiley)
[16] Stöhr J 1992 *NEXAFS Spectroscopy (Springer Series in Surface Sciences)* vol 25 (Berlin: Springer)
[17] Stöhr J 1988 in *X-Ray Absorption: Principles, Applications, Techniques of EXAFS, SEXAFS and XANES* ed D C Koningsberger and R Prins (New York: Wiley) pp 443–571
[18] Stöhr J, Jaeger R and Kendelewicz T 1982 *Phys. Rev. Lett.* **49** 142–6
[19] Baberschke K 1989 *Physica* B **158** 19–24
[20] Magnan H, Chandesris D, Rossi G, Jezequel G, Hricovini K and Lecante J 1989 *Phys. Rev.* B **40** 9989–92
[21] Magnan H, Chandesris D, Villette B, Heckmann O and Lecante J 1991 *Phys. Rev.* B **67** 859–62
[22] Heckmann O, Magnan H, le Fevre P, Chandesris D and Rehr J J 1994 *Surf. Sci.* **312** 62–72
[23] Le Fevre P, Magnan H, Heckmann O, Briois V and Chandesris D 1995 *Phys. Rev.* B **52** 11462–6
[24] Roubin P, Chandesris D, Rossi G, Lecante J, Desjonquéres M C and Tréglia G 1986 *Phys. Rev. Lett.* **56** 1272–5
[25] Sette F, Chen C T, Rowe J E and Citrin P H 1987 *Phys. Rev. Lett.* **59** 311–14
[26] Chandesris D and Rossi G 1988 *Phys. Rev. Lett.* **60** 2097
[27] Sette F, Chen C T, Rowe J E and Citrin P H 1988 *Phys. Rev. Lett.* **60** 2098
[28] Namikawa K, Ando M, Nakajima T and Kawata H 1985 *J. Phys. Soc. Japan* **54** 4099–102
[29] van der Laan G, Thole B T, Sawatzky G A, Goedkoop J B, Fuggle J C, Esteva J-M, Karnatak R, Remeika J P and Dabkowska H A 1986 *Phys. Rev.* B **34** 6529–31
[30] Schütz G, Wagner W, Wilhelm W and Kienle P 1987 *Phys. Rev. Lett.* **58** 737–40
[31] Erskine J L and Stern E A 1975 *Phys. Rev.* B **12** 5016–24
[32] Lee P A and Beni G 1977 *Phys. Rev.* B **15** 2862–83
[33] Lee P A, Citrin P H, Eisenberger P and Kincaid B M 1981 *Rev. Mod. Phys.* **53** 769–806
[34] Müller J E and Schaich W L 1983 *Phys. Rev.* B **27** 6489–92
[35] Schaich W L 1984 *Phys. Rev.* B **29** 6513–19
[36] Schaich W L 1973 *Phys. Rev.* B **8** 4028–32
[37] Ashley C A and Doniach S 1975 *Phys. Rev.* B **11** 1279–88
[38] Lee P A and Pendry J B 1975 *Phys. Rev.* B **11** 2795–811
[39] Natoli C R, Benfatto M and Doniach S 1986 *Phys. Rev.* A **34** 4682–94
[40] Rehr J J, Albers R C, Natoli C R and Stern E A 1986 *Phys. Rev.* B **34** 4350–53
[41] Rehr J J and Albers R C 1990 *Phys. Rev.* B **41** 8139–49
[42] Natoli C R, Benfatto M, Brouder C, Ruiz López M F and Foulis D L 1990 *Phys. Rev.* B **42** 1944–68
[43] Müller J E, Jepsen O, Andresen O K and Wilkins J W 1978 *Phys. Rev. Lett.* **40** 720–2
[44] Natoli C R, Misemer D K, Doniach S and Kutzler F W 1980 *Phys. Rev.* A **22** 1104–8
[45] Müller J E, Jepsen O and Wilkins J W 1982 *Solid State Commun.* **42** 365–8
[46] Norman D, Stöhr J, Jaeger R, Durham P J and Pendry J B 1983 *Phys. Rev. Lett.* **51** 2052–5
[47] Materlik G, Müller J E and Wilkins J W 1983 *Phys. Rev. Lett.* **50** 267–70
[48] Müller J E and Wilkins J W 1984 *Phys. Rev.* B **29** 4331–48

[49] Chou S-H, Kutzler F W, Ellis D E, Shenoy G K, Morrison T I and Montano P A 1985 *Phys. Rev.* B **85** 1069–76
[50] Stöhr J and Bauchspiess K R 1991 *Phys. Rev. Lett.* **67** 3376–9
[51] Ankudinov A L and Rehr J J 1995 *Phys. Rev.* B **52** 10214–20
[52] Brouder Ch, Alouani M and Bennemann K H 1996 *Phys. Rev.* B **54** 7334–49
[53] Ebert H 1996 *Rep. Prog. Phys.* **59** 1665–735
[54] Ankudinov A L and Rehr J J 1997 *Phys. Rev.* B **56** R1712–15
[55] Beni G and Platzman P M 1976 *Phys. Rev.* B **14** 1514–18
[56] Crozier E D, Rehr J J and Ingalls R 1988 *X-Ray Absorption: Principles, Applications, Techniques of EXAFS, SEXAFS and XANES* ed D C Koningsberger and R Prins (New York: Wiley) pp 373–442
[57] Yokoyama T 1998 *Phys. Rev.* B **57** 3423–32
[58] Poiarkova A V and Rehr J J 1999 *Phys. Rev.* B **59** 948–57
[59] Filipponi A 2001 *J. Phys.: Condens. Matter* **13** R23–60
[60] Campbell L, Hedin L, Rehr J J and Bardyszewski W 2002 *Phys. Rev.* B **65** 064107
[61] Alagna L, Prosperi T, Turchini S, Goulon J, Rogalev A, Goulon-Ginet C, Natoli C R, Peacock R D and Stewart B 1998 *Phys. Rev. Lett.* **80** 4799–802
[62] Poumellec B, Cortes R, Tourillon G and Berthon J 1991 *Phys. Status Solidi* b **164** 319–26
[63] Lovesey S W 1998 *J. Phys.: Condens. Matter* **10** 2505–13
[64] Neubeck W, Vettier C, de Bergevin F, Yakhou F, Mannix D, Bengone O, Alouani M and Barbier A 2001 *Phys. Rev.* B **63** 134430
[65] Danger J, Le Févre P, Magnan H, Chandesris D, Bourgeois S, Jupille J, Eickhoff T and Drube W 2002 *Phys. Rev. Lett.* **88** 243001
[66] von Barth U and Grossmann G 1979 *Solid State Commun.* **32** 645–9
[67] Stern E A and Rehr J J 1983 *Phys. Rev.* B **27** 3351–7
[68] Nesvizhskii A I, Ankudinov A L and Rehr J J 2001 *Phys. Rev.* B **63** 094412
[69] Fano U 1969 *Phys. Rev.* **178** 131–6
[70] Fano U 1969 *Phys. Rev.* **184** 250–1
[71] Schütz G, Fischer P, Goering E, Attenkofer K, Ahlers D and Rößl W 1997 *Synchrotron Radiat. News* **10** 13–26
[72] Stöhr J and Nakajima R 1998 *IBM J. Res. Dev.* **42** 73–88
[73] Scherz A 2004 *PhD Thesis* Freie Universität Berlin (Berlin: Dissertation.de-Verlag im Internet GmbH) ISBN 3-89825-779-7
[74] Ebert H 1996 *Spin–Orbit-Influenced Spectroscopies of Magnetic Solids* (*Lecture Notes in Physics*) ed H Ebert and G Schütz (Berlin: Springer) pp 159–77
[75] Wienke R, Schütz G and Ebert H 1991 *J. Appl. Phys.* **69** 6147–9
[76] Schütz G, Knülle M and Ebert H 1993 *Phys. Scr.* T **49** 302–6
[77] Thole B T, Carra P, Sette F and van der Laan G 1992 *Phys. Rev. Lett.* **68** 1943–6
[78] Carra P, Thole B T, Altarelli M and Wang X 1993 *Phys. Rev. Lett.* **70** 694–7
[79] Strange P 1994 *J. Phys.: Condens. Matter* **6** L491–5
[80] Chen C T, Idzerda Y U, Lin H-J, Smith N V, Meigs G, Chaban E, Ho G H, Pellegrin E and Sette F 1995 *Phys. Rev. Lett.* **75** 152–5
[81] Ankudinov A L and Rehr J J 1995 *Phys. Rev.* B **51** 1282–5
[82] Teramura Y, Tanaka A and Jo T 1996 *J. Phys. Soc. Japan* **65** 1053–5
[83] Ankudinov A L, Rehr J J, Wende H, Scherz A and Baberschke K 2004 *Europhys. Lett.* **66** 441–7
[84] Stöhr J and König H 1995 *Phys. Rev. Lett.* **75** 3748–51
[85] Kittel C 1949 *Phys. Rev.* **76** 743–8
[86] Kittel C 1951 *J. Phys. Radium* **12** 291
[87] Lytle F 1965 *Physics of Non-Crystalline Solids* ed J Prins (Amsterdam: North-Holland) p 12
[88] Kronig R 1932 *Z. Phys.* **75** 468
[89] Rehr J J and Albers R C 2000 *Rev. Mod. Phys.* **72** 621–54
[90] Rehr J J and Ankudinov A L 2001 *J. Electron. Spectrosc. Relat. Phenom.* **114–116** 1115–21
[91] Ankudinov A L, Ravel B, Rehr J J and Conradson S D 1998 *Phys. Rev.* B **58** 7565–76
For details see http://leonardo.phys.washington.edu/feff/
[92] Newville M, Ravel B, Haskel D, Rehr J J, Stern E A and Yacoby Y 1995 *Physica* B **208/209** 154–5
[93] Bahrdt J, Frentrup W, Gaupp A, Scheer M, Gudat W, Ingold G and Sasaki S 2001 *Nucl. Instrum. Methods Phys. Res.* A **467–468** 21–9
[94] Sasaki S 1994 *Nucl. Instrum. Methods. Phys. Res.* A **347** 83–6
[95] Kortright J B, Awschalom D D, Stöhr J, Bader S D, Idzerda Y U, Parkin S S P, Schuller I K and Siegmann H-C 1999 *J. Magn. Magn. Mater.* **207** 7–44

[96] Schütz G, Knülle M, Wienke R, Wilhelm W, Wagner W, Kienle P and Frahm R 1988 *Z. Phys. B—Condens. Matter* **73** 67–75
[97] Wende H *et al* 2002 *J. Appl. Phys.* **91** 7361–3
Wende H *et al* 2004 *ESRF Highlights 2003* 84–5
[98] Natoli C R, Benfatto M, Della Longa S and Hatada K 2003 *J. Synchrotron Radiat.* **10** 26–42
[99] Teo B-K and Lee P A 1979 *J. Am. Chem. Soc.* **101** 2815–32
[100] McKale A G, Knapp G S and Chan S-K 1986 *Phys. Rev.* B **33** 841–6
[101] Binsted N 1998 *EXCURV98: CCLRC Daresbury Laboratory Computer Program*
For details see http://srs.dl.ac.uk/XRS/Computing/Programs/excurv97/intro.html
[102] Filipponi A, Di Cicco A and Natoli C R 1995 *Phys. Rev.* B **52** 15122–34
For details see http://gnxas.unicam.it/XASLABwww/pag_gnxas.html
[103] Blaha P, Schwarz K, Madsen G K H, Kvasnicka D and Luitz J 2001 *WIEN2k, An Augmented Plane Wave + Local Orbitals Program for Calculating Crystal Properties* (Austria: Karlheinz Schwarz, Universität Wien) ISBN 3-9501031-1-2 For details see http://www.wien2k.at/index.html
[104] Ebert H 2000 *Electronic Structure and Physical Properties of Solids* (*Lecture Notes in Physics* vol 535) ed H Dreyssé (Berlin: Springer) pp 191–246
[105] Ebert H 2002 Ludwig-Maximilians-Universität München
For details see http://olymp.cup.uni-muenchen.de/ak/ebert/SPRKKR/
[106] Kotani A 1997 *J. Phys. IV (France)* **7** C2-1–8
[107] de Groot F M F 1994 *J. Electron Spectrosc. Relat. Phenom.* **67** 529–622
[108] Shirley E L 1998 *Phys. Rev. Lett.* **80** 794–7
[109] Schwitalla J and Ebert H 1998 *Phys. Rev. Lett.* **80** 4586–9
[110] Soininen J A and Shirley E L *Phys. Rev.* B **64** 165112
[111] Soininen J A, Rehr J J and Shirley E L 2003 *J. Phys.: Condens. Matter* 2573–86
[112] Rehr J J 2003 *J. Phys.: Condens. Matter* **15** S647–54
[113] Ankudinov A L, Nesviszhskii A I and Rehr J J 2003 *Phys. Rev.* B **67** 115120
[114] Hedin L 1999 *J. Phys.: Condens. Matter* **11** R489–528
[115] Petersilka M, Gossmann U J and Gross E K U 1996 *Phys. Rev. Lett.* **76** 1212–15
[116] Holland B W, Pendry P, Pettifer R F and Bordas J 1978 *J. Phys. C: Solid State Phys.* **11** 633–42
[117] Rehr J J, Booth C H, Bridges F and Zabinsky S I 1994 *Phys. Rev.* B **49** 12347–50
[118] Di Cicco A and Filipponi A 1994 *Phys. Rev.* B **49** 12564–71
[119] Filipponi A and Di Cicco A 1995 *Phys. Rev.* A **52** 1072–8
[120] Filipponi A and Di Cicco A 1996 *Phys. Rev.* B **53** 9466–7
[121] Rehr J J, Zabinsky S I, Ankudinov A and Albers R C 1995 *Physica* B **208–209** 23–6
[122] Rehr J J, Booth C H, Bridges F and Zabinsky S I 1996 *Phys. Rev.* B **53** 9468–70
[123] Ramaker D E, Mojet B L, Koningsberger D C and O'Grady W E 1998 *J. Phys.: Condens. Matter* **10** 8753–70
[124] O'Grady W E and Ramaker D E 1998 *Electrochim. Acta* **44** 1283–7
[125] van Dorssen G E, Koningsberger D C and Ramaker D E 2002 *J. Phys.: Condens. Matter* **14** 13529–41
[126] Tromp M, van Bokhoven J A, Slagt M Q, Klein Gebbink R J M, van Koten G, Ramaker D E and Koningsberger D C 2004 *J. Am. Chem. Soc.* **126** 4090–1
[127] Wende H, Arvanitis D, Tischer M, Chauvistré R, Henneken H, May F and Baberschke K 1997 *J. Phys. IV (France)* **7** C2-211–12
[128] Wende H, Srivastava P, Chauvistré R, May F and Baberschke K 1997 *J. Phys.: Condens. Matter* **9** L427–33
[129] Wende H and Baberschke K 1999 *J. Electron Spectrosc. Relat. Phenom.* **101–103** 821–6
[130] Wende H 1999 *PhD Thesis* Freie Universität Berlin (Berlin: Verlag, Dr. Köster) ISBN 3-89574-341-0
[131] Wende H, Litwinski Ch, Scherz A, Gleitsmann T, Li Z, Sorg C, Baberschke K, Ankudinov A, Rehr J J and Jung Ch 2003 *J. Phys.: Condens. Matter* **15** 5197–206
[132] Döbler U, Baberschke K, Haase J and Puschmann A 1984 *Phys. Rev. Lett.* **52** 1437–40
[133] Döbler U, Baberschke K, Vvedensky D D and Pendry J B 1986 *Surf. Sci.* **178** 679–85
[134] Bader M, Puschmann A, Ocal C and Haase J 1986 *Phys. Rev. Lett.* **57** 3273–6
[135] Feidenhans'l R, Grey F, Johnson R L, Mochrie S G J, Bohr J and Nielsen M 1990 *Phys. Rev.* B **41** 5420–3
[136] Jensen F, Besenbacher F, Lægsgaard E and Stensgaard I 1990 *Phys. Rev.* B **41** 10233–6
[137] Coulman D J, Wintterlin J, Behm R J and Ertl G 1990 *Phys. Rev. Lett.* **64** 1761–4
[138] Besenbacher F, Jensen F, Lægsgaard, Mortensen K and Stensgaard I 1991 *J. Vac. Sci. Technol.* B **9** 874–8
[139] Besenbacher F and Nørskov J K 1993 *Prog. Surf. Sci.* **44** 5–66
[140] Liu W, Wong C, Zeng H C and Mitchell K A R 1995 *Prog. Surf. Sci.* **50** 247–57
[141] Stahrenberg K, Richter Th, Esser N and Richter W 2000 *Phys. Rev.* B **61** 3043–7

[142] Jung Ch, Eggensten F, Hartlaub S, Follath R, Schmidt J S, Senf F, Weiss M R, Zeschke Th and Gudat W 2001 *Nucl. Instrum. Methods. Phys. Res.* A **467–468** 485–7
[143] Follath R 2001 *Nucl. Instrum. Methods Phys. Res.* A **467–468** 418–25
[144] Litwinski Ch *Diploma Thesis* Freie Universität Berlin unpublished
[145] Ravel B, Newville M, Cross J O and Bouldin C E 1995 *Physica* B **208 & 209** 145–7
[146] Wende H, Arvanitis D, Tischer M, Chauvistré R, Henneken H, May F and Baberschke K 1996 *Phys. Rev.* B **54** 5920–6
[147] Parkin S R, Zeng H C, Zhou M Y and Mitchell K A R 1990 *Phys. Rev.* B **41** 5432–5
[148] van de Riet E, Smeets J B J, Fluit J M and Niehaus A 1990 *Surf. Sci.* **214** 111–40
[149] Dürr H, Fauster Th and Schneider R 1991 *Surf. Sci.* **244** 237–46
[150] Rehr J J, Bardyszewski W and Hedin L 1997 *J. Phys. IV (France)* **7** C2-97–98
[151] Dehmer J L, Dill D and Wallace S 1979 *Phys. Rev. Lett.* **43** 1005–8
[152] Arvanitis D, Rabus H, Wenzel L and Baberschke K 1989 *Z. Phys.* D **11** 219–29
[153] Rabus H, Arvanitis D, Wenzel L and Baberschke K 1990 *Phys. Scr.* **41** 846–9
[154] Sette F, Stöhr J and Hitchcock A P 1984 *J. Chem. Phys.* **81** 4906–14
[155] Arvanitis D, Baberschke K, Wenzel L and Döbler U 1986 *Phys. Rev. Lett.* **57** 3175–8
[156] Arvanitis D, Döbler U, Wenzel L and Baberschke K 1986 *Surf. Sci.* **178** 686–92
[157] Stöhr J, Outka D A, Baberschke K, Arvanitis D and Horsley J A 1987 *Phys. Rev.* B **36** 2976–9
[158] Arvanitis D, Wenzel L and Baberschke K 1987 *Phys. Rev. Lett.* **59** 2435–8
[159] Piancastelli M N, Ferrett T A, Lindle D W, Medhurst L J, Heimann P A, Liu S H and Shirley D A 1989 *J. Chem. Phys.* **90** 3004–9
[160] Sheehy J A, Gil T J, Winstead C L, Farren R E and Langhoff P W 1989 *J. Chem. Phys.* **91** 1796–812
[161] Farren R E, Sheehy J A and Langhoff P W 1991 *Chem. Phys. Lett.* **177** 307–14
[162] Weinelt M, Huber W, Zebisch P, Steinrück H-P, Pabst M and Rösch N 1992 *Surf. Sci.* **271** 539–54
[163] Kempgens B, Köppe H M, Kivimäki A, Neeb M, Maier K, Hergenhahn U and Bradshaw A M 1997 *Phys. Rev. Lett.* **79** 35–8
[164] Kempgens B, Köppe H M, Kivimäki A, Neeb M, Maier K, Hergenhahn U and Bradshaw A M 1999 *Surf. Sci.* **425** L376–80
[165] Sorensen S L, Wiklund M, Sundin S, Ausmees A, Kikas A and Svensson S 1998 *Phys. Rev.* A **58** 1879–84
[166] Thomas T D, Berrah N, Bozek J, Carroll T X, Hahne J, Karlsen T, Kukk E and Sæthre L J 1999 *Phys. Rev. Lett.* **82** 1120–3
[167] Haack N, Ceballos G, Wende H, Baberschke K, Arvanitis D, Ankudinov A L and Rehr J J 2000 *Phys. Rev. Lett.* **84** 614–17
[168] Arvanitis D, Haack N, Ceballos G, Wende H, Baberschke K, Ankudinov A L and Rehr J J 2000 *J. Electron Spectrosc. Relat. Phenom.* **113** 57–65
[169] Connerade J P 1987 *Giant Resonances in Atoms, Molecules and Solids (NATO ASI Series)* ed J P Connerade *et al* (New York: Plenum) p 3
[170] Rehr J J, Albers R C and Zabinsky S I 1992 *Phys. Rev. Lett.* **69** 3397–400
[171] Rehr J J 1993 *Japan. J. Appl. Phys.* **32** 8
[172] Piancastelli M N 1999 *J. Electron Spectrosc. Relat. Phenom.* **100** 167–90
[173] Hitchcock A P and Brion C E 1977 *J. Electron Spectrosc. Relat. Phenom.* **10** 317–30
[174] Hemmers O *et al* 1997 *J. Phys.* B **30** L727–33
[175] Lindle D W and Hemmers O 1999 *J. Electron Spectrosc. Relat. Phenom.* **100** 297–311
[176] Derevianko A, Hemmers O, Oblad S, Glans P, Wang H, Whitfield S B, Wehlitz R, Sellin I A, Johnson W R and Lindle D W 2000 *Phys. Rev. Lett.* **84** 2116–19
[177] Baibich M N, Broto J M, Fert A, Nguyen Van Dau F, Petroff F, Eitenne P, Creuzet G, Friedrich A and Chazelas J 1988 *Phys. Rev. Lett.* **61** 2472–5
[178] Binasch G, Grünberg P, Saurenbach F and Zinn W 1989 *Phys. Rev.* B **39** 4828–30
[179] *Wall Street Journal* 10 November 1997, p B8
[180] Dax M 1997 *Semicond. Int.* **20** 84
[181] Ney A, Pampuch C, Koch R and Ploog K H 2003 *Nature* **425** 485–7
[182] Grünberg P, Schreiber R, Pang Y, Brodsky M B and Sowers H 1986 *Phys. Rev. Lett.* **57** 2442–5
[183] Parkin S S P, More N and Roche K P 1990 *Phys. Rev. Lett.* **64** 2304–7
[184] Parkin S S P, Bhadra R and Roche K P 1991 *Phys. Rev. Lett.* **66** 2152–5
[185] Bruno P 1995 *Phys. Rev.* B **52** 411–39
[186] Lindner J and Baberschke K 2003 *J. Phys.: Condens. Matter* **15** R193–232
[187] Prinz G A 1998 *Science* **282** 1660–3
[188] Coehoorn R 1995 *J. Magn. Magn. Mater.* **151** 341–53

[189] Moog E R, Zak J and Bader S D 1991 *J. Appl. Phys.* **69** 4559–61
[190] Nakajima N, Koide T, Shidara T, Miyauchi H, Fukutani H, Fujimori A, Iio K, Katayama T, Nývlt M and Suzuki Y 1998 *Phys. Rev. Lett.* **81** 5229–32
[191] Wu R, Li C and Freeman A J 1991 *J. Magn. Magn. Mater.* **81** 71–80
[192] Niklasson A M N, Johansson B and Skriver H L 1999 *Phys. Rev.* B **59** 6373–82
[193] Izquierdo J, Vega A, Elmouhssine O, Dreyssé H and Demangeat C 1999 *Phys. Rev.* B **59** 14510–15
[194] Tomaz M A, Antel W J Jr, O'Brien W L and Harp G R 1997 *J. Phys.: Condens. Matter* **9** L179–84
[195] Schwickert M M, Coehoorn R, Tomaz M A, Mayo E, Lederman D, O'Brien W L, Lin T and Harp G R 1998 *Phys. Rev.* B **57** 13681–91
[196] Farle M 1998 *Rep. Prog. Phys.* **61** 755–826
[197] Farle M, Anisimov A N, Baberschke K, Langer J and Maletta H 2000 *Europhys. Lett.* **49** 658–64
[198] Lindner J and Baberschke K 2003 *J. Phys.: Condens. Matter* **15** S465–78
[199] Scherz A, Wende H, Poulopoulos P, Lindner J, Baberschke K, Blomquist P, Wäppling R, Wilhelm F and Brookes N B 2001 *Phys. Rev.* B **64** 180407
[200] Wende H, Scherz A, Wilhelm F and Baberschke K 2003 *J. Phys.: Condens. Matter* **15** S547–59
[201] Scherz A, Wende H, Baberschke K, Minár J, Benea D and Ebert H 2002 *Phys. Rev.* B **66** 184401
Scherz A, Wende H, Sorg C, Baberschke K, Minár J, Benea D and Ebert H 2003 *BESSY Highlights 2002* 8–9
[202] Scherz A, Poulopoulos P, Wende H, Ceballos G and Baberschke K 2002 *J. Appl. Phys.* **91** 8760–2
[203] Scherz A, Poulopoulos P, Nünthel R, Lindner J, Wende H, Wilhelm F and Baberschke K 2003 *Phys. Rev.* B **68** 140401
[204] Scherz A, Wende H and Baberschke K 2004 *Appl. Phys.* A **78** 843–6
[205] Scherz A, Wende H, Sorg C, Baberschke K, Minár J, Benea D and Ebert H 2004 *Phys. Scr.* at press
[206] Wilhelm F, Poulopoulos P, Wende H, Scherz A, Baberschke K, Angelakeris M, Flevaris N K and Rogalev A 2001 *Phys. Rev. Lett.* **87** 207202
Wilhelm F, Poulopoulos P, Wende H, Scherz A, Baberschke K, Angelakeris M, Flevaris N K and Rogalev A 2002 *ESRF Highlights 2001* 65–6
[207] Wilhelm F *et al* 2000 *Phys. Rev. Lett.* **85** 413–16
Wilhelm F *et al* 2001 *ESRF Highlights 2000* 63–5
[208] Tyer R, van der Laan G, Temmerman W T and Szotek Z 2003 *Phys. Rev. Lett.* **90** 129701
[209] Wilhelm F, Poulopoulos P, Wende H, Scherz A, Baberschke K, Angelakeris M, Flevaris N K and Rogalev A 2003 *Phys. Rev. Lett.* **90** 129702
[210] Tyer R, van der Laan G, Temmerman W M, Szotek Z and Ebert H 2003 *Phys. Rev.* B **67** 104409
[211] Wilhelm F *et al* 2000 *Phys. Rev.* B **61** 8647–50
[212] Poulopoulos P, Wilhelm F, Li Z, Scherz A, Wende H, Baberschke K, Angelakeris M, Flevaris N K, Rogalev A and Brookes N B 2004 *J. Magn. Magn. Mater.* **272–276** 317–18
[213] Harmon B N and Freeman A J 1974 *Phys. Rev.* B **10** 1979–93
[214] Moon R M, Koehler W C, Cable J W and Child H R 1972 *Phys. Rev.* B **5** 997–1015
[215] Coey J M D 1996 *Rare-Earth Iron Permanent Magnets* (Oxford: Clarendon)
[216] Carra P and Altarelli M 1990 *Phys. Rev. Lett.* **64** 1286–8
[217] Carra P, Harmon B N, Thole B T, Altarelli M and Sawatzky G A 1991 *Phys. Rev. Lett.* **66** 2495–8
[218] Carra P, König H, Thole B T and Altarelli M 1993 *Physica* B **192** 182–90
[219] Wang X, Leung T C, Harmon B N and Carra P 1993 *Phys. Rev.* B **47** 9087–90
[220] Giorgetti Ch, Dartyge E, Brouder Ch, Baudelet F, Meyer C, Pizzini S, Fontaine A and Galéra R-M 1995 *Phys. Rev. Lett.* **75** 3186–9
[221] Bartolomé F, Tonnerre J M, Sève L, Chaboy J, García, Krisch M and Kao C C 1997 *Phys. Rev. Lett.* **79** 3775–8
[222] Giorgetti Ch, Dartyge E, Baudelet F and Brouder Ch 2001 *Appl. Phys.* A **73** 703–6
[223] Chaboy J, Bartolomé F, García L M and Cibin G 1998 *Phys. Rev.* B **57** R5598–601
[224] Lang J C, Srajer G, Detlefs C, Goldman A I, König H, Wang X, Harmon B N and McCallum R W 1995 *Phys. Rev. Lett.* **74** 4935–8
[225] Wende H, Wilhelm F, Poulopoulos P, Baberschke K, Freeland J W, Idzerda Y U, Rogalev A, Schlagel D L, Lograsso T A and Arvanitis D 2000 *AIP Conf. Proc.* **514** 140–7
[226] Wende H, Wilhelm F, Poulopoulos P, Rogalev A, Schlagel D L, Lograsso T A and Baberschke K 2001 *J. Synchrotron Radiat.* **8** 419–21
[227] Wende H, Wilhelm F, Poulopoulos P, Rogalev A, Goulon J, Schlagel D L, Lograsso T A and Baberschke K 2001 *Nucl. Instrum. Methods Phys. Res.* A **467–468** 1426–9
[228] Schütz G, Frahm R, Mautner P, Wienke R, Wagner W, Wilhelm W and Kienle P 1989 *Phys. Rev. Lett.* **62** 2620–3

[229] Srivastava P *et al* 1998 *J. Appl. Phys.* **83** 7025–7
[230] Wende H, Srivastava P, Arvanitis D, Wilhelm F, Lemke L, Ankudinov A, Rehr J J, Freeland J W, Idzerda Y U and Baberschke K 1999 *J. Synchrotron Radiat.* **6** 696–8
[231] Angelakeris M, Poulopoulos P, Vouroutzis N, Nyvlt M, Prosser V, Visnovsky S, Krishnan R and Flevaris N K 1997 *J. Appl. Phys.* **82** 5640–5
[232] Flevaris N K, Poulopoulos P, Angelakeris M and Niarchos D 1995 *J. Magn. Magn. Mater.* **140–144** 613–14
[233] Shin S-C, Srinivas G, Kim Y-S and Kim M-G 1998 *Appl. Phys. Lett.* **73** 393–5
Kim Y-S and Shin S-C 1999 *Phys. Rev.* B **59** R6597–600
[234] Parra R E and Cable J W 1980 *Phys. Rev.* B **21** 5494–504
Parra R E and Medina R 1980 *Phys. Rev.* B **22** 5460–70
[235] Krishnan R, Lassri H, Prasad S, Porte M and Tessier M 1993 *J. Appl. Phys.* **73** 6433–5
[236] Vogel J, Fontaine A, Cros V, Petroff F, Kappler J P, Krill G, Rogalev A and Goulon J 1997 *Phys. Rev.* B **55** 3663–9
[237] Poulopoulos P *et al* 2001 *J. Appl. Phys.* **89** 3874–9
[238] Poulopoulos P, Scherz A, Wilhelm F, Wende H and Baberschke K 2002 *Phys. Status Solidi* a **189** 293–300
[239] Grange W *et al* 1998 *Phys. Rev.* B **58** 6298–304
[240] Staiger W, Michel A, Piedrron-Bohnes V, Hermann N and Cadeville M C 1997 *J. Mater. Res.* **12** 161
[241] Frota-Pessôa S, Klautau A B and Legoas S B 2002 *Phys. Rev.* B **66** 132416
[242] Félix-Medina R, Dorantes-Dávila J and Pastor G M 2003 *Phys. Rev.* B **67** 094430
[243] Dürr H A, Guo G Y, van der Laan G, Lee J, Lauhoff G and Bland J A C 1997 *Science* **277** 213–15
[244] Gambardella P *et al* 2003 *Science* **300** 1130–3
[245] Bruno P 1989 *Phys. Rev.* B **39** 865–8
[246] van der Laan G 1998 *J. Phys.: Condens. Matter* **10** 3239–53
[247] Weller D, Stöhr J, Nakajima R, Carl A, Samant M G, Chappert C, Mégy R, Beauvillain P, Veillet P and Held G A 1995 *Phys. Rev. Lett.* **75** 3752–5
[248] Tröger L, Arvanitis D, Baberschke K, Michaelis H, Grimm U and Zschech E 1992 *Phys. Rev.* B **46** 3283–9
[249] Hunter Dunn J, Arvanitis D, Mårtensson N, Tischer M, May F, Russo M and Baberschke K 1995 *J. Phys.: Condens. Matter* **7** 1111–9
[250] Nakajima R, Stöhr J and Idzerda Y U 1999 *Phys. Rev.* B **59** 6421–9
[251] Wilhelm F 2000 *PhD Thesis* Freie Universität Berlin (Berlin: Dissertation.de-Verlag im Internet GmbH) ISBN 3-89825-177-2
[252] Daalderop G H O, Kelly P J and Schuurmans M F H 1990 *Phys. Rev.* B **41** 11919–37
[253] Újfalussy B, Szunyogh L, Bruno P and Weinberger P 1996 *Phys. Rev. Lett.* **77** 1805–8
[254] Hjortstam O, Baberschke K, Wills J M, Johansson B and Eriksson O 1997 *Phys. Rev.* B **55** 15026–32
[255] Wu R, Chen L and Freeman A J 1997 *J. Magn. Magn. Mater.* **170** 103–9
[256] Qian W and Hübner W 2003 *Phys. Rev.* B **67** 184414
[257] Hjelm A, Eriksson O and Johansson B 1993 *Phys. Rev. Lett.* **71** 1459–61
[258] Galanakis I, Alouani M and Dreyssé H 2000 *Phys. Rev.* B **62** 3923–8
[259] Qian W and Hübner W 1999 *Phys. Rev.* B **60** 16192–7
[260] Qian W and Hübner W 2001 *Phys. Rev.* B **64** 092402
[261] Ebert H, Zeller R, Drittler B and Dederichs P H 1990 *J. Appl. Phys.* **67** 4576–8
[262] Kornherr C 1997 *Master Thesis* University of Munich
[263] Frota-Pessôa S 2004 *Phys. Rev.* B **69** 104401
[264] Schmailzl P, Schmidt K, Bayer P, Döll R and Heinz K 1994 *Surf. Sci.* **312** 73–81
[265] Heinz K, Müller S and Hammer L 1999 *J. Phys.: Condens. Matter* **11** 9437–54
[266] Lemke L *et al* 1998 *J. Phys.: Condens. Matter* **10** 1917–30
[267] Pizzini S *et al* 1992 *Phys. Rev.* B **46** 1253–6
[268] Zhou X W and Wadley H N G 1998 *J. Appl. Phys.* **84** 2301–15
[269] Weiss M R *et al* 2001 *Nucl. Instrum. Methods Phys. Res.* A **467–468** 449–52
[270] Hamada N, Terakura K and Yanase A 1984 *J. Phys. F: Met. Phys.* **14** 2371–8
[271] Fink J, Müller-Heinzerling Th, Scheerer B, Speier W, Hillebrecht F U, Fuggle J C, Zaanen J and Sawatzky G A 1985 *Phys. Rev.* B **32** 4899–904
[272] van der Laan G 1997 *J. Phys.: Condens. Matter* **9** L259–65
[273] Rüdt C, Poulopoulos P, Lindner J, Scherz A, Wende H, Baberschke K, Blomquist P and Wäppling R 2002 *Phys. Rev.* B **65** 220404
[274] Kalska B, Häggström L, Blomquist P and Wäppling R 2000 *J. Phys.: Condens. Matter* **12** 539–48
[275] Kalska B, Blomquist P, Häggström L and Wäppling R 2001 *Europhys. Lett.* **53** 395–400
[276] Uzdin V, Westerholt K, Zabel H and Hjörvarsson B 2003 *Phys. Rev.* B **68** 214407

[277] Schmitz D, Hauschild J, Imperia P, Liu Y T and Maletta H 2004 *J. Magn. Magn. Mater.* **269** 89–94
[278] Eriksson O, Bergqvist L, Holmström E, Bergman A, LeBacq O, Frota-Pessoa S, Hjörvarsson B and Nordström L 2003 *J. Phys.: Condens. Matter* **15** S599-615
[279] Holström E, Nordström L, Bergqvist L, Skubic B, Hjörvarsson B, Abrikosov I A, Svendlindh P and Eriksson O 2004 *Proc. Natl Acad. Sci. USA* **101** 4742–5
[280] van der Laan G 1997 *Phys. Rev.* B **55** 8086–9
[281] Mirebeau I, Parette G and Cable J W 1987 *J. Phys. F: Met. Phys.* **17** 191
[282] Anisimov A N, Farle M, Poulopoulos P, Platow W, Baberschke K, Isberg P, Wäppling R, Niklasson A M N and Eriksson O 1999 *Phys. Rev. Lett.* **82** 2390–3
[283] Wu R, Wang D and Freeman A J 1993 *Phys. Rev. Lett.* **71** 3581–4
[284] Wu R and Freeman A J 1994 *Phys. Rev. Lett.* **73** 1994–7
[285] Sacchi M, Mirone M, Hague C F, Mariot J-M, Pasquali L, Isberg P and Gullikson E M 1999 *Phys. Rev.* B **60** R12569–72
[286] Komelj M, Ederer C and Fähnle M 2004 *Phys. Rev.* B **69** 132409
[287] Goering E, Bayer A, Gold S, Schütz G, Rabe M, Rüdiger U and Güntherodt G 2002 *Phys. Rev. Lett.* **88** 207203
[288] Goering E, Ahlers D, Attenkofer K, Obermeier G, Horn S and Schütz G 1999 *J. Synchrotron Radiat.* **6** 537–9
[289] Goering E, Gold S and Bayer A 2004 *Appl. Phys.* A **78** 855–65
[290] van der Laan G and Thole B T 1991 *Phys. Rev.* B **43** 13401–11
[291] Lindner J 2003 *PhD Thesis* Freie Universität Berlin (Berlin: Dissertation.de-Verlag im Internet GmbH) ISBN 3-89825-606-5
[292] Tischer M, Hjortstam O, Arvanitis D, Hunter Dunn J, May F, Baberschke K, Trygg J, Wills J M, Johansson B and Eriksson O 1995 *Phys. Rev. Lett.* **75** 1602–5
[293] Fnidiki A, Juraszek J, Teillet J, Duc N H, Danh T M, Kaabouchi M and Sella C 1998 *J. Appl. Phys.* **84** 3311–16
[294] Idzerda Y U, Tjeng L H, Lin H-J, Gutierrez C J, Meigs G and Chen C T 1993 *Phys. Rev.* B **48** 4144–7
[295] Ebert H, Schütz G and Temmerman W M 1990 *Solid State Commun.* **76** 475–8
[296] Neumann C, Hoogenboom B W, Rogalev A and Goedkoop J B 1999 *Solid State Commun.* **110** 375–9
[297] Miguel-Soriano J, Chaboy J, Garcia L M, Bartolomé F and Maruyama H 2000 *J. Appl. Phys.* **87** 5884–6
[298] Lang J C, Kycia S W, Wang X D, Harmon B N, Goldman A I, Branagan D J, McCallum R W and Finkelstein K D 1992 *Phys. Rev.* B **46** 5298–302
[299] Krisch M H, Kao C C, Sette F, Caliebe W A, Hämäläinen K and Hastings J B 1995 *Phys. Rev. Lett.* **74** 4931–4
[300] Krisch M H, Sette F, Bergmann U, Masciovecchio C, Verbeni R, Goulon J, Caliebe W and Kao C C 1996 *Phys. Rev.* B **54** R12673–6
[301] Gibbs D, Harshman D R, Isaacs E D, McWhan D B, Mills D and Vettier C 1988 *Phys. Rev. Lett.* **61** 1241–4
[302] Hannon J P, Trammel G T, Blume M and Gibbs D 1988 *Phys. Rev. Lett.* **61** 1245–8
[303] Langridge S, Paixão J A, Bernhoeft N, Vettier C, Lander G H, Gibbs D, Sørensen S Aa, Stunault A, Wermeille D and Talik E 1999 *Phys. Rev. Lett.* **82** 2187–90
[304] Fischer P, Schütz G, Scherle S, Knülle M, Stähler S and Wiesinger G 1992 *Solid State Commun.* **82** 857–61
[305] Hegland D E, Legvold S and Spedding F H 1963 *Phys. Rev.* **131** 158–62
[306] Wu R, Wang D and Freeman A J 1993 *Phys. Rev. Lett.* **71** 3581–4
[307] Ankudinov A L, Rehr J J, Wende H and Baberschke K 2004 *Phys. Scr.* at press
[308] Ahlers D and Schütz G 1998 *Phys. Rev.* B **57** 3466–73
[309] Dartyge E, Fontaine A, Giorgetti Ch, Pizzini S, Baudelet F, Krill G, Brouder Ch and Kappler J P 1992 *Phys. Rev.* B **46** 3155–8
[310] Dartyge E, Baudelet F, Brouder C, Fontaine A, Giorgetti C, Kappler J P, Krill G, Lopez M F and Pizzini S 1995 *Physica* B **208 & 209** 751–4
[311] Schütz G and Ahlers D 1996 *Spin–Orbit-Influenced Spectroscopies of Magnetic Solids* (*Lecture Notes in Physics*) ed H Ebert and G Schütz (Berlin: Springer) pp 229–57
[312] Ahlers D, Schütz G, Popescu V and Ebert H 1998 *J. Appl. Phys.* **83** 7082–4
[313] Ebert H, Minár J, Popescu V, Sandratskii L and Mavromaras A 2000 *AIP Conf. Proc.* **514** 110–19
[314] Brouder C, Alouani M, Giorgetti C, Dartyge E and Baudelet F 1996 *Spin–Orbit-Influenced Spectroscopies of Magnetic Solids* (*Lecture Notes in Physics*) ed H Ebert and G Schütz (Berlin: Springer) pp 259–74
[315] Wende H, Freeland J W, Chakarian V, Idzerda Y U, Lemke L and Baberschke K 1998 *J. Appl. Phys.* **83** 7028–30
[316] Ebert H, Popescu V and Ahlers D 1999 *Phys. Rev.* B **60** 7156–65
[317] Popescu V, Ebert H and Ahlers D 1999 *J. Magn. Magn. Mater.* **191** 368–72
[318] Pizzini S, Fontaine A, Dartyge E, Giorgetti C, Baudelet F, Kappler J P, Boher P and Giron F 1994 *Phys. Rev.* B **50** 3779–88

[319] Goulon J, Rogalev A, Gauthier C, Goulon-Ginet C, Paste S, Signorato R, Neumann C, Varga L and Malgrange C 1998 *J. Synchrotron Radiat.* **5** 232–8
[320] Gauthier C, Goujon G, Feite S, Moguiline E, Braicovich L, Brookes N B and Goulon J 1995 *Physica* B **208 & 209** 232–4
[321] Rogalev A, Gotte V, Goulon J, Gauthier C, Chavanne J and Elleaume P 1998 *J. Synchrotron Radiat.* **5** 989–91
[322] Tsang T W, Gschneider K A, Schmidt F A and Thome D K 1985 *Phys. Rev.* B **31** 235–44
[323] Ahlers D, Attenkofer K and Schütz G 1998 *J. Appl. Phys.* **83** 7085–7
[324] Ebert H, Popescu V, Ahlers D, Schütz G, Lemke L, Wende H, Srivastava P and Baberschke K 1998 *Europhys. Lett.* **42** 295–300
[325] Gotsis H J and Strange P 1994 *J. Phys.: Condens. Matter* **6** 1409–16
[326] Wende H *et al* 2004 *Phys. Scr.* at press
[327] Nigh H E, Legvold S and Spedding F H 1963 *Phys. Rev.* **132** 1092–7
[328] Zabinsky S I, Rehr J J, Ankudinov A, Albers R C and Eller M J 1995 *Phys. Rev.* B **52** 2995–3009
[329] Chaboy J, Marcelli A and Tyson T A 1994 *Phys. Rev.* B **49** 11652–61
[330] Schüßler-Langeheine C, Weschke E, Mazumdar C, Meier R, Grigoriev A Y, Kaindl G, Sutter C, Abernathy D, Grübel G and Richter M 2000 *Phys. Rev. Lett.* **84** 5624–7
[331] Legvold S 1980 *Ferromagnetic Materials* vol 1, ed E P Wohlfarth (Amsterdam: North-Holland) pp 183–295
[332] Gambardella P, Dhesi S S, Gardonio S, Grazioli C, Ohresser P and Carbone C 2002 *Phys. Rev. Lett.* **88** 047202
[333] Lau J T, Föhlisch R, Nietubyč, Reif M and Wurth W 2002 *Phys. Rev. Lett.* **89** 057201
[334] Kuch W, Chelaru L I, Offi F, Wang J, Kotsugi M and Kirschner J 2004 *Phys. Rev. Lett.* **92** 017201
[335] Vogel J, Kuch W, Bonfim M, Camarero J, Pennec Y, Offi F, Fukumoto K, Kirschner J, Fontaine A and Pizzini S 2003 *Appl. Phys. Lett.* **82** 2299–301
[336] Sonntag B 2001 *Nucl. Instrum. Methods Phys. Res.* A **467–468** 8–15
[337] Kapteyn H C and Ditmire T 2002 *Nature* **420** 467–8
[338] Wabnitz H *et al* 2002 *Nature* **420** 482–5
[339] Cornacchia M *et al* 2004 *J. Synchrotron Radiat.* **11** 227–38